DOT/FAA/TC-23/35

Federal Aviation Administration
William J. Hughes Technical Center
Aviation Research Division
Atlantic City International Airport
New Jersey 08405

Integrated Propulsion and Controls for Rotorcraft – Phase 1

October 2023

Final report

U.S. Department of Transportation
Federal Aviation Administration

NOTICE

Technical Report Documentation Page

Form DOT F 1700.7 (8-72) Reproduction of completed page authorized

1. Report No. DOT/FAA/TC-23/35	2. Government Accession No.	3. Recipient's Catalog No.
4. Title and Subtitle Integrated Propulsion and Controls for Rotorcraft – Phase 1		5. Report Date October 2023 6. Performing Organization Code
7. Author(s) Kyle B. Collins, Richard P. Anderson, Richard Prazenica, K. Merve Dogan, Patric Hruswicki, Riccardo Roiati, Xinyu Yang, Jonathan Schroder, Nishant Sharma, Vivek Saini, Syed Zuhair Ali Razvi, Shivansh Agrawal, Sahil Ghate, Cody Kuskie, Robert L. Kincart, Zachary Herman, J. Cheston Newbold III, Atahan Kurttisi, Eren Sarioglu, Ernesto Perez Leal		8. Performing Organization Report No.
9. Performing Organization Name and Address Embry Riddle Aeronautical University (Eagle Flight Research Center) 1 Aerospace Blvd, Daytona Beach, FL, 32114, USA		10. Work Unit No. (TRAIS) 11. Contract or Grant No. #629M15-21-T-00037
12. Sponsoring Agency Name and Address Federal Aviation Administration (FAA)		13. Type of Report and Period Covered Final Report (August 2021 – December 2022) 14. Sponsoring Agency Code

15. Supplementary Notes
FAA Sponsors: David Sizoo, Ross Schaller, Dan Dellmyer, Traci Stadtmueller

16. Abstract

This technical report documents research conducted by Embry-Riddle Aeronautical University’s Eagle Flight Research Center team in the Integrated Flight and Propulsion Control for Rotorcraft Performance under contract 692M15-19-R-00016.
The purpose of the research was to evaluate the performance of various control strategies multi-rotor VTOL aircraft could employ for both nominal and degraded modes of flight. The lessons developed herein are beneficial to Urban and Advanced Air mobility vehicle developers by promoting increased awareness of flight safety through the benefits a collective-cyclic pitch mixed (CCPM) capable rotor system can offer. A large, unmanned quadcopter was built with unique distributed electric propulsion (DEP) units and proved that sustained flight with one rotor disabled is possible. Dynamic simulation models were developed for individual rotor systems and the entire vehicle to predict in-flight behavior of both nominal and motor-out modes of quadrotor, hexarotor, and octorotor flight. Traditional thrust differential-based control logic did not provide adequate control for sustained flight in any failure mode.

17. Key Words Integrated Propulsion and Controls for Rotorcraft, eVTOL, distributed electric propulsion (DEP), thrust control strategies, failure mode analysis, vehicle flight testing, vehicle simulation, control allocation, fault-tolerant flight control, handling qualities prediction, trajectory following, simulation.	18. Distribution Statement This document is available to the U.S. public through the National Technical Information Service (NTIS), Springfield, Virginia 22161. This document is also available from the Federal Aviation Administration William J. Hughes Technical Center at actlibrary.tc.faa.gov.

19. Security Classif. (of this report) Unclassified	20. Security Classif. (of this page) Unclassified	21. No. of Pages 182	19. Security Classif. (of this report) Unclassified

Contents

Figures

Tables

Acronyms

Acronym	**Definition**
AAM	Advanced Air Mobility
ACAH	Attitude Command/ Attitude Hold
ARP	Aerospace Recommended Practice
ATS	Attitude Test Stand
BET	Blade Element Theory
BPD	Bandwidth and Phase Delay
CAD	Computer Aided Design
CG	Center of Gravity
CM	Center of Mass
COF	Crossover Frequency
DAQ	Data Acquisition
DCM	Direction Cosine Matrix
DEP	Distributed Electric Propulsion
DOD	Department Of Defense
DOF	Degree of Freedom
DRB	Disturbance Rejection Bandwidth
EFRC	Eagle Flight Research Center
ERAU	Embry-Riddle Aeronautical University
ESC	Electronic Speed Controller
eVTOL	Electric Vertical Take-off and Landing
FAA	Federal Aviation Administration
FAR	Federal aviation regulations
FBW	Fly-by-wire
FDI	Fault Detection & Isolation
FEA	Finite Element Analysis
FFT	Fast Fourier Transform
FP	Fixed Pitch
FTC	Fault-Tolerant Controls
HQTE	Handling Qualities Task Element
IMU	Inertial Measurement Unit
LQR	Linear Quadratic Regulator
MDEP&C	Multi-rotor distributed electric propulsion and control

Acronym	**Definition**
MIL-STD	Military Standard
MMA	Motor Mixing Algorithm
MOC	Means of compliance
MTE	Mission Task Element
NACA	National Advisory Committee for Aeronautics
NASA	National Aeronautics and Space Administration
NED	North-East-Down
NLDI	Nonlinear Dynamic Inversion
ODE	Ordinary Differential Equations
PAVER	Personal Air Vehicle Embry Riddle
PID	Proportional Integral Derivative
PIM	Pseudo-Inverse Method
PIO	Pilot Induced Oscillation
PLA	Polylactic Acid
PMF	Perfect Model Following
PWM	Pulse Width Modulation
RC	Remote Controlled
RCAH	Rate Command/ Attitude Hold
RCAS	Rotorcraft Comprehensive Analysis System
RPM	Revolutions Per Minute
RTS	Rotor Test Stand
SAE	Society of Automotive Engineers
SAST	Single-Arm Structural Test
SVO	Simplified Vehicle Operation
UAM	Urban Air Mobility
UEI	United Electronic Industries
VP1	Variable Pitch 1
VP2	Variable Pitch 2

Executive summary

Distributed electric propulsion (DEP) has increased the design space for aerospace vehicles, specifically the electric Vertical Takeoff and Landing (eVTOL) class. The rising number of companies offering contending vehicles for certification by the Federal Aviation Administration (FAA) pushes the need for tailored airworthiness regulations. To certify these aircraft for private and commercial operations, a greater understanding of how the vehicle is controlled in both nominal and off-nominal modes is required. The purpose of the research documented herein is to assess how the various methods of DEP thrust control can be integrated into larger urban air mobility (UAM) passenger-carrying missions, and to investigate how well the methods perform in both normal and degraded modes of operation.

The Eagle Flight Research Center (EFRC) built two large, unmanned quadcopter platforms using DEP rotor units to validate various control strategies. Rotorheads with collective and cyclic pitch capabilities were tested, measured, and analyzed for performance and scalability using a thrust stand. Validated full-vehicle simulation models were then created to support control law development, vehicle handling predictions, as well as performance in failure modes. Nonlinear simulations generated ideal trajectories, the best-case capabilities of a vehicle with an "ideal" control law. Valuable lessons were learned from this work, and some recommendations for design considerations have been assessed, including minimum thrust-to-weight requirements, minimum rotors required for degraded flight, structural resonance considerations of multi-rotor vehicles, and control law performance.

The design process of any fault-tolerant multi-rotor eVTOL vehicle should start from an acknowledgment that unexpected mechanical failures can occur, and account for the maximum possible number of propulsors that can fail. Only then can propulsion sizing begin, targeting a vehicle thrust-to-weight ratio of more than 1:1 with the minimum number of rotors active, allowing adequate thrust to maintain altitude and overhead thrust for maintaining control during an emergency. The Personal Air Vehicle – Embry-Riddle (PAVER) quadcopter, a sub-scale demonstrator, has a 4:1 thrust-to-weight ratio, which allows for stable, controlled flight even with two missing rotors along one diagonal axis.

The conventional method of propulsion and control for multi-rotor vehicles entails using fixed-pitch propellers with direct-drive electric motors distributed symmetrically around the vehicle’s center of gravity. The RPM control system used for attitude and directional control in a multi-rotor aircraft relies on thrust differential for attitude control and torque differential for directional control. While this system has the advantage of simplicity and a low number of parts, it has a limitation in yaw authority, which is limited to the maximum reaction torque that can be

generated by all motors turning in the same direction (half the total number of rotors). Additionally, this method of yaw control through torque differential becomes inadequate as the inertia of the aircraft along the Z-axis increases. Another limitation of the RPM control system is that it can also limit pitch and roll control as the size of the aircraft increases, since it becomes more difficult to change the RPM of individual motors as the size and inertia of the rotor increases. This can make it more challenging to achieve the necessary pitch and roll angles for specific maneuvers.

Some designs demonstrate a solution to the yaw authority problem by permanently tilting some or all of their rotors to generate a yaw component from thrust. The greater the tilt angle, the more effective the yaw response is, at the cost of reducing vertical thrust capability. Control actuation in other axes (roll, pitch) relies on thrust differential about the vehicle’s center of gravity (CG). The response time of these systems depends on the rate at which the rotor can be accelerated or decelerated to a target thrust. A limitation in the scalability of such systems is that rotational inertia grows exponentially with diameter.

The PAVER drone demonstrates a superior form of control through moment generation at each rotor made possible by helicopter mechanics. While more complex mechanically, the benefits of blade pitch control are clearly demonstrated in flight by its fast response time and impressive control authority. Notably, each rotor equally contributes to yaw control without a reduction of rotor thrust by using cyclic pitch. Additionally, this cyclic pitch for yaw control capability makes it possible for the vehicle’s heading, attitude, and altitude to remain unaffected in the event of one rotor failure.

Vibration and resonance were prominent challenges for the PAVER design team. The first vehicle iteration began its test campaign with a notable failure characterized by airframe resonance focused on the torsional mode of the quadrotor arms. The vehicle’s rotor blades are allowed to lead and lag by design. This increases the effects of any slight rotor imbalance. Further, when multiple vibration sources (in the form of rotors) are paired together in a system, the likelihood of amplified resonance becomes a problem. A second PAVER vehicle was built to improve vibration characteristics and to operate as a redundant flight article. While many structural changes were incorporated to improve resilience, a similar resonance-based incident occurred with the new airframe in the same RPM range. However, the resonance was an in plane bending of the quadrotor arms. Vehicle stability was achieved by operating outside of these resonant RPM ranges.

Through study of control law implementation, it was found that a simplified vehicle operation (SVO) control law could negate the benefits a high-performance over-actuated propulsion and control system could provide, degrading the potential for safe flight in nominal and off-nominal scenarios. Future work could include vehicle-centered force and moment capability envelopes that illustrate the control power potentials and limitations of the bare airframe in comparison to implemented control laws.

Further recommendations and conclusions are made in this report, including design aspects, evaluations of rotor tests, simulation models, trajectory following, and control law logic of eVTOL airworthiness certification.

1 Introduction

1.1 eVTOL enabled by distributed electric propulsion

Distributed electric propulsion (DEP) has increased the design space for aerospace vehicles, specifically the class of vehicles characterized as electric vertical take-off and landing (eVTOL). Examples of vehicles currently being tested with hopes of achieving FAA certification are Joby aircraft and Wisk Aero vehicles shown in Figure 1. This new class of vehicles not only looks different from the typical airplane or helicopter with which the aviation community is familiar, but also functions differently. To certify these aircraft for private and commercial operations, a greater understanding of how the vehicle is controlled in both nominal and off nominal or degraded modes is required. The purpose of the research reported herein is to assess how the various methods of DEP thrust control scale up to the sizes required for the eVTOL mission, in addition to how well the methods perform in both normal and degraded modes of operation.

Figure 1. A) Joby aircraft's eVTOL and B) Wisk Aero's Cora on test flights
(image credits Joby Aviation and Wisk Aero)

1.2 Typical thrust control strategies employed by DEP in eVTOL

Many eVTOL configurations have elected to use a conventional fixed pitch RPM-controlled system that is ubiquitous to hobby-sized drones. Faster RPM generates more thrust up to its limit. This strategy is pictured in Figure 2 A. Another strategy is to set RPM to a desired speed and then change the collective pitch of the prop-rotor blades to control thrust. This strategy is pictured in Figure 2 B for thrust. Within the collective pitch strategy method, there can be differences in thrust response time to control input depending on how fast the pitch of the blades can change.

Figure 2. A) Thrust change by RPM only and B) by collective pitch and/or RPM change

1.3 A novel thrust- and moment-controllable DEP unit

The rotor unit that was developed at the Eagle Flight Research Center (EFRC) within the Embry-Riddle Aeronautical University (ERAU) utilizes collective pitch control and cyclic pitch control applied to a hingeless prop-rotor. This provides each rotor unit with the ability to create not only thrust but also a combination of thrust and control. Control is made possible through longitudinal and lateral moments as shown in Figure 3.

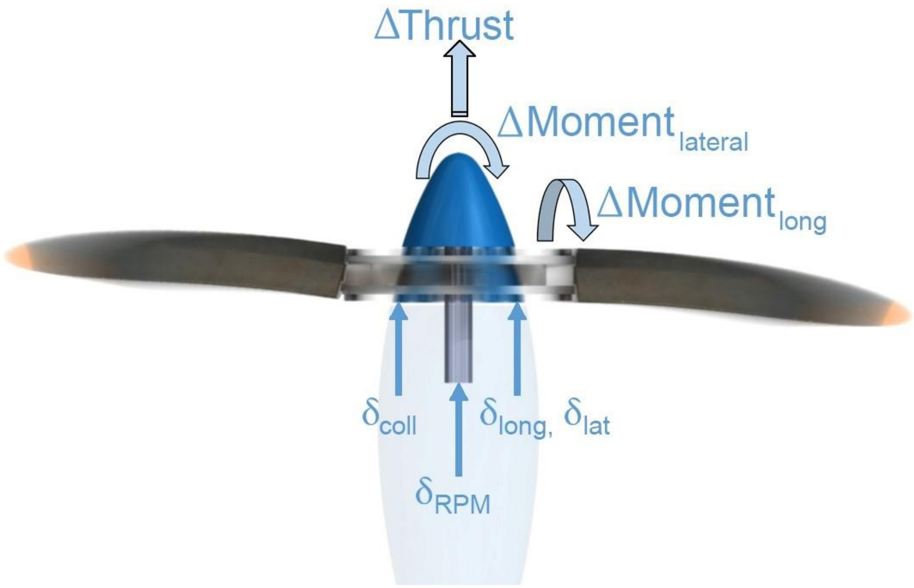

Figure 3. Thrust and moment control using RPM, collective pitch, and cyclic pitch change

This ability to create moments at the DEP unit can significantly increase the control authority of a vehicle in both nominal and degraded modes. For example, during a test flight of the tail sitter vehicle shown in Figure 4 A, one of the two DEP units failed. Despite this, the vehicle was able to land in its upright, tail-sitting position, using the thrust and moments created by the single DEP unit Figure 4 B and the autorotation capability of the failed DEP unit. This latent control redundancy makes a DEP unit of this type particularly attractive to the eVTOL concept. To demonstrate this, ERAU EFRC has created a 4-DEP unit eVTOL prototype Figure 4 C utilizing this DEP concept.

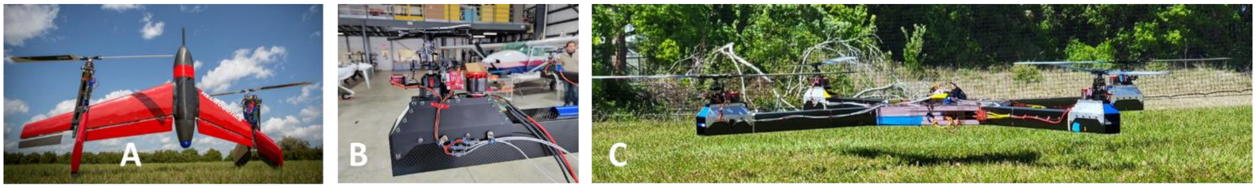

Figure 4. A) Hingeless rotor DEP equipped Mark II UAV, B) prototype DEP unit and C) 4-DEP unit prototype vehicle

1.4 Research contributions

The research performed consisted of DEP unit modeling and simulation combined with a complete flight dynamic vehicle model with DEP units that can be operated in any of the three control strategies mentioned in section 1.2. Simulations were performed to characterize the vehicle's stability, performance, and control bandwidth with respect to the control strategy used. The results of these virtual experiments were validated with tests using actual hardware developed in the ERAU's EFRC.

The research will lead to a greater understanding of the certification basis and methods of compliance for eVTOL and urban air mobility (UAM) vehicles that employ DEP for thrust, lift, and control. The main testbed of the research was a 4-DEP unit prototype constructed out of carbon fiber as shown in Figure 4C. The DEP units incorporated on the prototype allowed the investigation of the DEP control strategies listed in Table 1.

Table 1. DEP control strategies investigated

Strategy 1	**Strategy 2**	**Strategy 3**
Fixed Pitch, Vary RPM	Vary Collective Pitch, Govern RPM	Vary Collective Pitch, Vary Cyclic Pitch, Govern RPM

The 4-DEP configuration prototype is typical of vehicles in the DEP eVTOL category. With its collective- and cyclic-controllable pitch rigid rotor head, the vehicle can be operated in a way that represents various strategies that could be employed by eVTOL certification applicants. For example, the DEP units can be operated with a fixed-pitch RPM-variable thrust control. The DEP unit can also be operated by setting a specific RPM and controlling thrust by varying collective pitch. Furthermore, it can utilize both collective and cyclic pitch control to generate not only thrust changes but also moment changes at the DEP. This feature makes the testbed an invaluable tool in understanding how these classes of vehicles should be certified based on the thrust, lift, and control strategy used.

The research performed was a combination of both modeling and simulation combined with experimental studies. Outcomes of this research include the following:

1.4.1 DEP unit thrust and moment control characterization

Tests were performed on a single DEP unit on a test stand to measure how thrust, longitudinal moments, and lateral moments change with respect to changes in RPM, collective pitch, and cyclic pitch. The test stand was appropriately instrumented for force and moment measurements. Information gained during this testing was used to validate rotor models used in the simulation models of the 4-DEP unit test vehicle.

1.4.2 Failure mode analysis

The effect of a single rotor failure was examined using both simulation and test. This part of the research underscored how failures of units on vehicles using one strategy of thrust control compare to the other two strategies.

1.4.3 Modeling and simulation

The modeling and simulation research utilized a flight dynamics simulation of a multi-DEP unit test vehicle. A separate model of the hingeless DEP rotor unit was created, tuned, and exercised to predict the forces and moments created under the different control strategies (RPM only; RPM and Collective; and RPM, Collective, and Cyclic). Validation of the model was performed through static tests on a test stand. A full vehicle simulation model was created and used to aid in the development of control laws for the 4-rotor testbed, piloted simulation prior to tests, investigation of the various strategies of DEP unit control, and to investigate the ability of the vehicle to maintain control during a rotor failure scenario.

1.4.4 Testing and evaluation

A single DEP unit was tested in each control strategy on a test stand developed during Phase 1. The team used the results to validate and tune analytical models of the rotor. Furthermore, a 4-DEP unit prototype was completed and tested under different control strategies. The hover tests were repeated under various “degraded” conditions with a single DEP unit disabled. Test results revealed the ability of a 4-rotor vehicle in hover to continue to fly after a single rotor failure when a control law that utilized cyclic pitch was used, but not when the units were controlled with RPM or collective pitch only.

2 Background and motivation

The integration of DEP, digital fly-by-wire (FBW) flight control systems, and autonomous flight control has allowed a new vehicle market to emerge within general aviation. This new market is mostly comprised of eVTOL vehicles. Figure 5 shows two such concepts from Jaunt Air Mobility and Vinati F-Helix. These eVTOL vehicles will have similar design features to conventional VTOL aircraft.

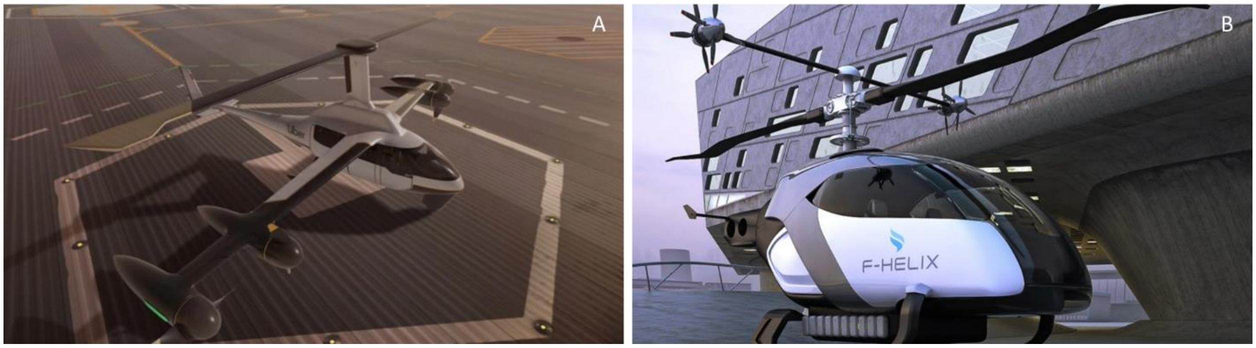

Figure 5. Artistic renditions of the eVTOL concepts
A) Jaunt air mobility slowed rotor compound helicopter and the B) Vinati F-helix propeller reaction driven helicopter (images from https://evtol.news)

Some other new vehicle concepts bear little resemblance at all to a conventional helicopter. Due to the added degree of flexibility offered by DEP and FBW, many concept vehicles incorporate a plurality of rotors and/or propellers in their designs. Some vector the thrust from these rotors to perform lifting functions in hovering and low-speed flight modes and propulsive functions in the cruise flight modes. Some designs use DEP units to lift and other DEP units to provide thrust. Some examples of these unique design configurations can be seen in Figure 6.

.

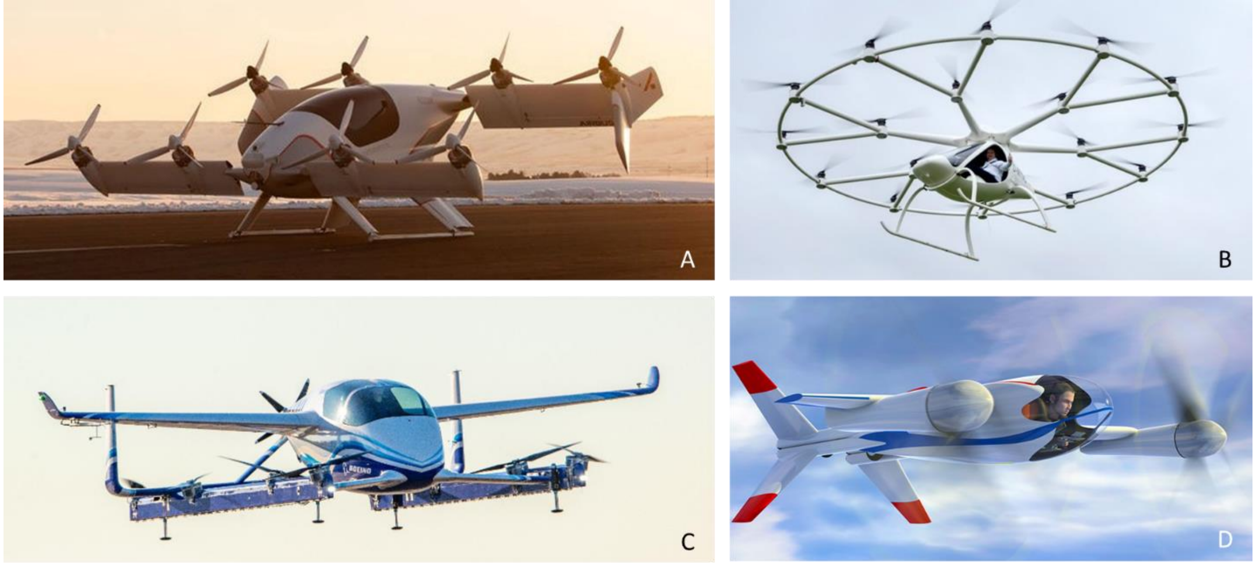

Figure 6. A) Vectored thrust Airbus A³ Vahana, B) Multi-rotor Volocoper, C) Lift + Cruise Boeing/Aurora PAV, and D) Tail-sitter NASA Puffin
(images from https://evtol.news)

Four vehicles currently well into development are the BlackFly by Opener, shown in Figure 7; Joby Aviation’s eVTOL prototype, shown in Figure 8; the Cora by Wisk prototype, shown in Figure 9, and the A^3 Vahana by Airbus, shown in Figure 10.

Figure 7. Opener’s Ultra-light BlackFly A) features list and in B) vertical landing
(credit: opener.aero)

Figure 8. Joby Aircraft (credit: Joby Aircraft)

Figure 9. Cora aircraft in hovering flight (credit: Wisk.aero)

Figure 10. Airbus Vahana prototype in hovering flight (credit: vahana.aero)

Most UAM and eVTOL concepts utilize multi-rotors and FBW. While many concepts also use a wing(s) for the cruise portion of the flight, it is not needed for hovering or very low-speed flight. However, wings are used since they provide a more efficient forward flight. Nevertheless, wings can provide reasonable means of gliding to a safe landing in the event of a complete power failure from a cruise flight if the wing loading allows. In cases where a complete power failure might prove catastrophic, some vehicles employ ballistic parachutes as an added safety feature. An example of a multi-rotor vehicle well into development that does not utilize a wing is the Ehang vehicle shown in Figure 11.

Figure 11. Ehang multi-rotor vehicle (credit: ehang.com)

One aspect of multi-rotor vehicles that may not be immediately noticeable is how the thrust of the DEP units is adjusted. In most cases, the thrust is modified using changes in propeller/rotor RPM, which is a simple and reliable method with few moving parts. However, this strategy has some limitations, such as the inability to produce negative thrust, no capability for producing hub moments, and slower response times as the size of the propeller increases. The thrust response may become slower as the propeller size grows, due to the larger inertia of the propeller and the greater torque required by the electric motor. In fact, there may be a point where this strategy is no longer effective as the motor size needed to generate the necessary torque to change the RPM of a large propeller becomes too large. Overall, the use of RPM changes to modify thrust is a useful technique, but it has its limitations that should be taken into consideration when designing and operating multi-rotor vehicles (Malpica & Withrow-Maser, 2020; Walter, McKay, Niemiec, Gandhi, & Ivler, 2020)

Some DEP units use collective pitch control at a fixed RPM to achieve more responsive thrust control. While this strategy is more mechanically complex, with more moving parts, it allows the RPM to be maintained at a desired constant value while changing the thrust through collective pitch changes. Additionally, if the collective pitch control is somehow impaired, thrust can still be controlled through RPM changes in this degraded mode. The FAA has a lot of experience certifying fixed-wing vehicles with constant-speed propellers that use this method. Overall, while the use of collective pitch control at a fixed RPM is more complex, it offers the benefits of more responsive thrust control and the ability to maintain a constant RPM.

A third strategy developed at the Eagle Flight Research Center involves the use of both collective and cyclic pitch on a DEP unit with a hingeless (rigid) rotor. While the use of collective and cyclic pitch itself is not new, as it is commonly used on helicopter rotors, its application on a DEP unit is unique. The added benefit of this strategy over the use of collective pitch alone is that the rigid rotor allows cyclic pitch changes to create significant lateral and longitudinal moments at the rotor hub, which can be used to control the vehicle in addition to using thrust alone on the DEP units. This should result in greater control power for the vehicle. Additionally, this strategy can provide control moments within a multi-rotor system even if one or more DEP units fail, without reducing thrust on the remaining DEP units. Overall, the use of both collective and cyclic pitch of the individual rotors offers the potential for greater control power and increased reliability in multi-rotor vehicles.

Though there are an ostensibly infinite number of vehicle configurations that can fulfill the role of an air taxi, more effort needs to be spent understanding the performance and safety factors for off nominal, or degraded modes of flight. This body of work cannot be ignored if UAM is to take hold in the realm of human transportation.

3 Problem statement

Over 140 companies are working on UAM concepts, each with unique propulsion architectures and control strategies. The airworthiness criteria and means of compliance to certify these vehicles are still in development. Current FAR 23/25, and FAR 27/29 rules are inadequate to certify the new UAM vehicles with FBW, SVO features and VTOL capabilities. It is crucial for the FAA to develop a set of rules appropriate for UAM/SVO as quickly as possible.

In order to do this, methods of reliably quantifying the safety of these systems while operating in both nominal and degraded system modes must be developed. The system development and safety assessment processes outlined in Aerospace Recommended Practice (ARP) 4754 (SAE International, 2010) and ARP 4761 (SAE International, 1996) respectively detail how to develop aerospace systems and assure them to be safe following a development assurance approach. These practices, however, ultimately require a prior knowledge of the effects of failure modes of the system, sub-systems, elements, and items. This a priori knowledge of these effects is available to both the designers and regulatory institutions when the system is a conventional airplane or helicopter. When the system deviates drastically from this, this knowledge is lacking.

The research documented herein is aimed at providing the knowledge as it relates to the use of lifting and thrusting DEP units, whether they are vectored thrust, multi-rotor, or lift + cruise. Specifically, the research focused on studying the implications of controlling the thrust (and moments if applicable) of the DEP unit by RPM change only, by using collective pitch change, and finally by using both collective and cyclic pitch change typical of helicopter rotor systems. It was theorized that the latter would offer the greatest ability of a multi-rotor system to be controlled in the event of failures of one or more DEP units. This is due to the ability of the cyclic pitch changes of a rigid rotor system to generate very large lateral and longitudinal moments. The functioning units can then use these moments to compensate for the loss of thrust and control ability that would be provided by the failed units. Understanding how the various control strategies can control a multi-rotor system with failed (or degraded) rotors greatly adds to the knowledge base of how this new class of vehicles should respond to degraded situations, and, more importantly, what control strategies provide the most robust solutions.

Perhaps the best way to understand the implications of how these different control strategies could affect the performance and control of the aircraft on which they are utilized is by using some notional examples. First, let us imagine that a DEP unit has failed in flight for some reason. In order to maintain balance, the RPM only strategy, as well as the RPM + collective pitch strategy may have to shut the diagonally opposite motor down, as shown in Figure 12. However, the RPM + collective & cyclic pitch strategy may be able to keep all remaining motors running and maintain balance by applying cyclic pitch to put moments on the DEP units, as shown in Figure 13.

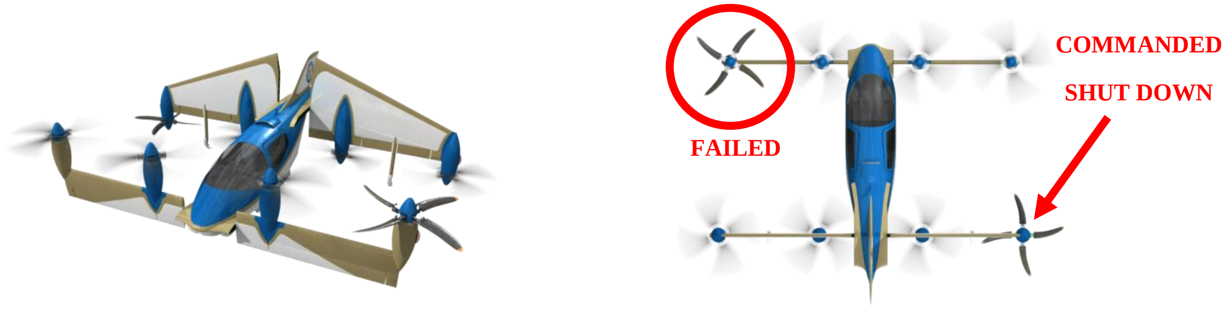

(A) (B)

Figure 12. Notional 8-DEP unit eVTOL where one DEP unit has failed and the diagonally opposite has been shut down to maintain balance shown in A) an Iso view and B) a Top view

(A) (B)

Figure 13. Notional 8-DEP unit eVTOL where one DEP unit has failed and all other motors are turning and using cyclic pitch to maintain balance shown in A) an Iso view and B) a Top view

In a similar example, suppose two motors fail. Using the same logic, the RPM-only strategy, as well as the RPM + collective pitch strategy, may have to shut the diagonally opposite motors down to maintain balance as shown in Figure 14. Depending on performance and factors of safety, it is unlikely the aircraft can maintain altitude in this situation. The strategy that utilizes collective & cyclic pitch can use cyclic pitch control moments on the functioning DEP units and may allow balance to be maintained while keeping all rotors producing thrust as shown in Figure 15.

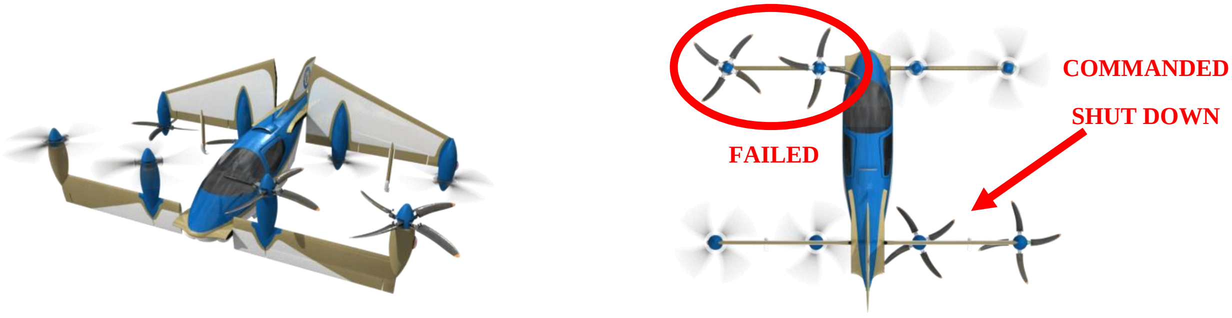

(A) (B)

Figure 14. Notional 8-DEP unit eVTOL where two DEP units have failed and the diagonally opposite motors have been shut down to maintain balance shown in A) an Iso View and B) a Top view

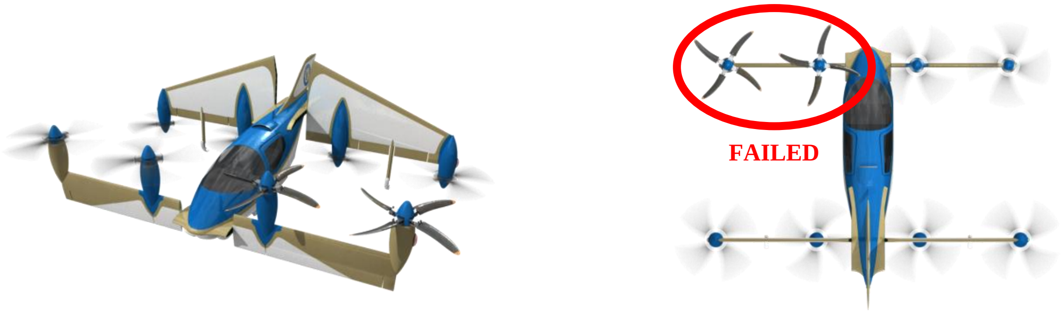

(A) (B)

Figure 15. Notional 8-DEP unit eVTOL where two DEP units have failed and all other motors are turning and using cyclic pitch to maintain balance shown in A) an Iso View and B) a Top view

To summarize, the primary purpose of the research presented herein is to identify barriers to certification and thus discover ways to affordably and safely approve these vehicles. Specifically, the focus is on handling qualities certification-related means of compliance on the multi-copter vehicle category for hovering flight. The quantitative results of simulation and flight-testing can be used to provide Lessons learned and insights that will help regulators better understand the challenges and safety issues of these new class of vehicles. The simulation and physical testing research performed will provide a better understanding of the safety of eVTOL vehicles in situations where DEP units fail and how this changes depending on the control strategy of the individual DEP units.

4 Technical approach

The technical approach described in Figure 16 is a general outline of the work performed. The flow is arranged logically with feedback based on the results of the testing accomplished. In addition to the knowledge gained about multi-rotor distributed electric propulsion and control (MDEP&C) systems applied to the eVTOL class of vehicles, the work is designed to provide some specific ideas about how the safety and certification of these vehicles can be generalized in a way that makes it easy for those qualified systems to enter certified service.

The sections of the technical approach shown in Figure 16 will be described below.

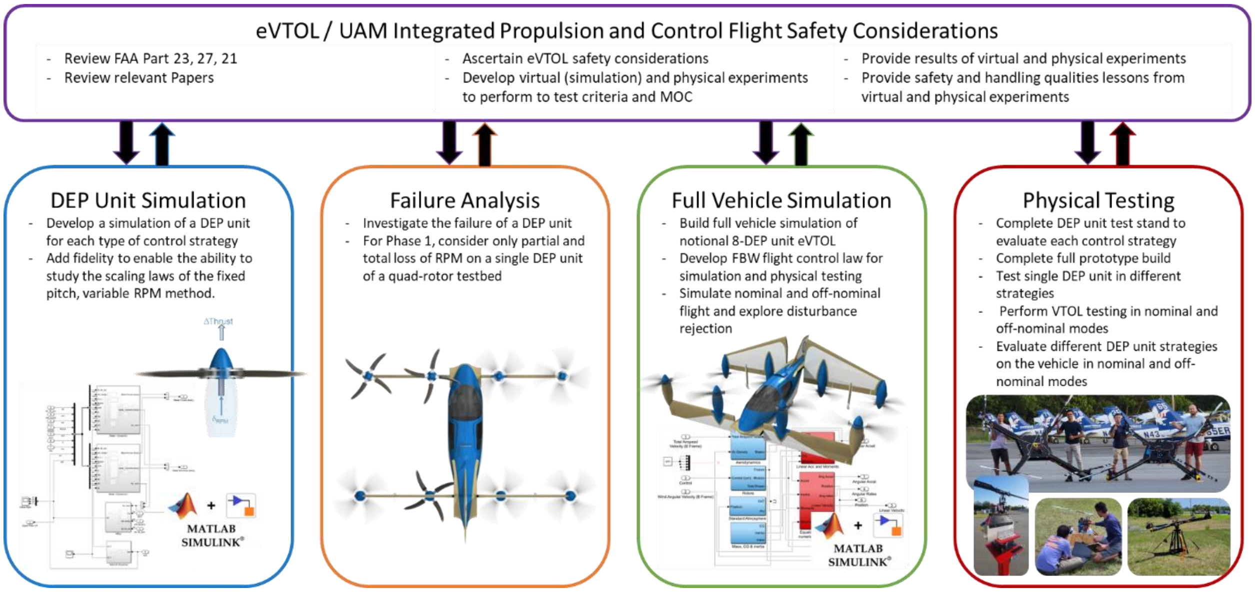

Figure 16. Phase 1 Technical Approach Diagram

4.1 eVTOL / UAM integrated propulsion and control flight safety considerations

MDEP&C vehicles come in a variety of configurations. The ample design space for these vehicles, along with the unique aspects of their integrated propulsion and FBW controls, has created a great deal of uncertainty about how they should be certified. There exists a need to identify barriers to certification and find ways to affordably certify systems and safety enhancements on powered-lift and distributed lift rotorcraft. This part of the technical approach is focused on exploring the state of the art in flight control as well as flight safety considerations of MDEP&C vehicles. When augmented with results from virtual simulation and physical testing, this aspect of the research provides the FAA with data and information to assist in the development of guidance, airworthiness criteria, and means of compliance for this type of vehicle.

This aspect of the technical approach will be a central element, serving as both the starting point and the result of all the work. It will involve gathering information from the literature review to guide experiments performed in simulation studies and physical tests, and then using the data generated in these simulations and tests to provide data and insight into the safety and flight control of eVTOL aircraft utilizing integrated propulsion and control systems. In this way, it will be a key factor in ensuring the success and relevance of the project.

4.2 DEP unit simulation

A parametric model of a DEP unit will be developed. The model can be easily adapted to simulate different types of DEP units, including ones with fixed pitch and variable RPM, as well as units where the RPM is controlled and the collective pitch is used to vary thrust. In addition, the simulation will be able to model a DEP unit that uses both collective and cyclic pitch on a governed RPM prop-rotor.

In addition to a dynamic simulation of the DEP unit, a model of the weights of the components will be developed. Furthermore, a model of the electric motor dynamics will also be created. Together, the ability of a fixed pitch prop-rotor to change thrust within some specified time (e.g., 50 ms) will be investigated as a function of the blade size. This task will provide beneficial information to understand how big a fixed pitch DEP system can be and still provide the necessary control bandwidth.

4.3 DEP rotor failure analysis

The three strategies of DEP unit propulsion and vehicle control examined in this research each have different failure modes. In the research performed, only failure of a DEP unit was considered. The failures represented were varying levels of thrust and moment reduction, including partial and complete loss of RPM on a single DEP unit.

4.4 Full vehicle flight dynamic simulation

Simulation models of the individual DEP models were incorporated into full vehicle simulation models. Both the DEP and vehicle simulations were validated using the test data from DEP unit tests and flight tests with the vehicle. While flight-testing focused on a single DEP unit loss of thrust/moment on a quadrotor vehicle, flight simulation efforts explored vehicles with more than 4 rotors and failures of more than one DEP unit.

Future work can incorporate flight control design and optimization using industry-recognized tools for an N-rotor eVTOL flight-dynamics model and flight vehicle. Future phase experiments could characterize the crossover frequency (COF), closed-loop bandwidth and phase design (BPD), disturbance rejection bandwidth (DRB), and system peak with varying controllers. Handling quality and ride quality metrics could also be tracked, as well as trade-offs with COF, BPD, and DRB. Additional failures identified in a more rigorous failure analysis will allow the researchers to investigate the full vehicle's response to such failures as a function of the type of thrust and control strategy employed.

4.5 Physical testing

DEP unit physical testing was conducted on single DEP units and a flight test vehicle. The single DEP unit testing was performed on a rotor test stand. Tethered and untethered vehicle flight tests were performed in a drone cage adjacent to the EFRC. These will be discussed in the sections below.

4.5.1 DEP unit testing

A rotor test stand, shown in Figure 17, was built and operated by the EFRC to understand how different control methods change thrust and control moments on a rotor head. Factors like thrust, torque, longitudinal and lateral moments were measured against changes in RPM, cyclic, and collective control.

Figure 17. DEP test stand at the EFRC

The results of the experiments performed were used to validate both performance and dynamic simulation models created during other tasks of the research.

4.5.2 Vehicle flight testing

A test matrix was built to investigate the operation in any of the three strategies of DEP unit thrust and control. Controllability and handling qualities were evaluated in both nominal and degraded modes of flight using the PAVER vehicle shown in Figure 18.

Figure 18. PAVER vehicle in hover

5 Performance of work tasks

5.1 Task A: Literature review

5.1.1 Advanced air mobility

The small electric VTOL aircraft market has made great strides in terms of development that are concurrent with advances in electric propulsion. The last five years in particular have seen an explosion in the public exposure and development of such vehicles. The Advanced Air Mobility (AAM) Reality Index, is currently tracking 21 separate vehicles being developed, encompassing a wide spectrum of maturity (SMG Consulting, 2021).

Many development hurdles have been cleared with several aircraft already having logged their first flights (SMG Consulting, 2021). That being said, many difficult development steps remain before an initial entry to service for any of these vehicles can be considered. Even so, many designers remain optimistic on their service entry dates, with nearly 60% of the aircraft being tracked by the AAM Reality Index citing an entry into service in the next 4 years. For such optimistic release dates, little work has been done in the realm of certification. This poses challenges for market confidence in the growth and scalability of UAM systems.

5.1.2 Handling qualities certification

The U.S. Army used the concept of mission task elements (MTEs) to aid in handling quality certification of military helicopters. Design specifications that enable predicted Level 1 handling qualities are outlined in ADS-33E (United States Army, 2000). The FAA is working towards methods to select and tailor mission task elements that are better suited to the eVTOL and UAM class of vehicles and have begun using the term handling qualities task elements (HQTEs) (Klyde, et al., 2020). HQTEs are similar to MTEs but are designed to indicate the types of elements the vehicle will perform during its mission.

Two important specifications in the analysis and design of systems are gain margin (open-loop gain needed to make a closed-loop system unstable that is related with designed control gain) and phase margin (the amount of change in open-loop phase needed to make a closed-loop system unstable that is related to time delay between commanded input and the output). The Bode graphical method in the frequency domain helps a designer to find these margins. Roll time, damping ratio, and natural frequency are also important elements in assessing handling qualities. The phase margin of 30–60 degrees and the gain margin of 2–10 dB are desirable in the closed-loop system design. Time delay is calculated by (phase margin) / (the frequency where phase margin occurs). Additionally, actuator dynamics can add additional time delays. Time delays have no contribution on a system’s gain response but have a linear effect as a phase shift/delay for the system.

The Society of Automotive Engineers (SAE) and the United States Army lay out some basic requirements for quadcopter handling qualities, (SAE, 2021) and (United States Army, 2000). First, control laws are designed to meet the damping ratio and stability margin requirements. Second, the heave step response of the system is evaluated using the hover and low-speed requirement of heave response to a collective input. The time constant and time delay are then defined. Third, the roll, pitch, and yaw handling qualities are evaluated by using a chirp signal as input to the system model. The phase delay and bandwidth are then extracted from the resultant Bode plot and referenced with these requirements.

There are two bandwidth specifications which are phase bandwidth (the frequency at which phase angle equals to -135 degrees) and gain bandwidth (the frequency at which the gain is 6 dB higher than the gain value of the phase crossover frequency), in addition to phase and gain margins according to United States Army (2000). The bandwidth specifications describe the frequency at which the amount of effective pilot control is assessed within system neutral stability. The important elements of ADS33 are attitude command / attitude hold (ACAH) and rate command / attitude hold (RCAH) response analyses, where bandwidth and phase delay are used to predict handling qualities levels of the vehicle.

A piloted simulation was performed with the NASA-Ames Vertical Motion Simulator for investigating the handling-quality implications of reduced flight control system stability margins and the trade-offs with higher disturbance rejection bandwidth (Blanken, et al., 2009). Several aircraft were simulated, and the flight characteristics of the aircraft were assessed using ADS-33E-PRF handling qualities metrics (Walter, McKay, Niemiec, Gandhi, & Ivler, 2019). In the following year, the same authors for the same problem designed optimized inner and outer loop controllers (Walter, McKay, Niemiec, Gandhi, & Ivler, 2020).

5.1.3 Control allocation

Control actuator settings are determined through control allocation. Control allocation improves fault tolerance and modularity of the overall control system while permitting the exploitation of actuator redundancy for improved maneuverability. A wide range of actuator configurations appear in current concepts for UAM vehicles (Rashad, Jelmer Goerres, Aarts, Engelen, & Stramigioli., 2020). This begs a deeper investigation of control allocation techniques for over-actuated (e.g., redundant) systems. Several topics should be considered in designing control allocation algorithms, such as actuator health, saturation, and failure. Control allocation approaches are categorized as pseudo-inverse, static, and dynamic control allocation (Alwi & Edwards, 2008; Durham, 1994; Tohidi, Sedigh, & Buzorgnia, 2016). Different control allocation techniques are discussed for over-actuated systems in the presence of saturation and failure (Johansen & Fossen, 2013; Oppenheimer, Doman, & Bolender, 2006; Tohidi, Yildiz, & Kolmanovsky, 2020; Lombaerts, et al., 2020; Zaccarian, 2009; Falconì, Angelov, & Holzapfel, 2018; Jaramillo, et al., 2022). In static control allocation, vehicles must guarantee adequate attitude command tracking performance under multiple circumstances. Typical attitude controllers consist of a feedback control architecture and a static control allocation function. The feedback controller calculates the required torques and thrust that the vehicle must achieve to maintain stable flight, while the static control allocation function converts these forces and torques into the desired pulse width modulation (PWM) signals sent to each motor.

Static control allocation has two distinct challenges. First, it carries a heavy computational burden due to the numerical solution of the constrained optimization problem at each sampling instant. Second, the configuration assumes that all components are fully functional, meaning that the system cannot adapt to the failure of a motor.

In dynamic control allocation, a dynamic update law for system inputs is derived so that instead of solving an optimization problem at each instant the control allocation problem is solved dynamically. Component health can also be analyzed in-flight to allow the system to adapt as required.

5.1.4 Fault-tolerant flight control

5.1.4.1 Introduction to fault-tolerant flight control and applications to multi-rotor air vehicles

Flight control is often one of the more difficult problems to solve during the design process of a new air vehicle. With the increasing commonality of high performance, low latency, and relatively error-free computers, fly-by-wire control systems have become increasingly more popular. Fly-by-wire systems offer many benefits including frequently better efficiency, as well as a lower workload on the pilot or flight crew (Flannigan, 1972). However, should some failure occur that damages or inhibits the flight controls or control computer, the aircraft is often uncontrollable without this equipment, which opens a major area of concern in vehicle safety. Flight fault-tolerant controls (FTC) are the obvious solution to this gap in the safety of fly-by-wire control systems. FTC systems work continuously to identify erroneous conditions within the flight control system as a whole. Should such a fault occur, the system could then maintain stability and allow for a safe recovery or landing of the vehicle and its passengers or cargo.

In the last decade, the development of small vertical takeoff and landing (VTOL) aircraft powered utilizing DEP has rapidly advanced, with many designs planning on an initial entry into service in the next 5 years (SMG Consulting, 2021). eVTOL and UAM vehicles are designed with advanced fly-by-wire systems for control, with several major companies introducing new fly-by-wire systems designed specifically for the small electric aircraft market.

A brief overview will be given on the intersection of these two developing factors and serve as an introduction to FTC design with the intent of augmenting the safety and robustness of upcoming fly-by-wire systems for use in UAM applications. A more in-depth introduction to FTC will be given, as well as an overview of today's research in this area. Considerations for implementation of FTC systems in UAM applications will be assessed.

5.1.4.2 What is fault-tolerant control?

Fault-tolerant control refers to any control system that is hardened against systemic failure because of a subsystem malfunction. Such malfunctions can be physical in nature such as a failure of an actuator, sensor, or control surface. Malfunctions could also be non-physical, for example a software failure in a flight control computer. Several different strategies exist to achieve a system such as this, however most systems can be described using one or more of the following descriptors: robust, reconfigurable or restructurable (Huang & Stengel, 2012). Robust systems are those, which will continue to operate as originally intended after a failure. In aircraft, flight dynamics or handling characteristics may be adversely affected; however, the vehicle will remain stable and controllable through no other outside action (Huang & Stengel, 2012). A reconfigurable system is one in which some change to the controller occurs after a failure is detected, altering system parameters (Huang & Stengel, 2012). Restructurable systems can shuffle system components in order to maintain system stability. Such measures should be implemented early in the control design process.

Any FTC design requires some level of redundancy. Two main forms of redundancy: physical redundancy and analytical redundancy were identified in a 2008 paper (Lunze & Richter, 2008). Physical redundancy refers to a physical duplicate or alternate component. Physically redundant components increase system cost and weight. Analytical redundancy refers to "the functional relationship between system inputs and outputs" (Lunze & Richter, 2008). Some controls may be used to affect different outputs of a system, even if they were not originally intended to control these outputs. For example, thrust from an engine on an aircraft often has some effect on the pitch of the aircraft, allowing for some control of this aspect of the aircraft if necessary. Analytical redundancy is more difficult to implement than physical redundancy in analysis and design, however, this difficulty should be assessed against the added weight, and cost of physically redundant parts (Lunze & Richter, 2008). The fewer outputs that are tracked for the model, the more redundancy is available for reconfiguration of a controller (Ward, Monaco, & Schierman, 1999). Because of this, considerable thought and effort must be dedicated to the design of such systems to optimize them such that they control only the required parameters of the system.

5.1.4.3 A general overview of FTC objectives

Control reconfiguration is essentially a two-step process, according to Gao (1996). First, the failed system must be stabilized such that the vehicle or process is not lost completely. The controller must then be redesigned to accommodate the failure in the system.

Minimizing the time required to accomplish these steps is critical, especially in the first step of stabilizing the system since if not stabilized in a short timeframe, the system as a whole could be lost (Gao, 1996). Gao notes that control algorithms typically used to stabilize the system, such as an optimal control linear quadratic regulator (LQR), may be too complex and take too long to run the steps to implement the controller.

5.1.4.4 A general overview for FTC design

Many challenges exist in the process of FTC design. One of the primary challenges of this process may seem trivial: no two systems are the same. Because of this, for each new system for which a new flight controller is designed, new strategies for fault-tolerant control must be designed as well (Gao, 1996).

While no two systems will likely be rectified in the same way, a general outline for a controller with a reconfigurable or restructurable fault-tolerant control design is presented below in Figure 19 (Lunze & Richter, 2008).

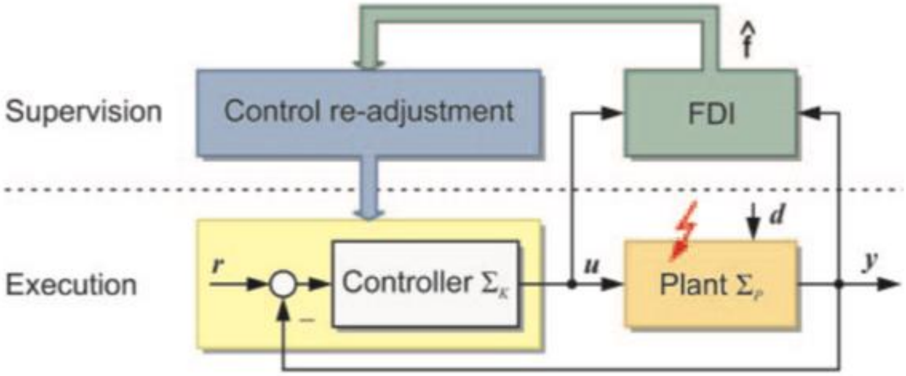

Figure 19. General closed loop control system with FTC

The Fault Detection and Isolation (FDI) module can be seen to be taking input from both sides of the plant. These inputs are then compared, and if a fault occurs in the system, this fault can then be fed to the Control Adjuster, the module responsible for reconfiguration or restructuring of the controls.

The FDI module and the Control Adjuster make up the reconfigurable or restructurable portion of the control system. Some methods for devising a system to satisfy these roles will be discussed below.

The simplest approach for implementing a FTC system is an expert system. An expert system is a system, which ideally knows all the possible failure modes and ways to rectify the control laws to maintain stability of the system (Huang, Celi, & Shih, 1996). The expert system plays the role of both the FDI and the Control Adjuster; however, the expert system can also be used to play the part of either the FDI or the Control Adjuster independently.

The downside of the expert system is that it requires a tremendous amount of overhead research and development work to be accomplished before it can be implemented (Huang, Celi, & Shih, 1996). As the system must "know" every situation that can possibly go wrong, each of these situations must be programmed into the FDI, as well as the relevant signs that such a failure has occurred. Additionally, if such a failure has been identified, then the control responses must be programmed into the Control Adjuster.

This method of FTC is the most primitive, but the simplicity allows for rapid implementation on limited scales. One example of this comes from a 1996 study conducted on the feasibility of reconfiguring a CH-47 "Chinook" helicopter's controls in order to maintain stability of the helicopter (Huang, Celi, & Shih, 1996). Handling qualities were maintained over the course of the study, though only a limited number of configurations and parameters were evaluated.

- Most other solutions to the problem of reconfigurable controls fall into some type of model following system. Many variations exist in these systems, including the Pseudo-Inverse Method (PIM) and explicit/implicit model following. The basic idea behind these types of controls is that the controller attempts to copy the response of some model system that is designed to have desirable characteristics (Dhayagude & Gao, 1996). Through copying the response of this model system, the controlled system is stabilized, which results in favorable handling characteristics. Another advantage of such systems is their inherent applicability to reconfiguration. The ideal model of the system always exists and is tracked by the physical system. Therefore, if some component were to fail in the system, nothing would stop it from continuing to try to track the reference model.

The pseudo-inverse method is a simple control algorithm that essentially works to find a new gain that will provide a "graceful degradation in performance" (Gao, 1996). The nominal and degraded system states are equated, leaving only the degraded gain, or K_f, as an unknown. The following equation is given for solving for K_f using standard state-space nomenclature in (Gao, 1996):

$$K_f = B_f\left(A - A_f + BK\right) \tag{1}$$

Gao (1996) suggests that an expert system may be used for the FDI function, wherein theoretical failure conditions are programmed into the system and their reconfigured gains also calculated beforehand and stored. Alternatively, a system that interprets failures and calculates gains in-flight could be employed. This in-flight reconfiguration cannot guarantee stability, and is a major shortcoming of PIM reconfiguration. Gao lists a few different potential solutions for this weakness.

The explicit and implicit model approaches differ from the PIM approach in what portion of the model is being reconfigured to match the reference model. In PIM, the A matrix of the state space system is reconfigured to more closely match that of some reference model, whereas in the other forms of model following, the trajectories of the systems are matched (Gao, 1996).

A key issue in model following techniques is that of Perfect Model Following (PMF). In order to guarantee that the reference model will be tracked satisfactorily, one needs a guarantee of PMF. The downside of this is that the restrictions placed on the reference model in order to achieve PMF are highly restrictive, and would not allow for any reasonable form of reconfiguration (Gao, 1996). Several solutions to this problem have been proposed, including that by Dhayagude and Gao (1996).

5.1.4.5 Fault-tolerant control and advanced air mobility

Since fly-by-wire control systems will be a staple of AAM vehicles, fault-tolerant controls will play a crucial role in their development.

Though fault-tolerant control methods have been developed on conventional aircraft, little work has been done on implementation in multi-rotor aircraft. A team worked to design a simple reconfiguration system for a CH-47 Chinook helicopter to moderate success as mentioned previously (Huang, Celi, & Shih, 1996). While the CH-47 is a multi-rotor vehicle, it makes use of complex rotor flight controls (cyclic and collective) that are often not found on smaller drones and AAM vehicles.

Stepanyan, et al. (2016) worked to design a FTC that would allow for the successful control of small multi-rotor vehicles after the loss of one or more rotors. If more than one motor failed, the system would automatically enter a safe land mode, and immediately attempt a landing.

There is very little redundancy built into this type of system. Multi-rotors, depending on configuration, use a combination of speeding up and slowing down of their various motors to induce torque on the aircraft, or to create a moment about the pitch or roll axis (Figure 20 (Haller, 2020)). Because of this, if one motor is lost, a significant amount of control authority also goes with it.

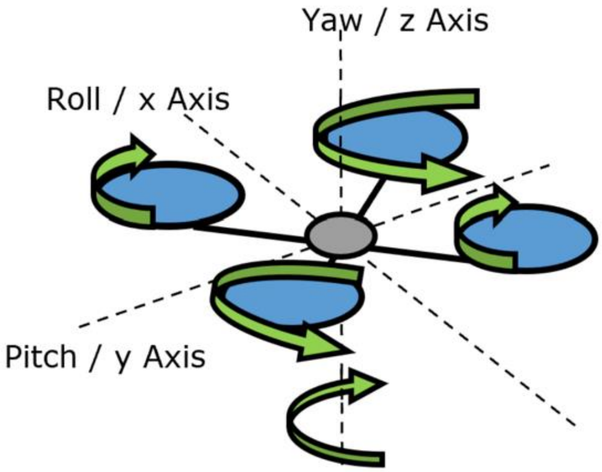

Figure 20. Yaw control for a simple quadcopter (Haller, 2020)

Multi-rotor vehicle fault tolerance can be improved by implementation of collective and cyclic pitch controls. Complex rotor heads capable of cyclic and collective control are often too heavy, complex and expensive to warrant use on a smaller drone, however on larger vehicles they may be justified. Implementation of these controls gives the vehicle multiple control options in the event of reconfiguration. In nominal conditions, a vehicle could perform like a simple multi-copter. In a degraded condition, cyclic control could be utilized to stabilize the system.

An alternative to this can be found in the CH-47 experiment, which notes a previous study, which makes use of small control surfaces positioned on the rotor blades to add control redundancy. Other solutions, like attitude control jets or emergency control moment gyros, could be considered for redundant control.

5.1.4.6 Conclusions of FTC literature review

As AAM vehicles start to enter final design stages, well-designed FTC for these vehicles becomes more of a pressing issue. Due to the nature of their missions and continual close contact with the general population, safe and reliable vehicles are a necessity. Several design concepts were touched on, including the pseudo-inverse method and model following methods, along with expert systems. Methods of implementation in multi-rotors were suggested. Further analysis will need to be done in order to successfully implement such a system in a multi-rotor, however if completed successfully, the benefits could be industry wide.

5.1.5 Summary of literature review

The literature review spanning section 5 covered elements that will contribute towards future handling qualities certification. Some topics of focus were AAM, control allocation, fault-tolerant flight control, and those applications in multi-rotor air vehicles.

Control allocation improves the fault tolerability and modularity of the overall control system, while also allowing for the exploitation of actuator redundancy for improved maneuverability. There are various control allocation approaches, including pseudo-inverse, static, and dynamic control allocation.

In the FTC strategy, the reviewed literature has established that resistance to failure is designed into the system, which can be physical (e.g. failure of an actuator, sensor, or control surface) or non-physical (e.g. software failure or bug in a flight control computer). To achieve such a system, the main strategies used are robustness, reconfigurability, and restructurability.

The literature related to flight FTC and applications to multi-rotor air vehicles revealed that the increasing availability of high-performance computers has made fly-by-wire control systems more popular, but redundancy is required for them to meet an acceptable level of safety. Flight FTC offers a solution to this gap in safety and will be of paramount importance as eVTOL and UAM vehicles mature.

5.2 Task B: Develop dynamic simulation models of DEP units

A dynamic simulation model of the rotor system (Figure 21) was developed in MATLAB / Simulink to predict the performance of the rotors tested in various control strategies. This section will explore the development and operation of the simulation software.

The rotor model aids in understanding the forces and moments produced by the propulsion system of the vehicle and is an integral part of the vehicle dynamic model. The rotor model is validated with forces and moments produced by a rotor on a physical test stand during Task F detailed in Section 5.6.

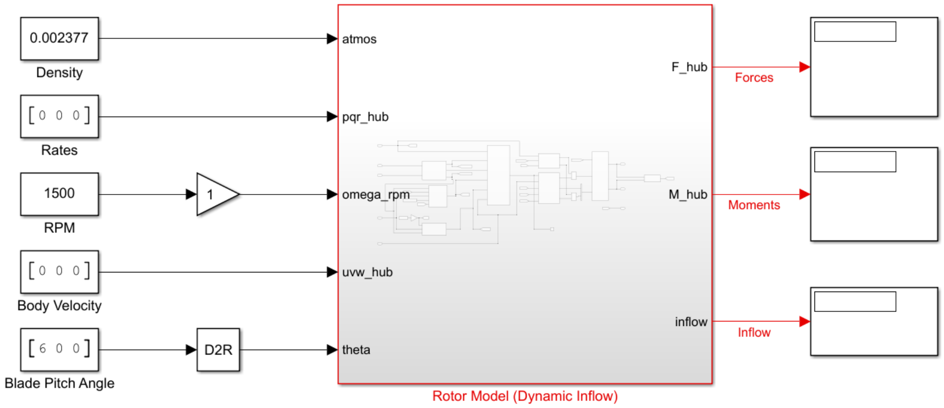

Figure 21. Overview of single rotor unit Simulink model

The model design utilizes closed-form Blade Element Theory (BET) and assumes that the rotor is rigid. The rotor design being modeled utilizes a hingeless rotorhead and the swashplate mechanics allow the blades to experience both collective pitch, lateral cyclic pitch, and longitudinal cyclic pitch. The model was built in the MATLAB/Simulink environment. The Simulink model in its present form assumes that the RPM is constant. In reality, the Electronic Speed Controller (ESC) governs the speed of the motor to a set speed (e.g. 1600 rpm). The RPM can be altered to simulate the rotor being operated in fixed-pitch, where RPM change will be used for thrust control.

The details of the rotor model block can be seen in Figure 22 below. The rotor uses the dynamic inflow methodology to compute the rotor inflow (Peters & HaQuang, 1988).

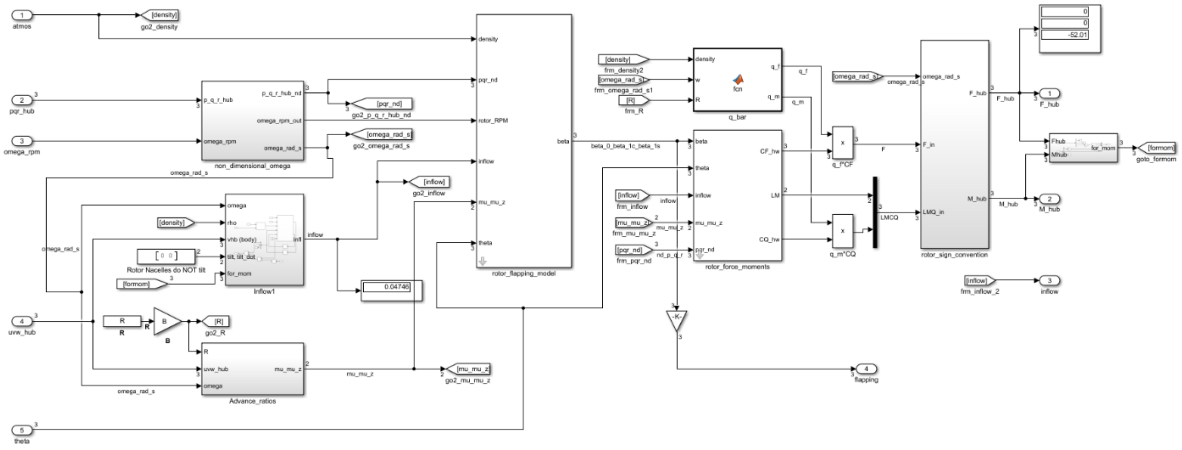

Figure 22. Simulink rotor model block

For a given vehicle with multiple DEP units, the capabilities of each single DEP unit and their effects on the system at large should be assessed. This was achieved by modeling DEP units of various types and control strategies: RPM controlled with fixed pitch rotors, collective controlled with governed RPM, and full collective and cyclic control with governed RPM. Rotorhead mechanical design features such as teetering design, hinge type, blade mount, and blade design were also considered. This methodology is applied in the rotor model.

The EFRC team implemented the concept of a rotor capability model, as depicted in Figure 23, which functions as a thrust and moment generator while closely approximating real-world constraints. Initial vehicle model-level simulation is performed using the capability model for the DEP units, which is a system identification-based approach.

The DEP unit's capability model features a node, which contains a tiltable disk that resembles the cyclic pitch capability and can produce a thrust that acts perpendicular to the disk. The model anticipates thrust and flapping angles along with rotor and environmental constants. A flap spring would create a moment when the disk is tilted. Torque is then calculated using simple momentum theory. Provisions are added to account for lag from the time of requested thrust or disk tilt to achieve a final value.

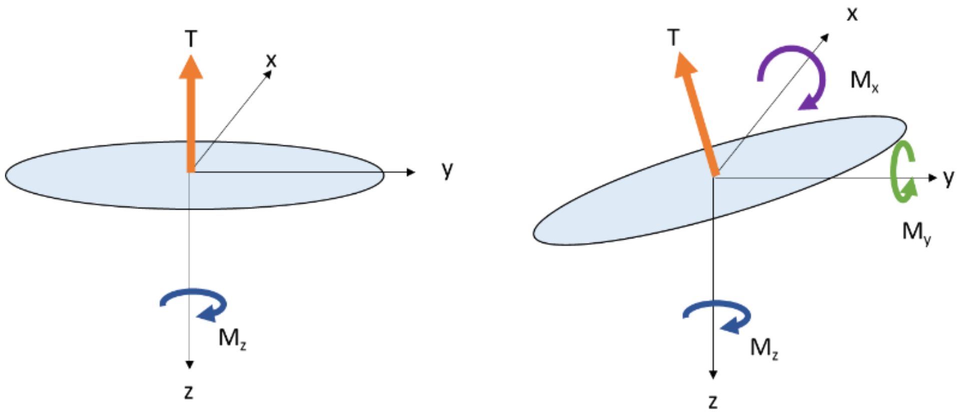

Figure 23. The axis system of rotor disk model

5.2.1 Lessons learned: DEP unit design

In ideal conditions with known external factors, a model would function perfectly. In the real world, there are often external factors such as sensor noise, wind disturbances, and unknown failures that can affect performance. It is therefore crucial to develop a robust dynamic model to mitigate these uncertainties.

BET is a useful tool for analyzing the dynamics of rotor models. The BET equations can be used to calculate the distribution of blade loading across the rotor. Blade element analysis was applied to simulate hover and axial flight conditions to determine the required forces and moments. In hover or axial flight, it is assumed that the flow is axisymmetric and that the flow through the rotor is either upward or downward. To simplify the analysis, momentum theory was used, which assumes that the flow through the rotor is one-dimensional, quasi-steady, incompressible, and inviscid (Leishman, 2006). It is also assumed that the lift coefficient of the airfoil section is constant across the span of the blade, resulting in uniform lift. Additionally, several other minor assumptions were made.

When developing the rotor model, efforts should be made to keep the model as simple as possible while capturing the necessary physics to ensure good model quality. Too many simplifying assumptions would idealize the model to the point of impracticality when compared with experimental results. Uncertain parameter values can be modified within their typical ranges until a good fit between the experimental results and the model is achieved.

5.3 Task C: Develop a parametric N-rotor multi-rotor vehicle simulation model

The process of developing a simulation model for an N-rotor vehicle model begins with a single rotor stage, followed by iterations to validate the simulation against experimental data. The blade element analysis was applied in hover and axial flight to determine the forces and moments required for a single DEP unit, as described in Task-B.

A model was then created to understand the interaction of the rotor systems. As a preliminary step towards the N-rotor vehicle model, a quadcopter Simulink model was designed with the configuration shown in Figure 24.

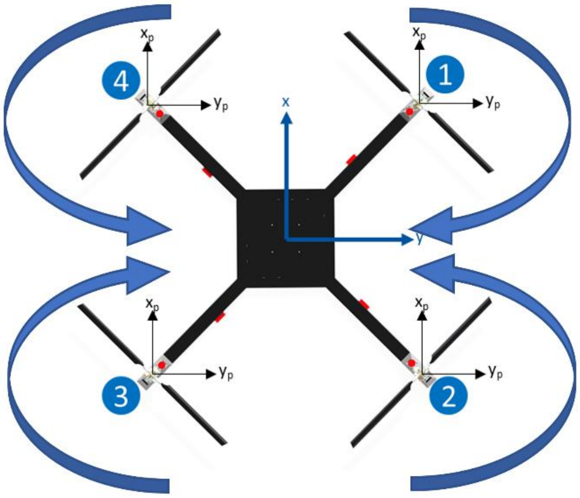

Figure 24. Quadcopter configuration

The forces and moments of each rotor unit are combined to produce the net forces and moments acting on the vehicle. To balance the torque forces, the rotor blades are arranged in an alternating rotation pattern, as shown in Figure 24. The positions of each unit and the center of gravity, where the net forces act, are also chosen accordingly.

The quadcopter model as shown in Figure 25 was created in a way that makes it simple to reconfigure the settings to add more rotors as needed.

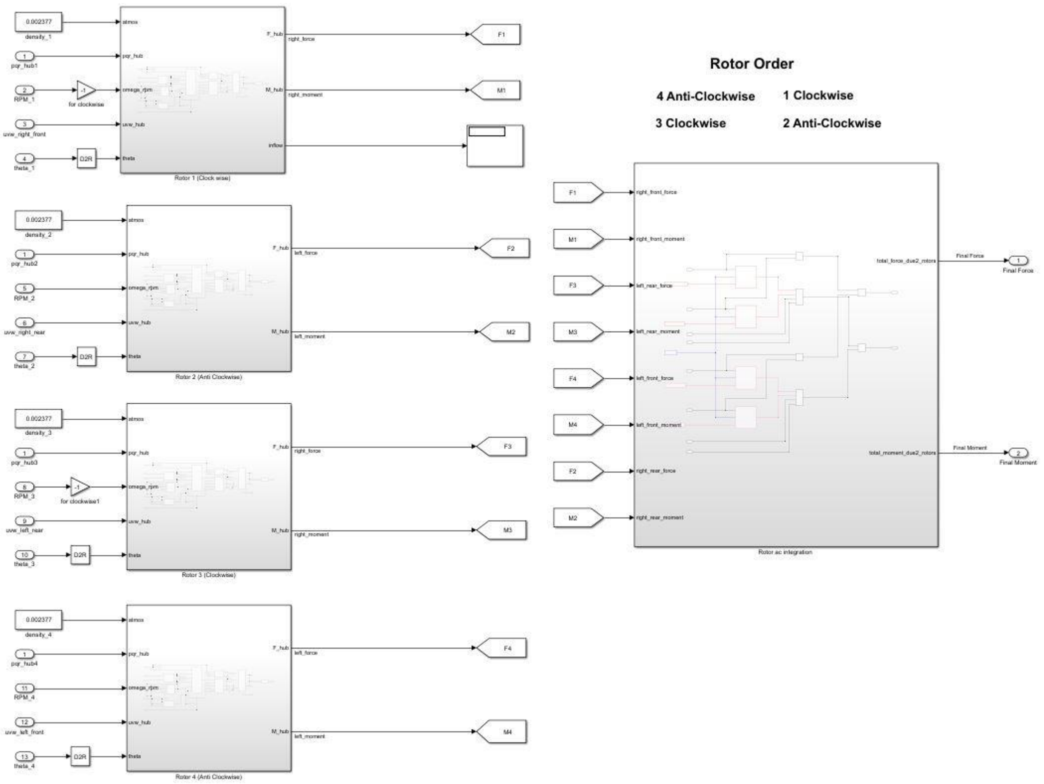

Figure 25. Quadcopter model overview

These units are a component of the dynamic model, which integrates the propulsive forces produced by the rotor units, aerodynamic forces, and external environmental forces acting on the body. While the aerodynamic model could be slightly modified to improve the model's accuracy with measured data, the environmental forces acting on the vehicle would remain constant. The forces and moments block for a quadcopter that generates the net forces and moments acting on the body are shown in Figure 26.

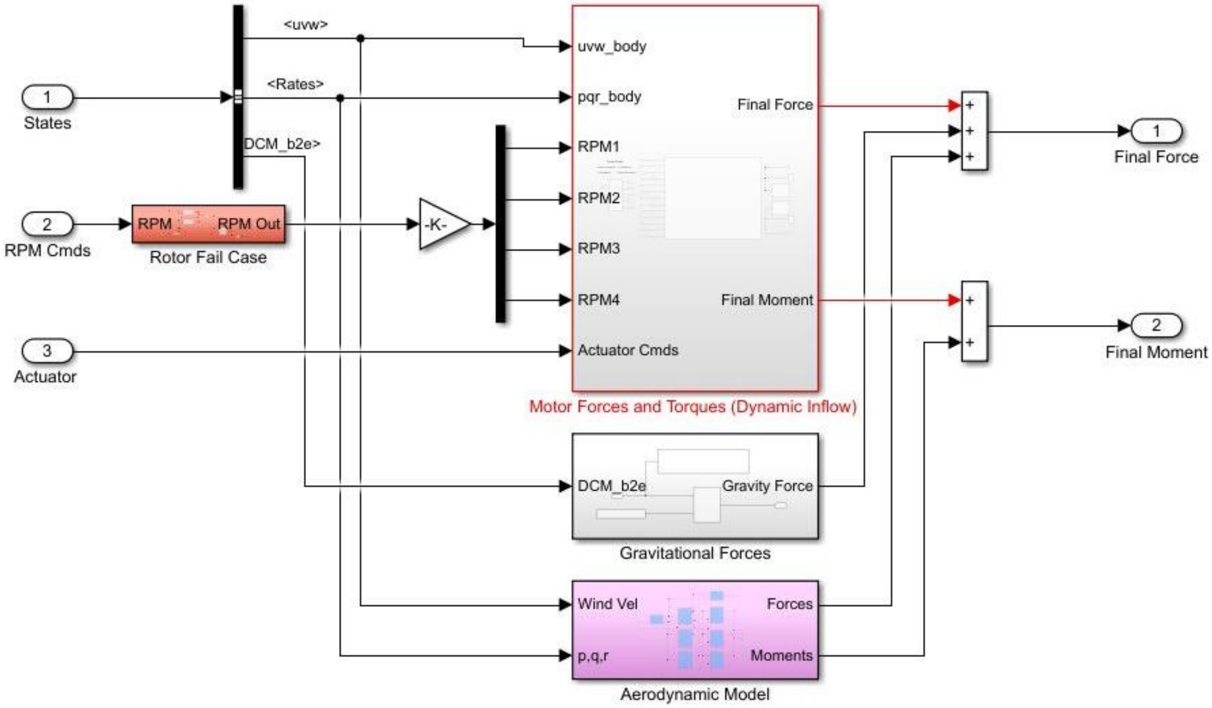

Figure 26. Force and moments block

The mathematical model can be used to depict any moving object, regardless of its shape or mass. A collection of non-linear differential equations was used to define the model dynamics. The rotational and translational subsystems, Euler Angle-Kinematic, and navigation equations are all regulated by a set of twelve ordinary differential equations (ODE) in a standard six degrees of freedom (6DOF) aircraft model. The Simulink model includes twelve ODEs for the quadcopter model, which was used to generate the vehicle simulation for testing as shown in Figure 27.

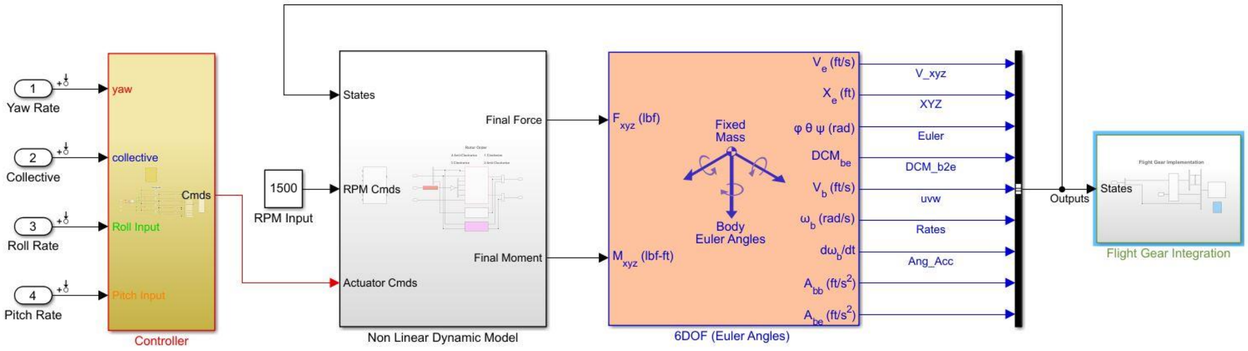

Figure 27. Non-linear dynamic model with controller

To develop an N-rotor model, the quadrotor model was modified with minimal changes to adapt the configuration to any design and any number of rotors. To modify the configuration of the vehicle, the model was introduced with the desired number of units and rotor-integration block settings were updated to account for the moments. Additionally, basic parameters such as the vehicle inertia, mass, and position of units were changed, resulting in the desired N-rotor non-linear model. It should be noted that this model is open loop and does not include a control strategy, which may result in instability.

A closed-loop feedback control system was introduced to control the model. The controller ensured that the vehicle followed reference commands with proximity. The controller in the Simulink model used a set of proportional, integral, and derivative (PID) controllers to control the maneuverability of the vehicle by tracking rate and angle commands. The fine-tuning process can be adjusted to obtain the desired handling characteristics once the controller is in operation.

5.3.1 Lessons learned: Developing parametric N-motor model

It was important to validate the moments of inertia and unit positions while developing the N-rotor model, as these fundamental parameters are critical for the dynamic model to behave like a real aircraft. Once the basic parameters were modified, it was necessary to ensure that the motor mixing algorithms were functioning properly by way of pilot input, actuator, and servo outputs. Additionally, when switching from one parametric N-rotor configuration to another, the control laws were revised and fine-tuned to achieve the desired handling characteristics.

5.4 Task D: Complete build of DEP unit test stand

The rotor test stand (RTS) structure was fabricated in August 2021. Multiple iterations were performed on the hardware and software of the test stand, including the motor mounting options and the telemetry and data acquisition capabilities. Figure 28 shows a CATIA-rendered structural model of the RTS. The geometry of the RTS was designed to eliminate any ground-effect interaction.

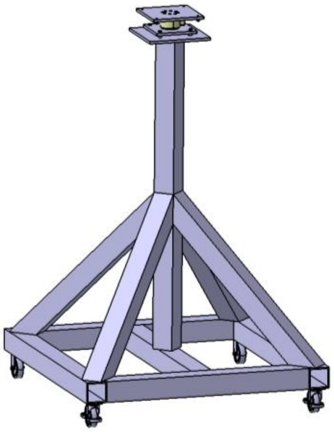

Figure 28. Rotor test stand CATIA design

One of the first major challenges in the development of the RTS was motor mounting, both on the test stand and eventually on a flight vehicle. The test stand provided the ability to test various motor mounting structures, commonly referred to as "units" on the steel plate above the six DOF strain gauge. Figure 29 shows the first attempt at a rotor mount to collect data from the RTS, which involved mounting a helicopter frame with its associated rotorhead mechanics to the load cell plate. As a precaution, the RTS was tethered to the ground and enclosed in a large safety cage for all tests to prevent debris in the event of a catastrophic failure.

Figure 29. First rotor mount attempt

Several tests were run until the diagonal supports buckled due to the intense vibrations during operation, as shown in Figure 30.

Figure 30. Rotor mount supports buckle due to vibrations

The shortcomings of the first rotor mount design provided an opportunity to improve on future rotor mounting. The first unit design was conceived and implemented shortly after the failure of the first rotor mounts. It was constructed with 3003 aluminum side plates bolted to 3D-printed PLA end caps, with the rotor tray nested on top with screws and a 4” square aluminum tube mounted to the bottom. This square aluminum tube would eventually serve as a model for the carbon fiber arms of the first vehicle. The first unit was made much shorter than the first rotor mounting to reduce vibrations. The inside of the unit housed the transmission belt and gearing between the rotor and motor shafts. Figure 31 shows the progression from a cardboard model to a complete assembly.

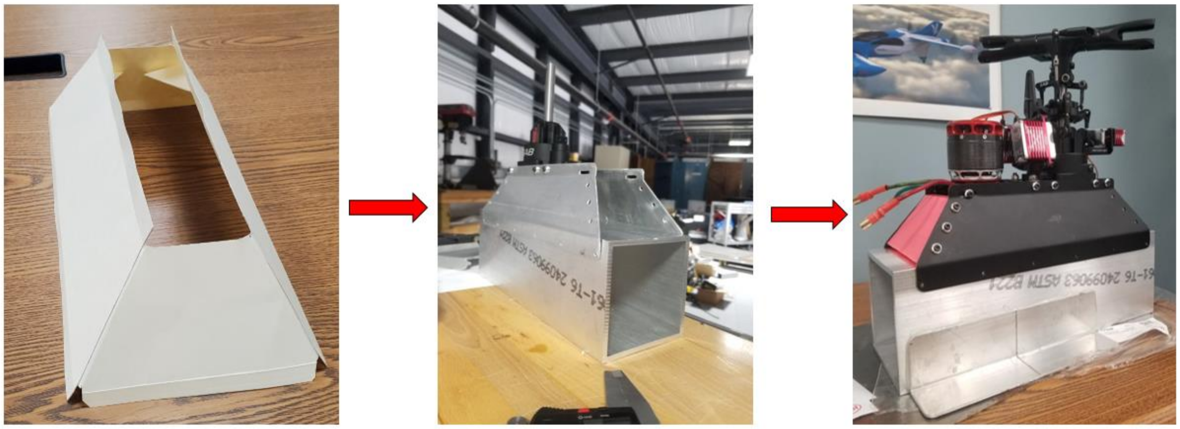

Figure 31. First DEP unit design flow

The first unit, with its 0.04" thick aluminum frame plates, was installed on a 4" square aluminum tube to test the strength of aluminum sheet structures. This prototype unit was then mounted on a spare section of the carbon fiber arm to match the quadcopter vehicle better. After approximately 2 hours of runtime, cracks were observed in the sheet aluminum as shown in Figure 32. To improve the life cycle of the unit, the material thickness was increased to 0.06". Internal 3D-printed arm supports were also installed inside the square tubes for increased strength, as shown in Figure 33.

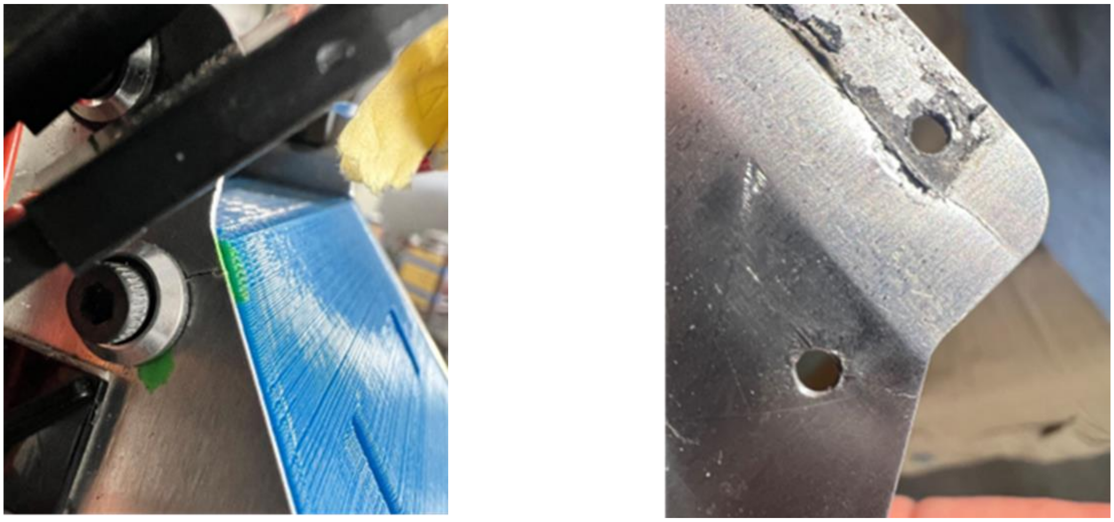

Figure 32. Cracks found on aluminum unit plates after tests

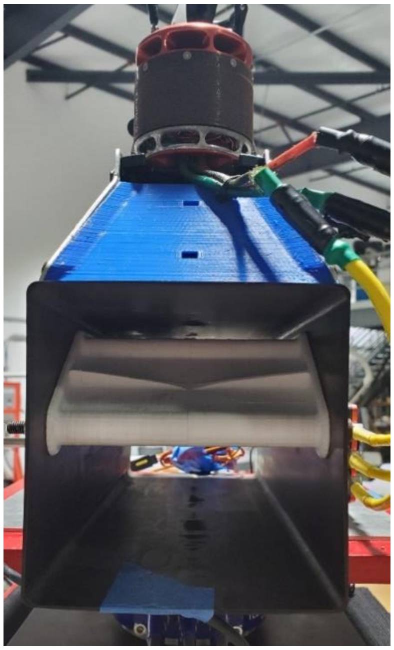

Figure 33. Internal 3D-printed arm support

Finite element analysis (FEA) was conducted on the unit plates to confirm that the areas subjected to the most stress were at the points where the plates ruptured. Figure 34 shows the stress concentration on the plate found with FEA, which matches with the cracks' location shown in Figure 32. This highlighted the importance of providing specific inspection points after each test.

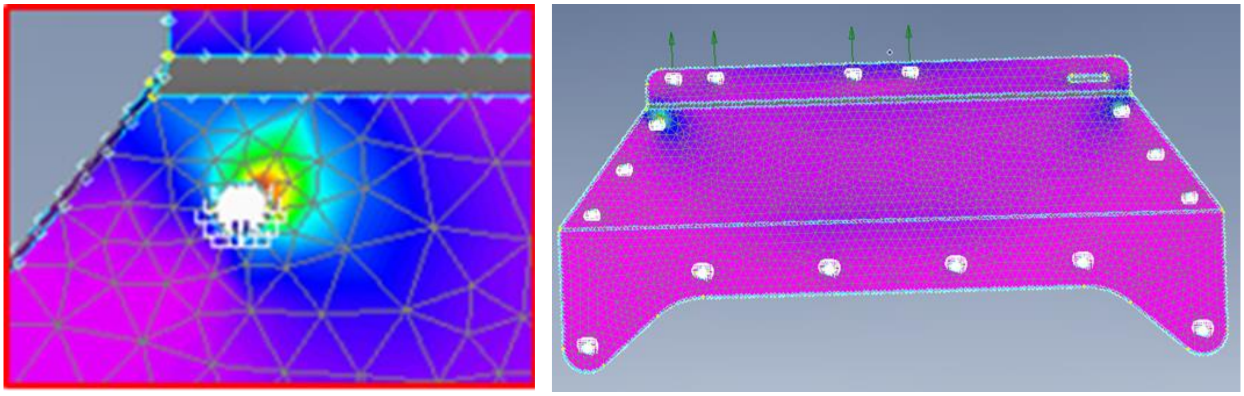

Figure 34. FEA Results on a DEP Unit Plate

Figure 35. Rotor test stand configuration

The RTS data acquisition system was made up of several components which were all combined and can be seen in Figure 35:

- A six degrees of freedom (6-DOF) load cell manufactured by HBM that allows for forces and moments measurements in all three axes (X,Y, Z). The load cell shown in Figure 36 A can measure a vertical force up to 2400 lbs.
- A Quantum X MX840B data acquisition unit, manufactured by HBM, was used for data sampling up to 48 kHz, as shown in Figure 36 B. The Quantum X easily connects to the Load Cell, allowing for a quick setup process, and can read up to eight different channels. The Quantum X device is more powerful than previous data acquisition methods, which were only capable of acquiring data at a 100 Hz sample rate.
- An ACT-3X panel tachometer from Monarch Instrument with a remote optical LED sensor was used to read the RPM of the rotor, as shown in Figure 36 C. The sensor emits a red LED light that is reflected on the reflective tape under the rotating blades. The readings from the sensor are processed and displayed by the tachometer in real-time. A second computer is used to communicate with the tachometer in real-time through the Monarch Instrument custom software, PmRemote. This software allows the user to display the live RPM values on the computer screen and to save the readings in an Excel file for post-processing.
- A speed controller, shown in Figure 36 D, is used to control the motor and to log voltage and current to a micro-SD card. This allows for the calculation of the system's operating power.
- The Catman software was used to interface with the Quantum X to acquire and visualize the data live coming from the load cell. The software environment is shown in Figure 36 E. The data is saved as a mat MATLAB file after every test.

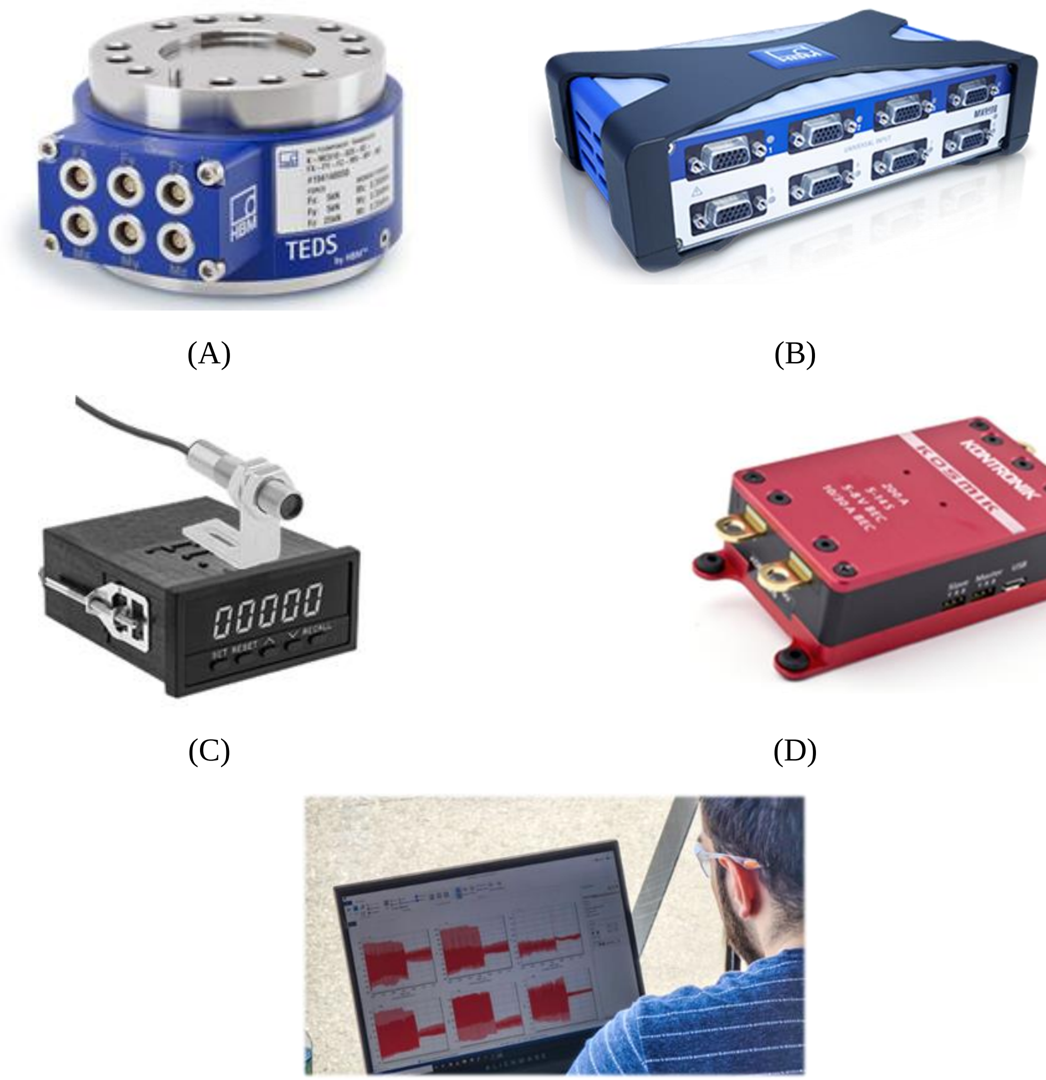

(A) (B)

(C) (D)

(E)

Figure 36. A) Load cell B) Quantum X C) Tachometer setup D) Speed controller E) Catman software environment

To control the commanded RPM and deflections accurately, MATLAB/Simulink was used with an Arduino Mega board to run a programmed sequence automatically. The servos and motor speed controller receive control signals in the form of PWM digital commands from the Arduino and are calibrated to output precise blade angle of attack and exact rotor RPM. The Arduino configuration is shown in Figure 37.

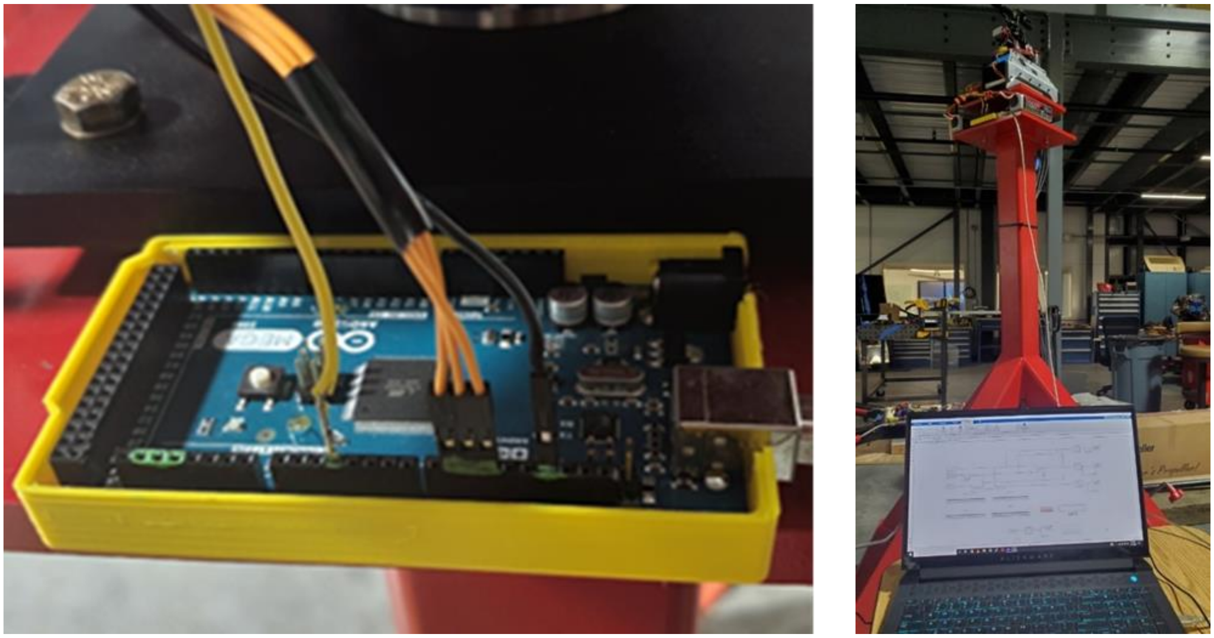

Figure 37. Arduino mega board mounted on test stand

Figure 38 shows the Simulink block diagram used to control RPM and collective pitch. Similar Simulink blocks were used to run sequences for cyclic control. For example, a sequence can be programmed to perform a collective pitch sweep in 2-degree increments from 0 to 12 degrees, followed by a cyclic control sweep at specific intervals, at a specific RPM.

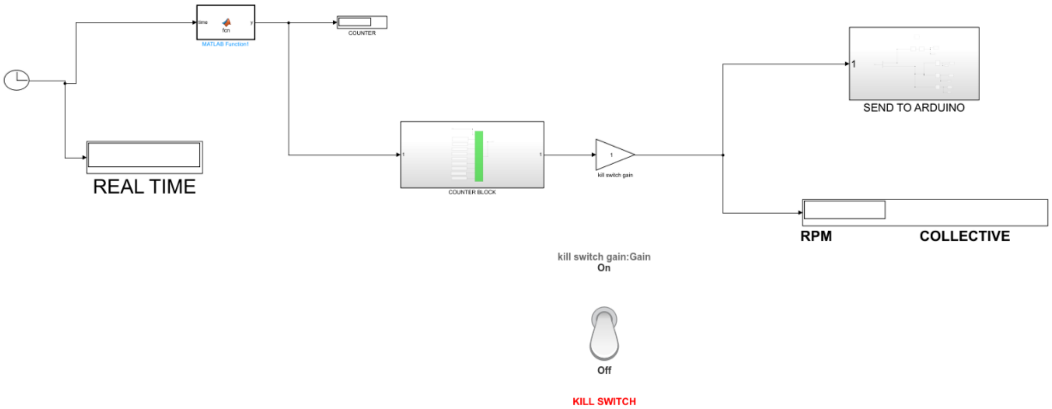

Figure 38. Simulink-Arduino implementation

Two kill switches were installed on the RTS. One kill switch cuts the signal through Simulink and the other kill switch opens the electrical system with a relay as shown in Figure 39.

Figure 39. Relay kill switch

Extensive testing was conducted to characterize a single motor unit. Thrust and torque values were collected initially, while running the rotors at collective pitch intervals from 0° to 13° at different RPM settings. Cyclic control changes were then tested at each collective pitch angle by deflecting the cyclic pitch to simulate an elevator input to command a pitching moment, and then an aileron input to command a rolling moment. Both control deflections were studied from -8° to +8°. Figure 40 shows the axis system for the single motor unit used to analyze the data.

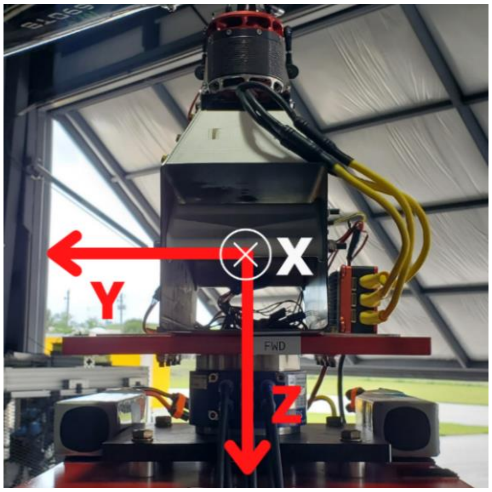

Figure 40. DEP unit axis system

For data post-processing and analysis, a Fast Fourier Transform (FFT) with Butterworth filtering code was developed to isolate the frequencies of interest while removing unwanted noise and vibrations. The plot on top of Figure 41 shows the raw data for the force in the X direction collected from the load cell during a collective sweep test at 1600 RPM, and the bottom plot of the same figure shows the FFT performed on the data. Figure 42 shows the same for the force in the Z direction. As expected, the biggest vibration is picked up in the X-axis, as can be seen by the high peaks in the FFT of Figure 41 against the low peaks of the FFT performed on the thrust measurements, shown in Figure 42.

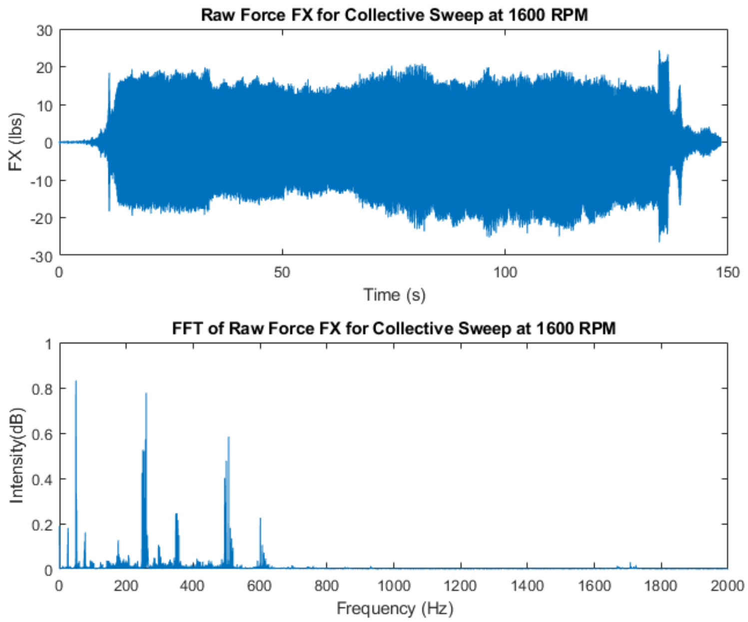

Figure 41. Raw force in X direction and FFT plot

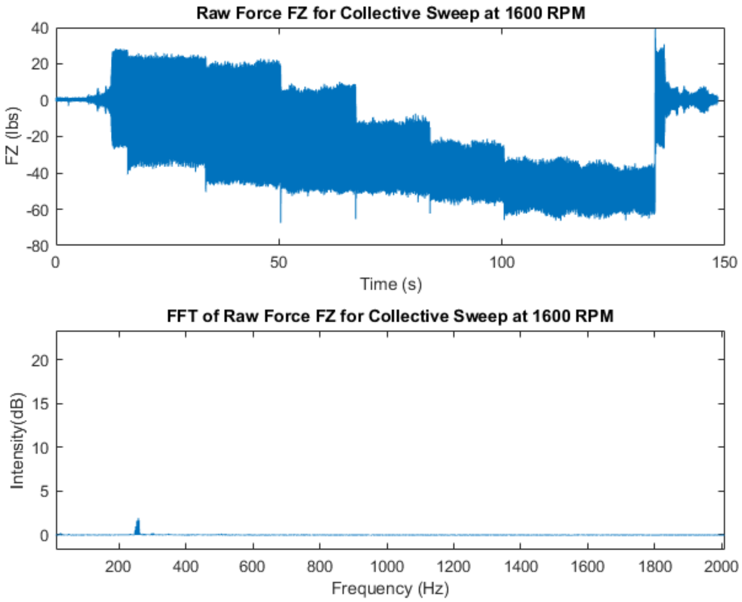

Figure 42. Raw force in Z direction and FFT plot

After filtering the data, clear thrust and moment increments can be seen. Figure 43 shows the thrust data from the collective sweep test at 1600 RPM. The raw data is shown in blue, and the filtered data is shown in red. The green dot shows the maximum thrust generated at 1600 RPM with 13° of collective pitch.

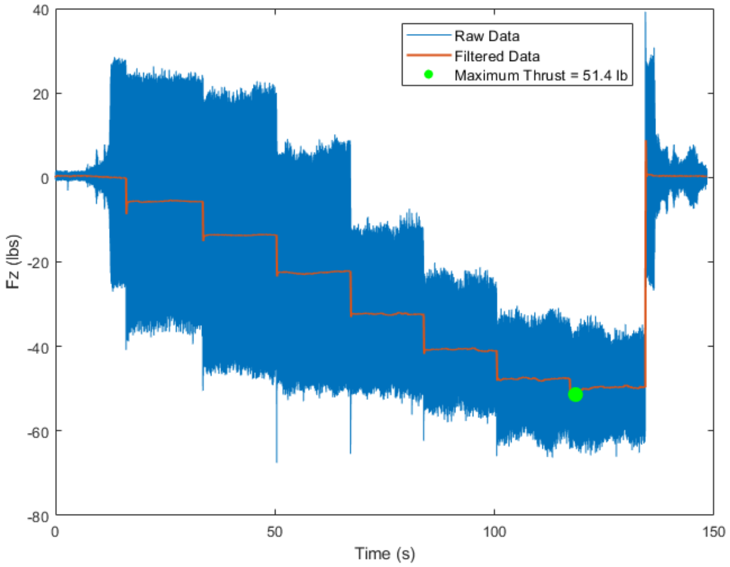

Figure 43. Thrust for collective sweep at 1600 RPM

Torque for the collective sweep at 1600 RPM is shown in Figure 44. The same filter used for the data presented in Figure 44 was used to validate all data from the single MATLAB/Simulink rotor model.

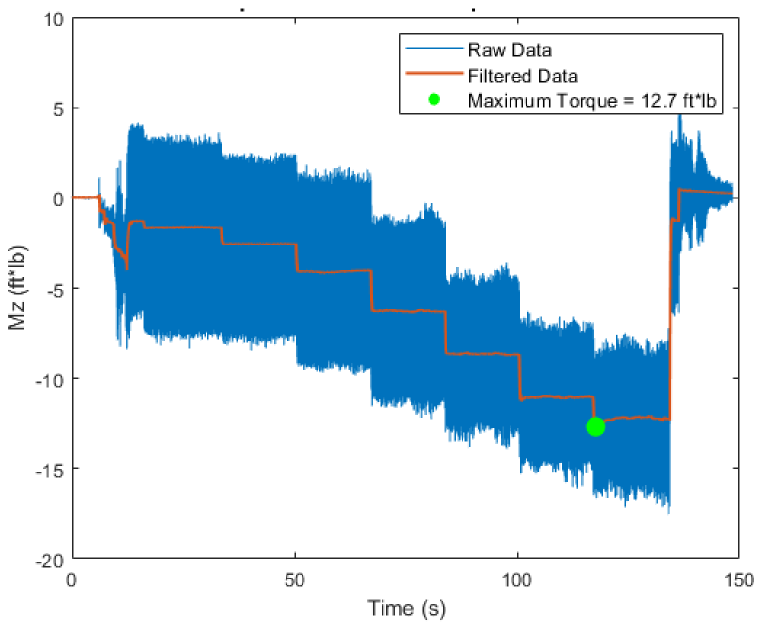

Figure 44. Torque for collective sweep at 1600 RPM

5.4.1 Lessons learned

5.4.1.1 Data acquisition

During the first quarter of the research project, the data acquisition team encountered challenges with the UEI chassis, which was supposed to record data at a sample rate of 8000 Hz over 8 channels but was failing execution past 100 Hz. It was eventually determined that the HBM load cell and the UEI chassis did not work together properly. As a result, the team decided to invest in the HBM Quantum X data acquisition unit, which had already been tested successfully. The team learned that cost-effective, simple solutions like an Arduino board could be as effective in servo and motor control as expensive, specialized hardware.

5.4.1.2 Tachometer

To ensure the most accurate RPM readings, it was determined that the remote optical LED sensor used by the tachometer works best when the angle from perpendicular is 15°. This allows the sensor to record only the light reflecting from the reflective tape on the blades. However, when the collective angle changed during testing, the tachometer angle also changed, which led to the optical sensor becoming less accurate and producing suspiciously high RPM readings. To eliminate these inconsistencies, the ESC was used to log RPM during the most recent tests, with the tachometer serving as additional confirmation. By adjusting the sensor's angle and using the ESC to log RPM, the team was able to obtain more accurate and reliable readings.

5.4.1.3 Simulink-Arduino implementation

To prevent overheating and potential damage to the RTS motor, an automated Simulink-Arduino system was modified to include a manual duty cycle slider for RPM control during testing. Tests now consist of 10-15 different RPM steps, controlled by the duty cycle slider, with a maximum duration of 40 seconds. This minimized the risk of overheating and causing motor damage.

5.4.1.4 ESC

The "Helicopter Mode" on the Kontronik ESC does not effectively compensate for loss of power due to draining batteries, causing the rotor RPM to decrease, and resulting in inconsistent rotor speeds. To address this issue, the RTS team implemented a battery replacement protocol, replacing the batteries with fully charged ones after each test. This helped to ensure more accurate and consistent test results. Future work may involve a deeper characterization of the effect of lower battery levels on rotor speeds.

5.5 Task E: Perform DEP unit testing to characterize thrust and control performance

The following table summarizes the maximum values of forces and moments that characterize the capabilities of a single DEP unit. Table 2 displays the maximum thrust and torque, adjusted for sea level conditions, which obtained from testing the collective pitch range without any cyclic input. These maximum values were achieved at a collective pitch deflection of 13°.

Table 2. Maximum thrust and torque for single DEP unit at a collective pitch of 13°

Max. Thrust	**Max. Torque**	**RPM**
60 lb.	14.6 ft. lb.	1800

Table 3 displays the maximum tested pitching moment that the DEP unit can produce. During testing, the maximum pitching moment value was obtained when the cyclic pitch was set to +8° and the collective pitch was set to 8°.

Table 3. Maximum thrust and pitching moment for single DEP unit at a cyclic deflection of 8° and collective pitch of 8°

Max Thrust	**Max. Torque**	**Max. Pitching Moment**	**RPM**
36 lb.	8.5 ft.lb	19 ft. lb.	1600

5.5.1 Control strategies comparison

To define the time response test, each DEP unit was commanded 20 lbs of thrust, which is the thrust required to make the vehicle hover. The time required to reach that target thrust under different control strategies was compared. MATLAB was used to calculate the time response for both strategies to reach the desired thrust.

A visualization of the required time can be seen in Figure 45 and Figure 46. From the collected data, the collective control strategy was, on average 10 milliseconds faster than the RPM control strategy. A limitation during tests was the spool-up time of the motor. Another limitation was that of RPM control: RPM control strategy testing required a starting RPM of 1200; a starting RPM of 0 spooling up to 1600 RPM would burn out the motor. Figure 46 shows an indicated initial thrust of 10 lbs, which reflects this. Even with this initial advantage in thrust, the RPM control strategy could not perform as quickly the collective control strategy. With these disadvantages in motor control and time response, the RPM control strategy was decidedly inferior to the collective control strategy.

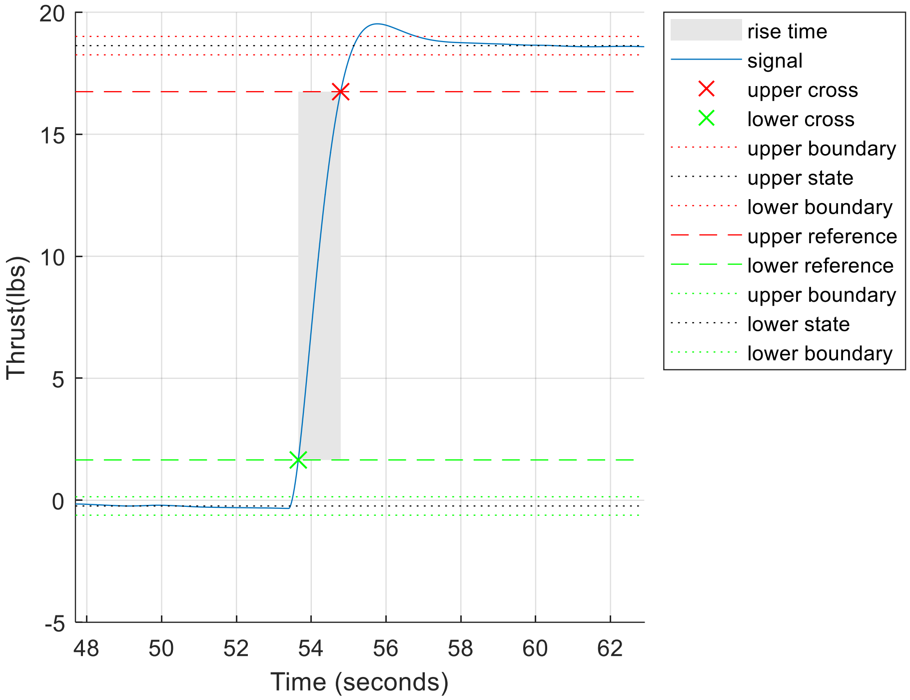

Figure 45. Collective control strategy rise-time

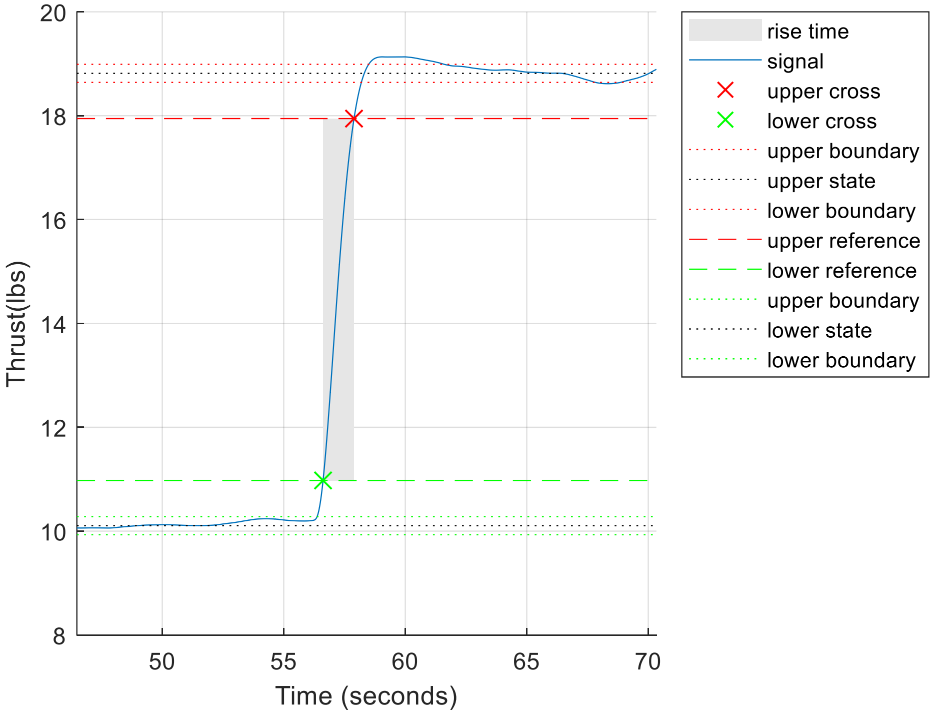

Figure 46. RPM control strategy rise time

5.5.2 Thrust performance characterization

The single DEP unit testing data has been compiled to create a user-friendly MATLAB function that utilizes 3D lookup tables and interpolation to show a relationship between thrust, collective, and RPM. This function allows users to access the capabilities of the DEP unit and plan test accordingly. Figure 47 shows a 3D interpolated graph of the thrust data.

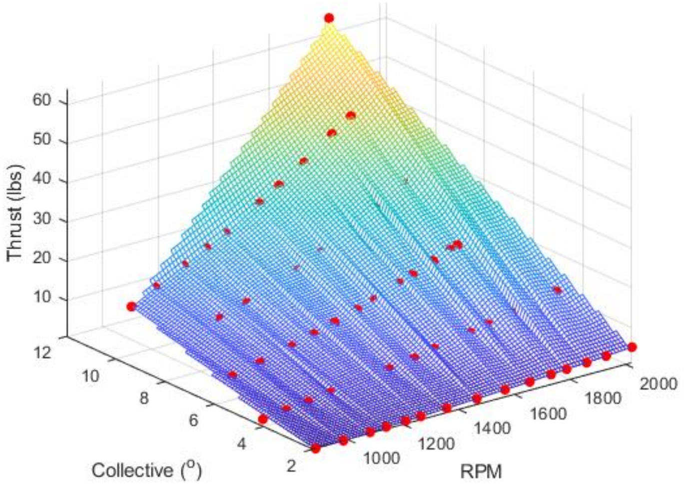

Figure 47. 3-D interpolated thrust figure (governor in helicopter mode, 18 tooth pinion,)

These functions can be used in the MATLAB/Simulink rotor models to provide realistic values for future applications and further model validation.

5.5.3 Blade comparison

Different blades in a 2-blade configuration were tested against a 3-blade rotorhead configuration on the RTS. Figure 48 shows all the blades tested.


REVO SAB VTX HANTZ

Figure 48. All blades tested

The SAB, Hantz, REVO, and VTX blades were all tested for their thrust and power requirements at a collective pitch of 10°. The SAB blade is a rectangular blade that was used in a two-blade configuration on the PAVER vehicle. The Hantz blade has a tapered and twisted design, created at the EFRC for low-noise applications. The REVO blade is a longer and thinner rectangular blade, while the VTX blade is tapered with a larger blade area at the 75% radius. Figure 49 shows a comparison of the thrust generated by each blade. Figure 50 compares their power requirements.

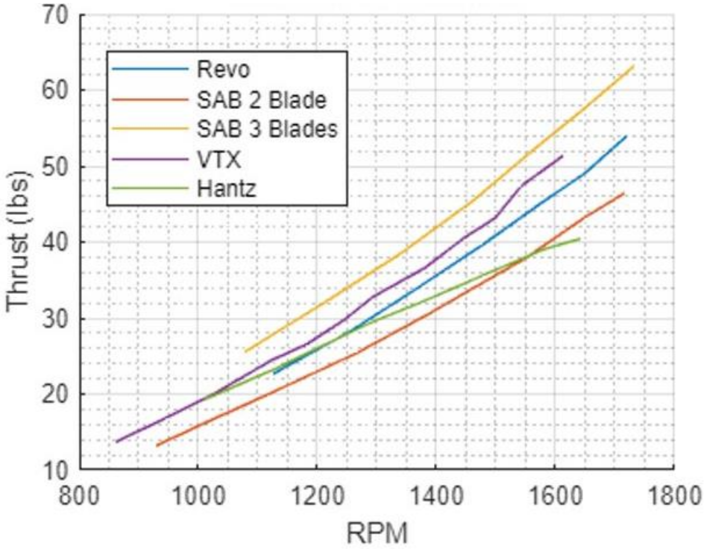

Figure 49. Thrust comparison of different blades at 10° collective pitch

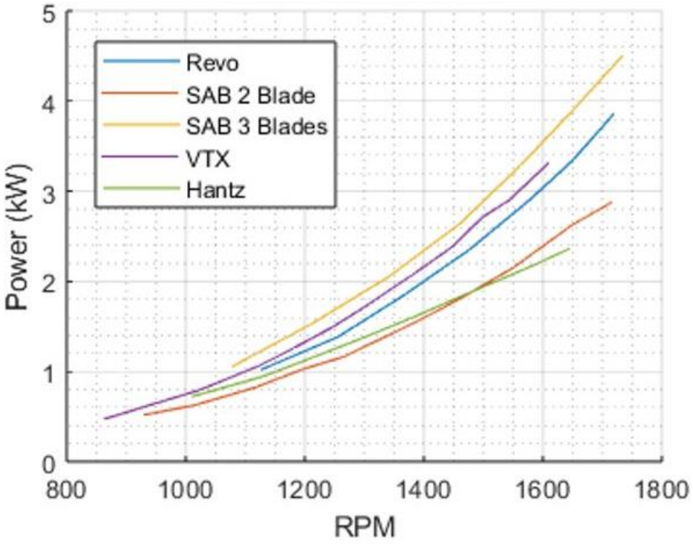

Figure 50. Power comparison of different blades at 10° collective pitch

The 3-bladed rotorhead generates more thrust at the cost of required power. Cyclic tests were performed for all the blades by commanding longitudinal cyclic to produce pitching moment. Figure 51 shows the moment generated at 6° collective with 6° cyclic deflection. Figure 52 shows the power required.

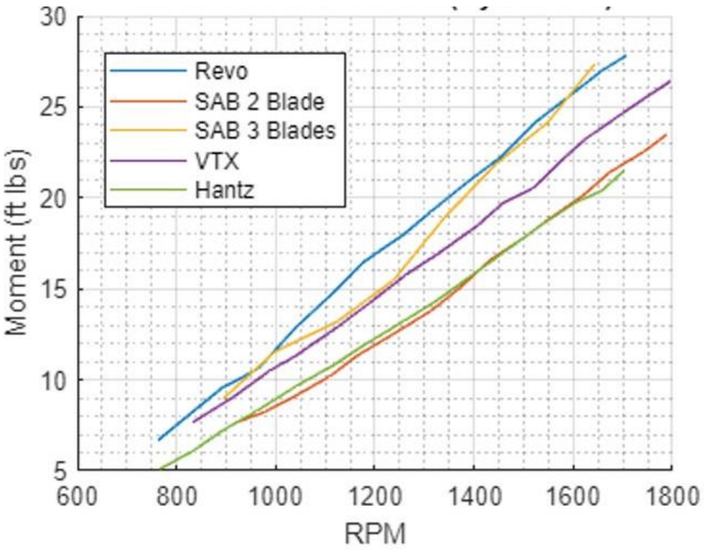

Figure 51. Moment comparison at 6° collective and 6° cyclic

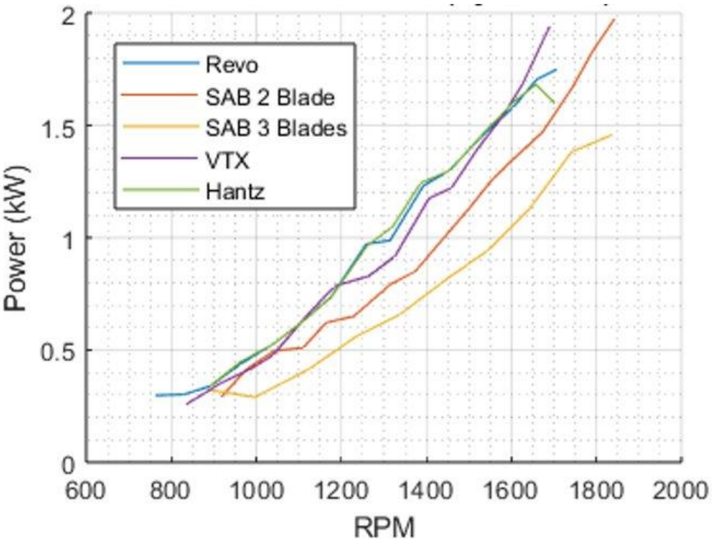

Figure 52. Power comparison at 6° collective and 6° cyclic

The 3-bladed rotorhead configuration was found to be the most effective in thrust-to-power efficiency. At lower RPM, this configuration generated higher thrust and produced a higher cyclic moment with a lower power requirement compared to the other setups tested.

5.6 Task F: Validate DEP simulation model with test data

The experimental values were compared to simulation values from the US Army Rotorcraft Comprehensive Analysis System (RCAS) and a custom MATLAB/Simulink model. Both sets of simulation values were consistent with the experimental values. Appendix A contains the experimental and simulation data with percent error calculations for the collective sweep tests. Figure 53 through Figure 56 present data from collective sweep tests performed at different RPM values, compared with the MATLAB/Simulink rotor model.

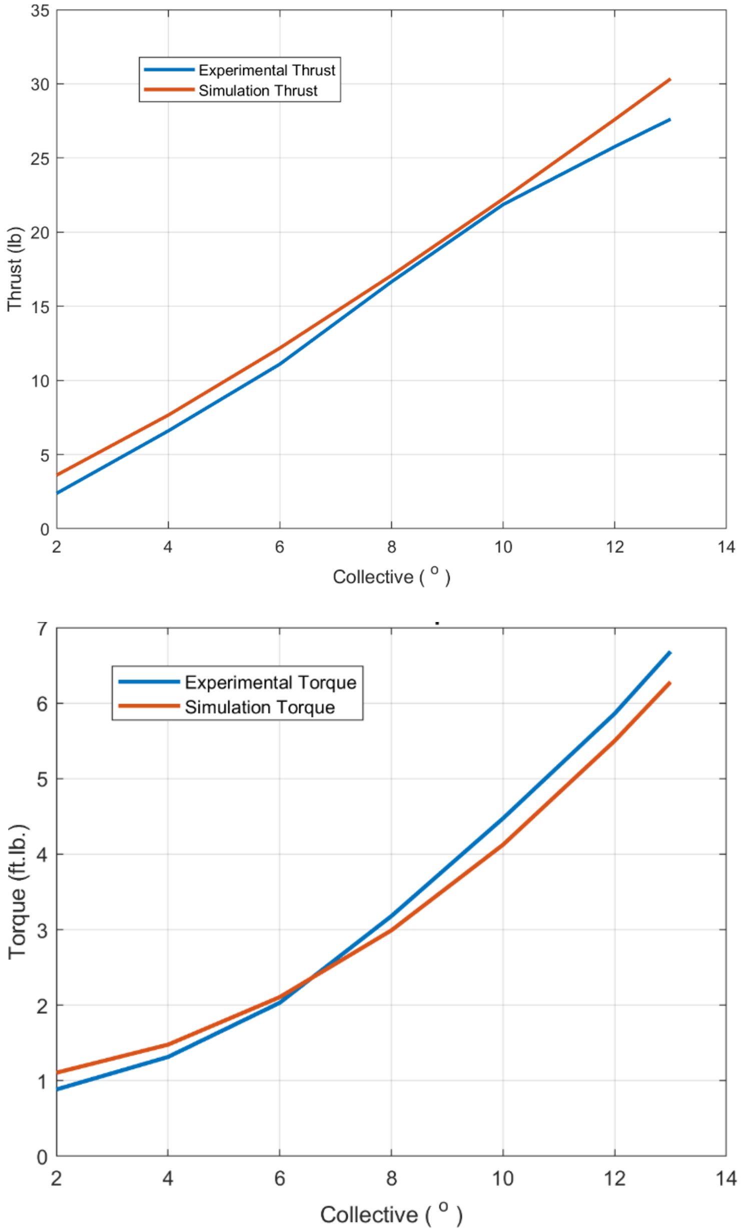

Figure 53. Collective pitch vs thrust (top) & collective pitch vs. torque (bottom) at 1200 RPM

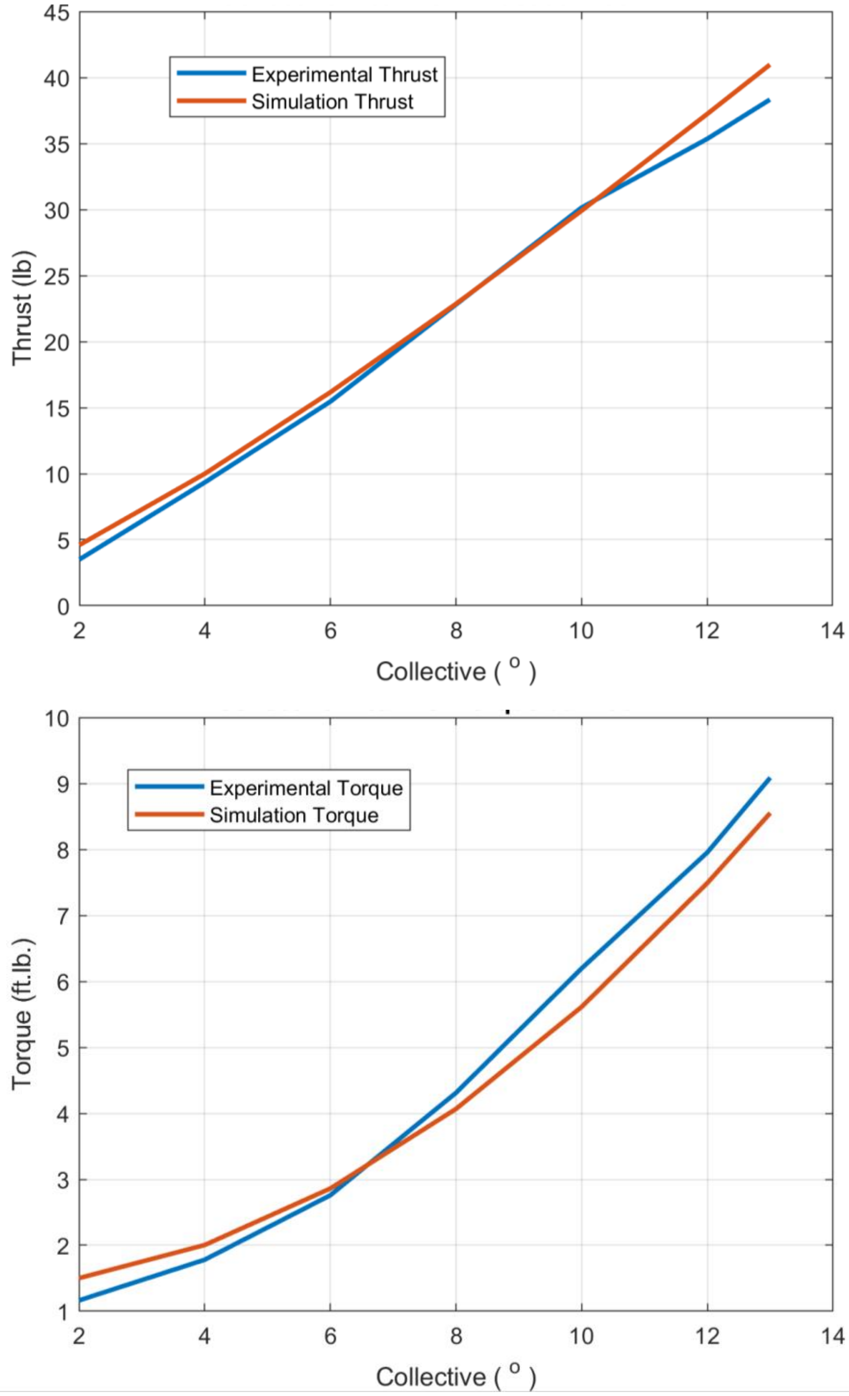

Figure 54. Collective pitch vs thrust (top) & collective pitch vs. torque (bottom) at 1400 RPM

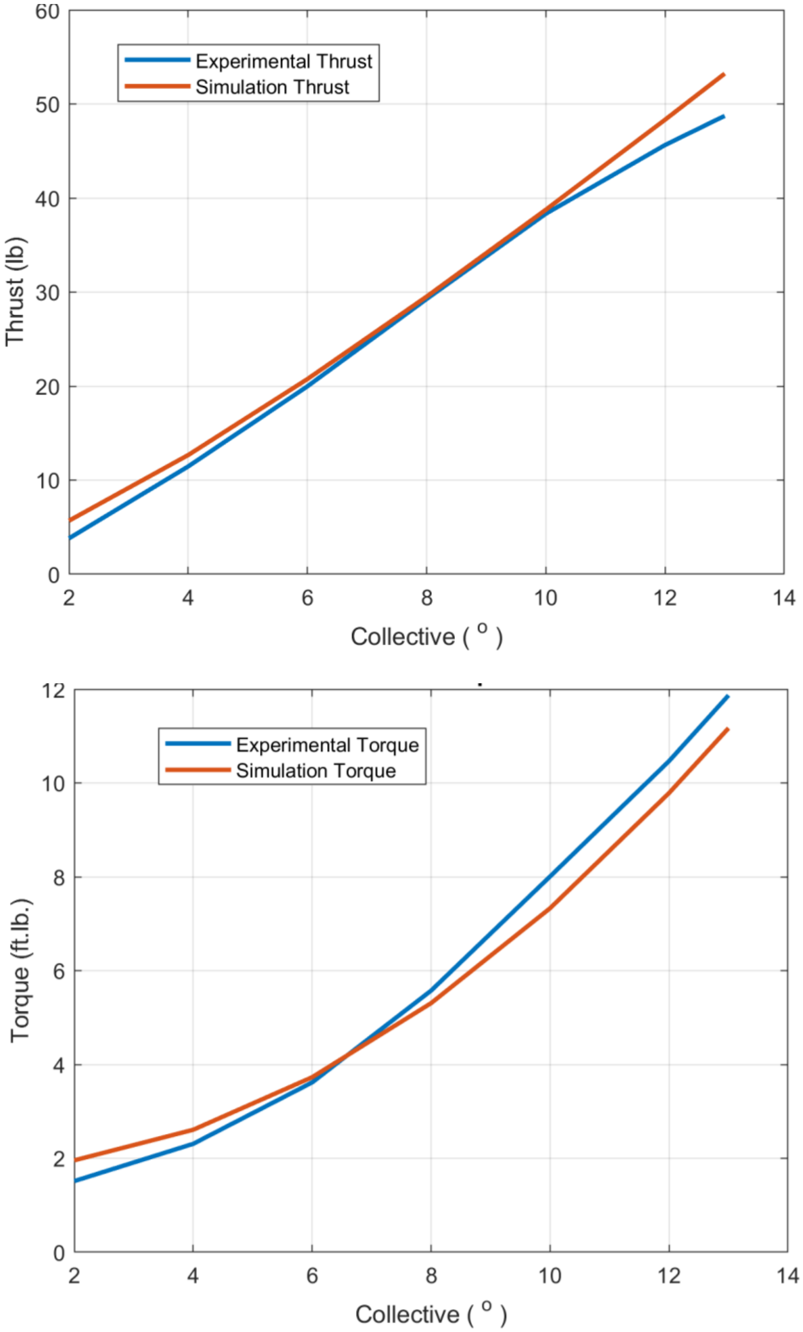

Figure 55. Collective pitch vs thrust (top) & collective pitch vs. torque (bottom) at 1600 RPM

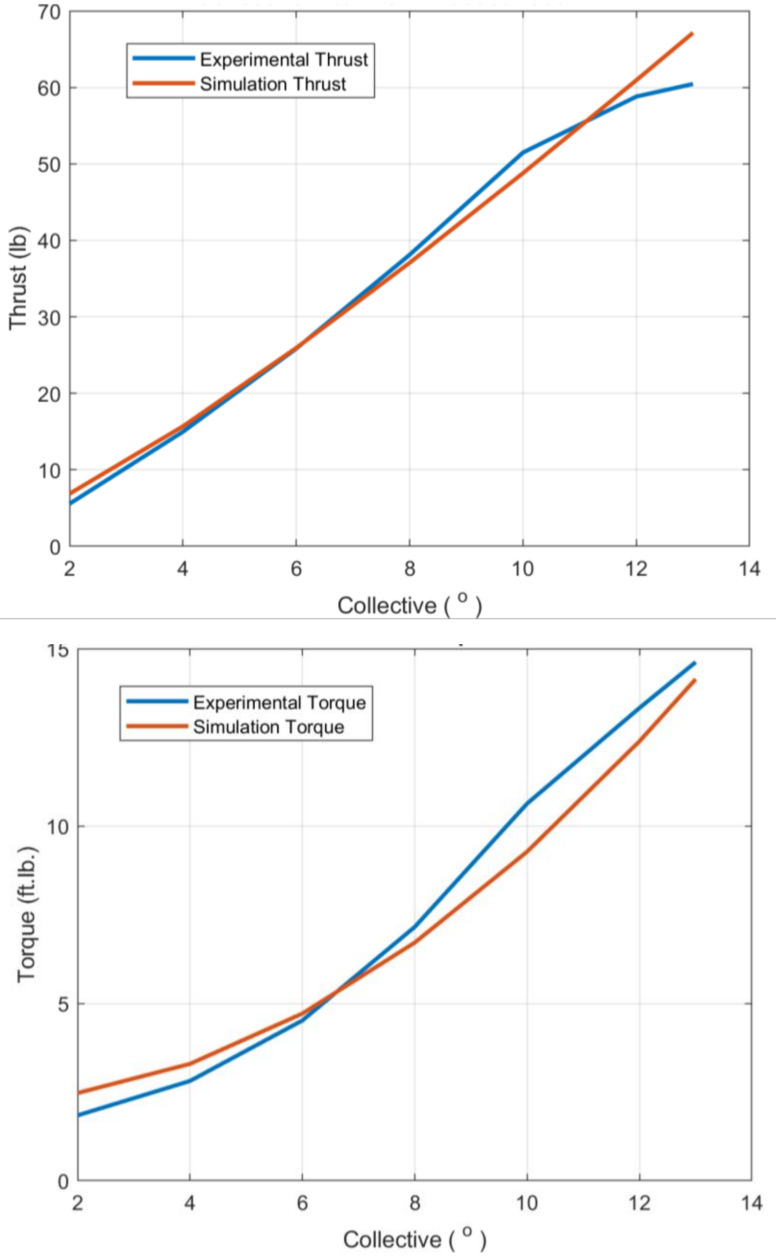

Figure 56. Collective pitch vs thrust (top) & collective pitch vs. torque (bottom) at 1800 RPM

The experimental and simulation results for the collective and cyclic sweep tests show strong correlation, with a small difference in torque values. The figures below compare the experimental results for pitching moment (Figure 57) and rolling moment (Figure 58) for a cyclic sweep test in elevator deflections at a constant collective of 6° at 1200 RPM. The off-axis moment generated, or, rolling moment, also exhibits strong correlation with the simulation results. Similar positive trends were observed in tests with higher RPM and different collective values in the elevator cyclic tests.

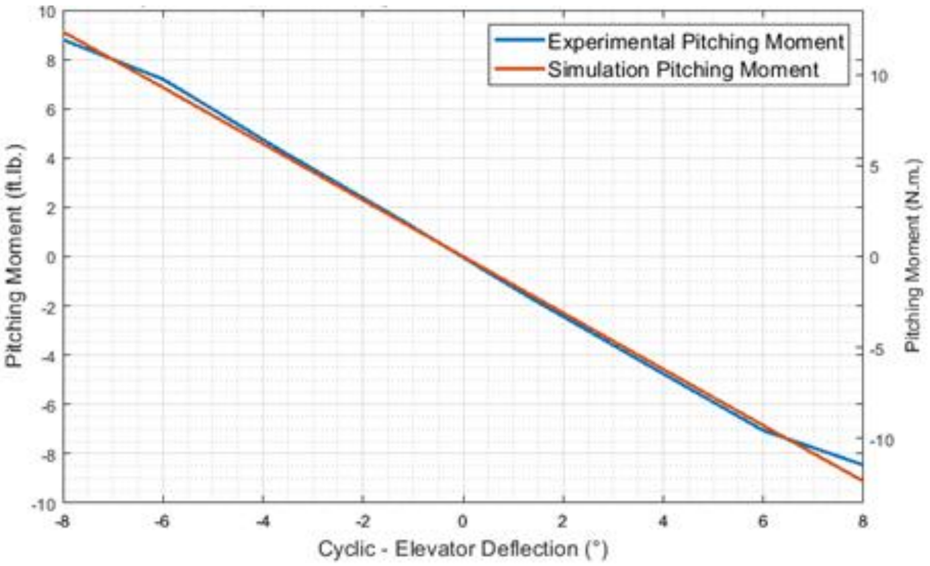

Figure 57. Pitching moment for elevator sweep test at 1200 RPM and 6° collective

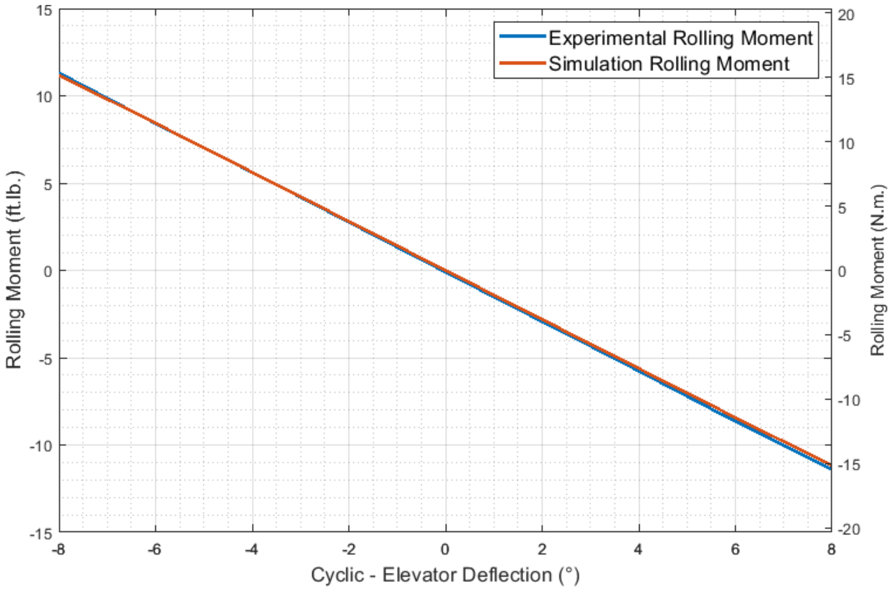

Figure 58. Rolling moment for elevator sweep test at 1200 RPM and 6° collective

5.7 Task G: Complete build of PAVER testbed

5.7.1 Hardware build

The first PAVER testbed was designed with a carbon fiber airframe consisting of carbon fiber plates and hollow square tubes, as shown in Figure 59. The square pipes were sandwiched between two sheets of 4mm thick carbon fiber baseplates and were bonded together using Hysol 9430 glue. The DEP units were made from aluminum sheet-metal plates that couples the rotor assembly to the arm attachments. To prevent buckling, the units were equipped with 3D-printed endcaps and inserts. The units were mounted at the end of each arm, placed 5’ from the center of the vehicle, and 7’ from the adjacent rotors. The electronic speed controller was mounted on the side of the arm to minimize the length of battery and motor wires. The signal wires were shielded to avoid potential interference from the motor wires.

Figure 59. The DEP units are assembled on the end of carbon fiber square tubes

The prototype of the PAVER system shown in Figure 60 was secured to the ground for a run-up test. The servo wires were connected to a PowerBox Competition SR2 unit, which supplied power to the servos and distributed PWM signals to each servo. The PowerBox was powered by two standalone 2-cell (2S) batteries, providing 8 volts to the servos to enable high speed and high torque operation.

Figure 60. PAVER V.1 strapped on the ground for testing

During the first test flight of the PAVER V.1, two DEP units experienced structural failure. The aluminum side-plates experienced a bearing failure, in the form of tear-out, at the mounting bolt holes, causing the rotorheads to detach. There was a noticeable vibration before the incident occurred. One theory was that ground resonance might have been the source of the vibration, leading to the twisting of the arms and eventual failure of the structure. The carbon fiber arms with 0/90-degree lay-up were able to withstand bending moments but were not as torsionally rigid. This theory led to a series of tests on arms with different geometries, lay-up directions, and methods of reinforcement.

Figure 61 illustrates the setup for these tests. A single test arm was mounted on a heavy welding table. A moment arm was clamped perpendicularly to the end of the DEP arm, where force was applied by an engine hoist. The applied force was recorded using a digital scale, and the resulting twist angle was measured with a pitch gauge mounted inside the DEP arm. The torsional rigidity of different DEP arm configurations was obtained by calculating the slope of the moment applied versus the twist angle along the axial direction.

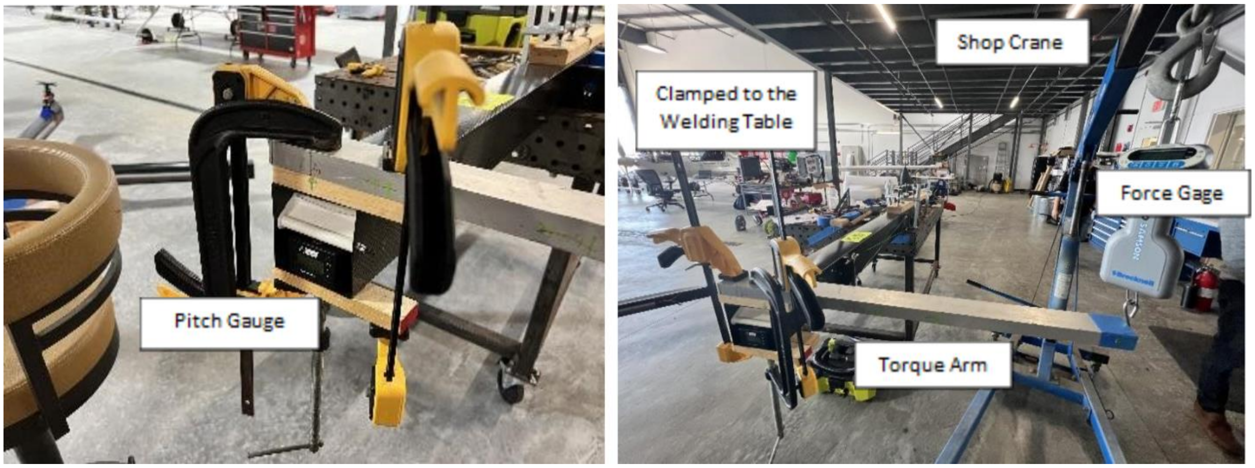

Figure 61. The test set-up for carbon fiber tube torsional rigidity

To increase the torsional rigidity of the DEP arm, several reinforcement methods were assessed, including the use of internal inserts, external tension wires, and replacing the square tube arm with a circular tube. At the initial condition, with no reinforcements installed, the torsional rigidity (q) of the original square tube was calculated to be $353 \frac{lbs\cdot in}{degree}$, based on the shear modulus (G) of the carbon fiber, which was calculated to be $2.4 \cdot 10^5\ psi$ from the torsion test data shown in Figure 62. For comparison, a typical carbon fiber with 0/90-degree lay-ups and the lowest quality listed in the material database (Granta EduPak) has a G value of $7.28 \cdot 10^5\ psi$. This indicates that the original tube had a very low torsional rigidity, which was not anticipated during the design phase as the primary focus had been on bending, for which the 0/90-degree lay-up was deemed sufficient.

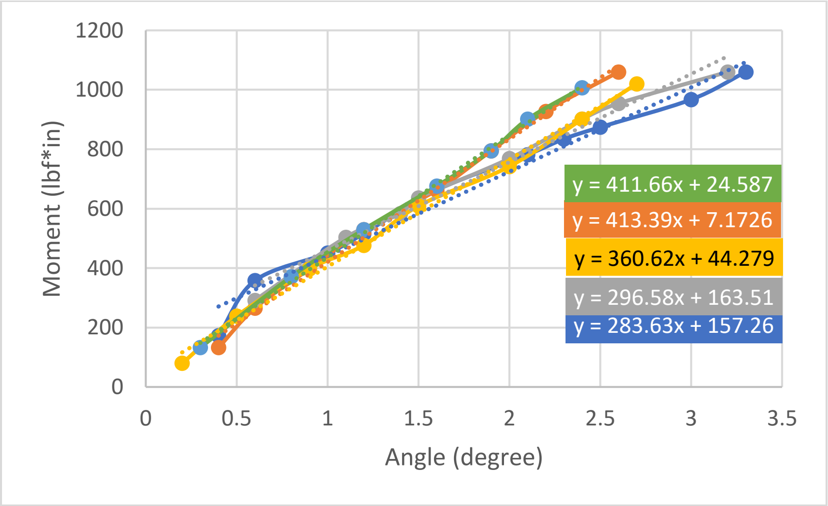

Figure 62. Moment vs twist angle (original square tube). Slope indicates the torsional rigidity

The torsional rigidity was improved by using a tube that included 45° fibers in the lay-up, which increases shear strength on a plane. The relationship between torque, torsional rigidity, and shear modulus can be expressed in the equation below.

$$T = q \cdot \theta, \;\; q = \frac{4A^2Gt}{LD_{Perimeter}} = \frac{T}{\theta} \tag{2}$$

$q = Torsional\ Rigidity,\ G = Shear\ Modulus\ (psi),\ A = Tube's\ open\ area,$
$L = length\ of\ the\ arm, D_{perimeter} = length\ around\ the\ tube,\ t = thickness,$
$\theta = Torsional\ Angle$

Several 3D-printed bulkheads were added to reinforce the tube to increase the torsional rigidity. An example of 3D-printed frames and their locations are shown in Figure 63.

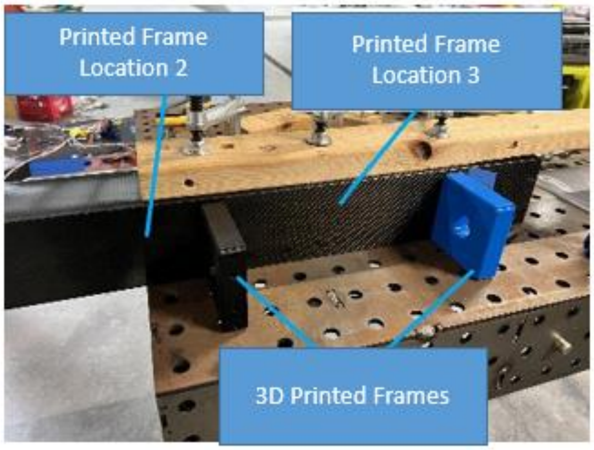

Figure 63. Example of 3D-printed frames and their locations

For non-thin wall tubes, the area moment of inertia of the cross-section plays a role in determining the torsional rigidity. Therefore, it was decided to purchase a circular carbon fiber tube with a thicker wall thickness and a 0/45/90-degree lay-up, with the assumption that the G value would be $2.4 \cdot 10^6\ psi$ based on similar carbon fiber data. When the new tube arrived, a torsion test was conducted again, as shown in Figure 64.

Figure 64. Test setup of the carbon fiber drive shaft

Round tubes provided significantly higher torsional rigidity, however their circular shape posted mounting problems on the test rig. During the torsion test, rubber bands were placed around the pipe beneath the 3D-printed clamp to prevent slipping, as shown in Figure 65. The deformation of the rubber bands indicated the torque applied, as the rubber bands exerted equal and opposite distributed forces on their surfaces. Therefore, the deformation of the rubber bands accurately reflected the torque applied.

Figure 65. Twist angle indicated on the pitch gauge

A new arm test stand was designed and built to test the circular tube unit's mounting and vibrations. The prediction of the new round tube's torsional rigidity was relatively close to the test results, with an obtained G value of $2.19 \cdot 10^6\ psi$ and a q value of $1556\ \frac{lbs \cdot in}{degree}$.

The torsional rigidity of the circular tube was approximately four times higher than that of the original square tube. Figure 66 shows a comparison of the q values for four different data points:

the original square tube, the square tube with 3D frame reinforcements installed, the circular tube prediction, and the experimental circular tube.

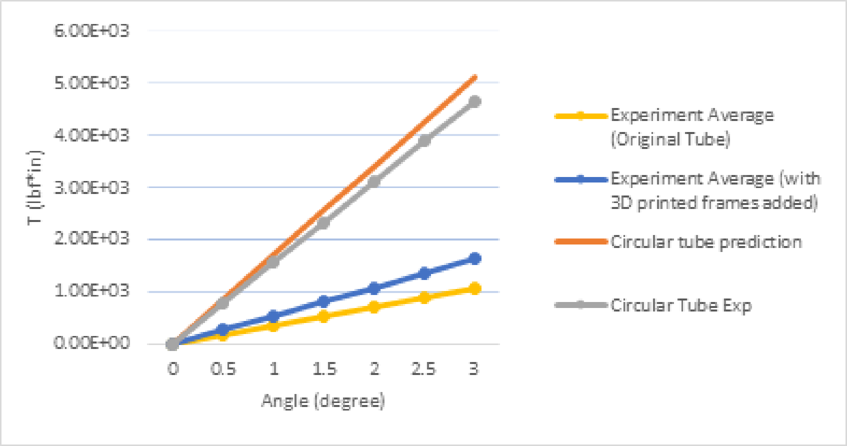

Figure 66. Torque twist test results and prediction

The steeper the slope in the torsion test data, the higher the torsional rigidity. For the same cross-sectional shape, a steeper slope also indicates a higher G value. However, the improvement in torsional rigidity and shear modulus comes at the cost of added weight. The original arm had an average weight of 3.3 lbs each, while the new round tube weighs 5.8 lbs. This translates to an additional approximately 10 lbs of weight for the PAVER system. The slopes obtained from the torsion tests were used to calculate the q values, which are presented in Table 4.

Table 4. Torsional rigidity (q) values obtained

Torsional Rigidity	**Original Tube (Twist Test)**	**Original Tube with Plastic Frames (Twist Test)**	**New Circular Tube Predicted**	**New Circular Tube (Twist Test)**
$\mathbf{q}\left(\frac{\mathbf{lbs \cdot in}}{\mathbf{degree}}\right)$	353	541	1707	1556
$\mathbf{q}\left(\frac{\mathbf{lbs \cdot in}}{\mathbf{radian}}\right)$	$20.2 \cdot 10^3$	$31.0 \cdot 10^3$	$104 \cdot 10^3$	$278 \cdot 10^3$

The natural frequencies for three modes were calculated using the torsional rigidity values obtained. The "longitudinal" mode refers to tension-compression, the "lateral" mode refers to bending, and the "torsional" mode refers to the twist of the arm. This study was conducted to investigate the potential resonance due to the first mode of the natural frequency matching the rotors' RPM. As shown in Table 5, the torsional natural frequency obtained for the original arm configuration was 1641 RPM, which is very close to the RPM at which torsional vibration was observed during the tethered test flight.

Table 5. List of natural frequency values for different modes

Operating RPM ~ 2,200	**EQUATION**	**ORIGINAL TUBE**	**ORIGINAL TUBE WITH FRAMES**	**ROUND TUBE**
$\omega_n, torsional$ (TWIST)	$T = q \cdot \theta, I = m \cdot l^2,$ $\omega_n = \sqrt{\frac{q}{I}}$	171.9 rad/s 1641 RPM	212.8 rad/s 2032 RPM	638 rad/s 6088 RPM
$\omega_n, longitudinal$ TENSION (COMPRESSION)	$k_{eq} = \frac{AE}{L},$ $\omega_n = \sqrt{\frac{k_{eq}}{m}}$	$17 \cdot 10^3$ rad/s 165k RPM	$31 \cdot 10^3$ rad/s 299k RPM	$25 \cdot 10^3$ rad/s 240k RPM
$\omega_n, lateral$ (BENDING)	$k_{eq} = \frac{3EI}{L^3},$ $\omega_n = \sqrt{\frac{k_{eq}}{m}}$	303 rad/s 2897 RPM	551 rad/s 5263 RPM	539 rad/s 5148 RPM

It is important to note that the other modes of vibration have much higher natural frequencies. The fact that torsional vibration was the first mode to impact the structural integrity of the airframe further supports the importance of this investigation. The study of these properties was revisited in later testing phases, as discussed in Task J.

Over the course of three months, the team completed the build of the second iteration of the PAVER quadcopter, incorporating all improvements based on lessons learned from the development of the first vehicle iteration, as shown in Figure 67.

Figure 67. CATIA rendering of PAVER V2

The main difference between PAVER V2 and the first iteration is the structure of the airframe. The V2's arms were carbon fiber tubes with a 0.15" wall thickness and a lay-up orientation optimized for torsional applications. While the weight of each arm is 1.5 times the weight of the previous structure used in V1, it is much stronger in all load cases. The round geometry of the arm tubes required different bonding techniques at the main body and a unique DEP unit mounting solution to adapt the rotorheads to the round tube. Balsa wood strips were glued onto the baseplates to act as a glue dam, and the arms were secured to the baseplates with Hysol 9430 glue mixed with cotton flock. The new DEP unit design also included additional internal supports, increased edge distance, and metal plates bonded to the 3D-printed parts. Figure 68 shows an example of the new DEP unit mounting solution.

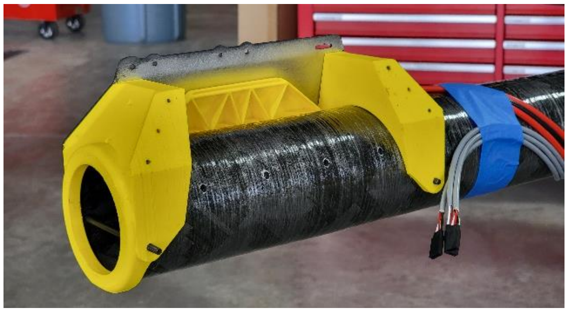

Figure 68. The redesigned structure for V2 DEP units

Aside from the structure, PAVER V2 uses the same avionics and power plants as the original PAVER vehicle. The wiring connections are slightly different due to the implementation of Simulink flight controls - the servos are powered by the PowerBox Competition SR2 power distribution unit and receive PWM signals directly from the servo rail of the Pixhawk Cube. This allows each of the 12 servos to be controlled as its own channel, with two additional channels for throttle control of the ESCs. Both vehicles are shown in Figure 69 below.

Figure 69. PAVER testbed V1 (left) and V2 (right)

The structural improvements made to PAVER V2 contribute to a more rigid airframe than its predecessor does. Arm twist was not observed within the range of operating RPM, but vibration in a different mode was observed, which will be discussed in Task J.

5.7.2 Flight controller

5.7.2.1 *Flight controller hardware*

The Pixhawk Cube Black (Cube) was selected as the flight controller and computer for the vehicle, as shown in Figure 70. This was the controller of choice given its high-performance processor and sensor suite, which includes two barometers and an Inertial Measurement Unit (IMU), consisting of accelerometers, gyroscopes, and a magnetometer, offering vibration isolation and redundancy, thereby improving the accuracy of the controller’s state estimation (Roiati, et al., 2022).

Figure 70. Pixhawk Cube Black

5.7.2.2 Flight controller firmware

When deciding which firmware to integrate on the Cube, there were two options: ArduPilot and PX4 Autopilot. During initial flight tests, the Cube was running the ArduPilot firmware in the HeliQuad flight mode. The HeliQuad flight mode works in a manner similar to an RPM controlled quadrotor, but rather than increasing or decreasing an individual motor’s RPM, the collective pitch of that rotor is increased or decreased while the RPM is held constant. The goal was to transition to a flight controller software that could run custom flight control algorithms designed in Simulink. Both firmware options were thoroughly investigated to determine which would provide the most flexibility in terms of codebase customization and smooth integration with MATLAB and Simulink (Roiati, et al., 2022).

The PX4 Autopilot was selected because it was found to support robust integration with Simulink/MATLAB. Simulink's *UAV Toolbox Support Package for PX4 Autopilots* enabled a seamless interface, allowing the use and development of custom flight-control algorithm models. The *Embedded Coder* function in Simulink converts these Simulink models into C++ code, which is then integrated with the PX4 Autopilot firmware, enabling the code to connect directly with the Cube's onboard sensors and systems (Roiati, et al., 2022).

FlightGear, described in section 5.8.1, was utilized to visualize simulations and tests of the flight control algorithms in virtual 3D environments. The integration of FlightGear and PX4 Autopilot firmware with Simulink facilitated software simulations and tests, with Simulink serving as the central component of the flight-control development workflow.

5.7.2.3 Flight control algorithms

After validating the rotors, the vehicle controller was designed. Because the total number of control effectors on the vehicle is greater than the number of axes to control, the controls must be allocated, or mixed together to achieve motion about these axes. The PAVER prototype, like any other standard RC helicopter, is controlled by the following inputs:

1. Vertical acceleration (corresponding to the collective)
2. Pitch control moment (corresponding to the longitudinal cyclic)
3. Roll control moment (corresponding to the lateral cyclic)
4. Heading control (corresponding to the tail rotor collective)

A custom motor mixing algorithm (MMA) was designed for the propulsion system of the vehicle, enabling both collective, pitch, and roll responses to pilot commands from the swashplates, as shown in Figure 71. The pre-flight setup involved leveling and calibrating the swashplate and customizing its input PWM response to match the required angular deflection of the propulsion system's blades (Roiati, et al., 2022). The mixing configuration of the block is dependent on the active flight modes of the vehicle.

The flight modes that have been tested are shown in

Table 6:

1. Fixed Pitch (FP): Differential RPM for Roll, Pitch and Yaw
2. Variable Pitch 1 (VP1): Collective Control for Roll, Pitch and Yaw
3. Variable Pitch 2 (VP2): Same as VP1, except Yaw is Cyclic Controlled

Table 6. Flight modes

#	Flight Mode	Control Method			
		Throttle	**Roll**	**Pitch**	**Yaw**
1.	FP	RPM	RPM	RPM	RPM
2.	VP1	Collective	Collective	Collective	Collective
3.	VP2	Collective	Collective	Collective	Cyclic

This mixing model was improved to include a PID controller as a feedback loop to aid in the stabilization of the aircraft's attitude and heading during operation (Roiati, et al., 2022). The PID control gain values were determined using the mathematical model implemented in FlightGear.

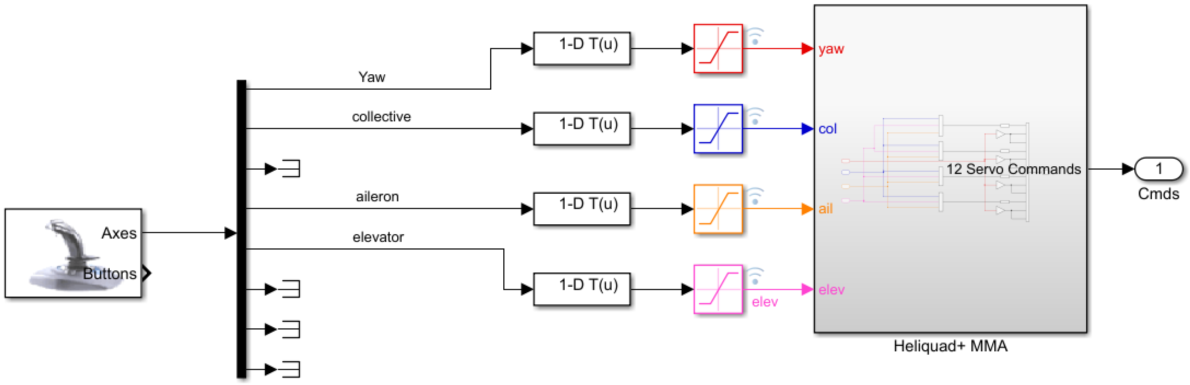

Figure 71. Motor mixing algorithm overview

5.7.3 Flight modes

5.7.3.1 Fixed pitch (FP)

This type of controller operates by altering the rotor speed. Two rotors spin clockwise and two counterclockwise, each delivering thrust equivalent to one-fourth of thrust required to hover under ideal conditions. The schematic of this mode is shown in Figure 72.

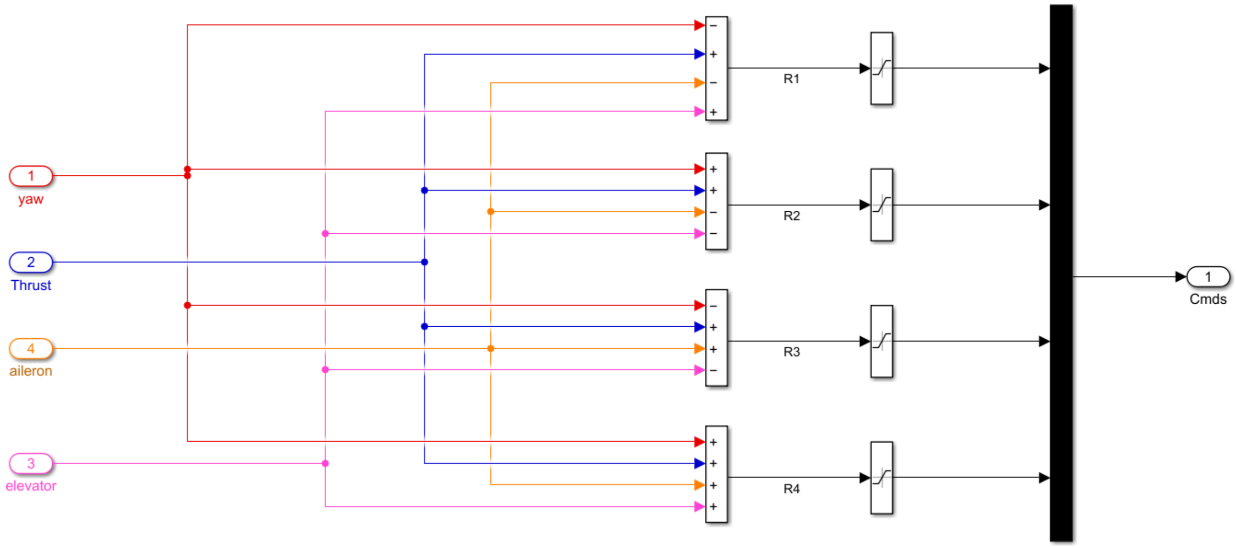

Figure 72. Fixed pitch motor mixing algorithm

In this mode, yaw control is achieved by adjusting the rotation rate of the two pairs of rotors, such as increasing the speed of the clockwise rotors while decreasing the speed of the counterclockwise rotating rotors, or vice versa. The overall thrust is maintained constant during this process.

5.7.3.2 Variable pitch 1 (VP1)

The VP1 MMA controller model, as shown in Figure 73, enables PAVER to be controlled in a collective-only mode while keeping the RPM governed. The thrust is produced by altering the collective blade angle of all the rotors together, which in turn increases the net thrust produced. Utilizing the differential collective pitch allows the vehicle to roll, pitch, and yaw accordingly.

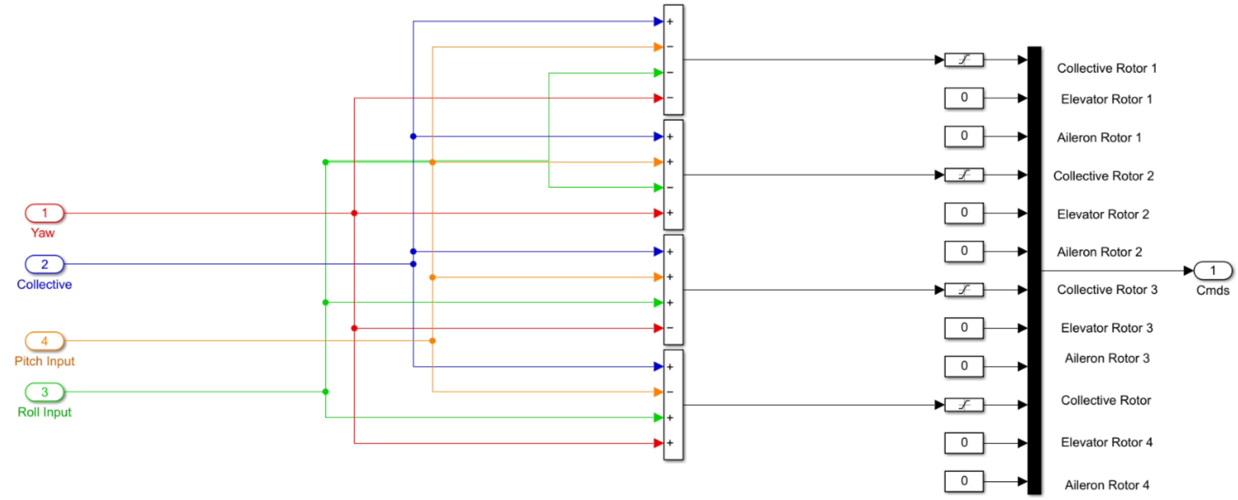

Figure 73. VP1 motor mixing algorithm

5.7.3.3 Variable pitch 2 (VP2)

The VP1 model allows PAVER to perform the essential maneuvers required for flight; however, it fails to maintain the necessary performance for the required yaw rate. As a result, another MMA, called the VP2, was designed, as shown in Figure 74. This MMA allows the rotor disc to rotate cyclically about the hub, enabling yaw control through thrust vectoring.

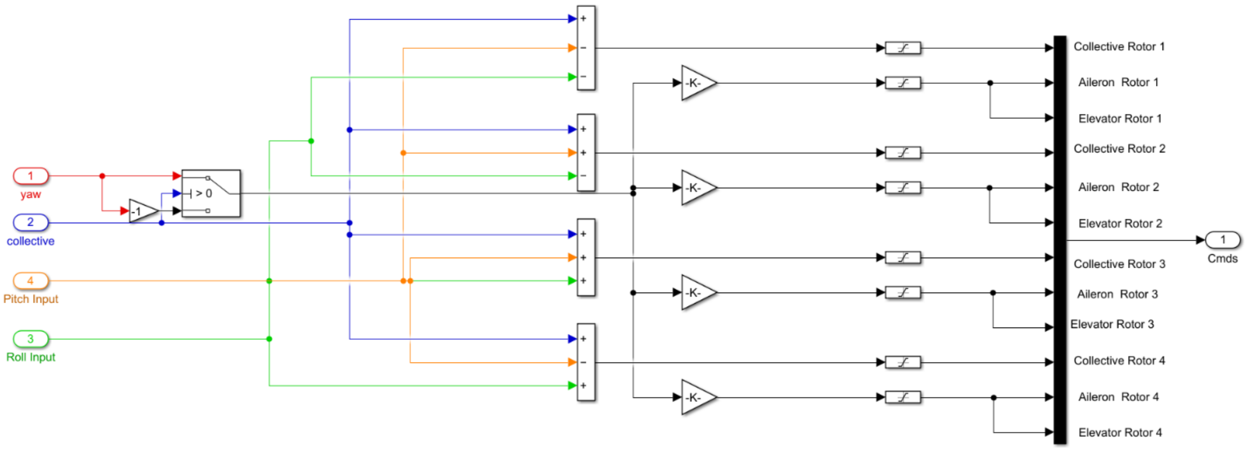

Figure 74. VP2 motor mixing algorithm

A feedback control system using PID controllers was employed in the control algorithm as a starting point, with the objective of later transitioning to a more advanced and complex controller as required.

The input to the PID controller is an error signal (difference between actual and desired value), which is multiplied by PID gains to acquire the controls which are further processed under the MMA to convert to the vehicle's control. In total, there are three PIDs – one for each of the vehicle's moments – roll, pitch, and yaw. Each controller was fine-tuned considering parameters like rise time, settling time, and overshoot. Once tuned, these PIDs were tested in a simulation environment where FlightGear was used to visualize the model. Although the PID controller may generate appropriate control input, the simulation may not reflect the behavior in a real-world setting. However, this established a baseline from which the controller could be fine-tuned. Three types of controllers were designed, namely, a rate controller, attitude controller, and cascaded feedforward controller. The cascaded feedforward controller has a rate command / attitude hold response type and makes use of aspects of both rate and attitude controllers.

5.7.3.4 Rate controller

Figure 75 shows a rate controller where the input commands are from an RC transmitter. The joysticks control the vehicle's collective as well as its roll, pitch, and yaw rates. When the joystick deflection is released, the vehicle attempts to maintain zero angular rate, and does not automatically level. This gives the operator control over the vehicle and enhances its maneuverability. The Euler angles are not constrained in any way, which would allow the vehicle to fly upside down. Error signals created from a difference between the commanded rate and the vehicle's actual rate are fed into the PIDs to obtain the desired response. As the commanded roll, pitch, and yaw rate change with pilot input, the controllers will attempt to track these inputs accurately.

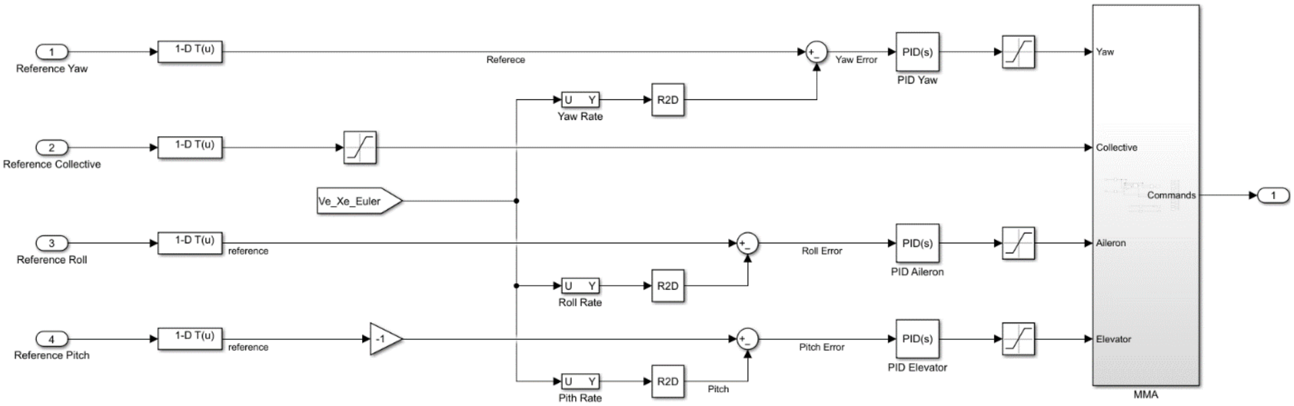

Figure 75. Example rate controller

5.7.3.5 Attitude controller

The structure of an attitude controller is very similar to that of the rate controller except that the error signals are created from differences in vehicle attitude rather than angular rates. Reference attitudes can come from either pilot stick position or from the attitude the vehicle has when the stick is released. In the case of pitch or roll commands, stick deflection equals a commanded pitch or roll angle. For yaw, stick deflection still equals a rate command as discussed in the previous section. However, when the stick is released, the controller holds the existing heading.

5.7.3.6 Cascaded feedforward control

The cascaded feedforward controller, shown in Figure 76, is the final version of the controller used in PAVER for all control strategies. It combines aspects of both rate and attitude controllers, with the inner loop tracking rate commands and the outer loop tracking angle commands. This controller also has a feedforward loop that reduces the error between the reference and actual command more quickly, improving the efficiency of command tracking.

The feedforward loop allows the rate input from the pilot to be instantly commanded into the rate controller (inner loop).

The controller used in this system has four input signals: three angular rates with saturation limits, and a collective command. This controller functions similarly to a rate controller, but it can maintain the latest attitude when the stick deflection is returned to center. In addition, a stable level switch has been implemented to bring the vehicle back to a level orientation from any angle.

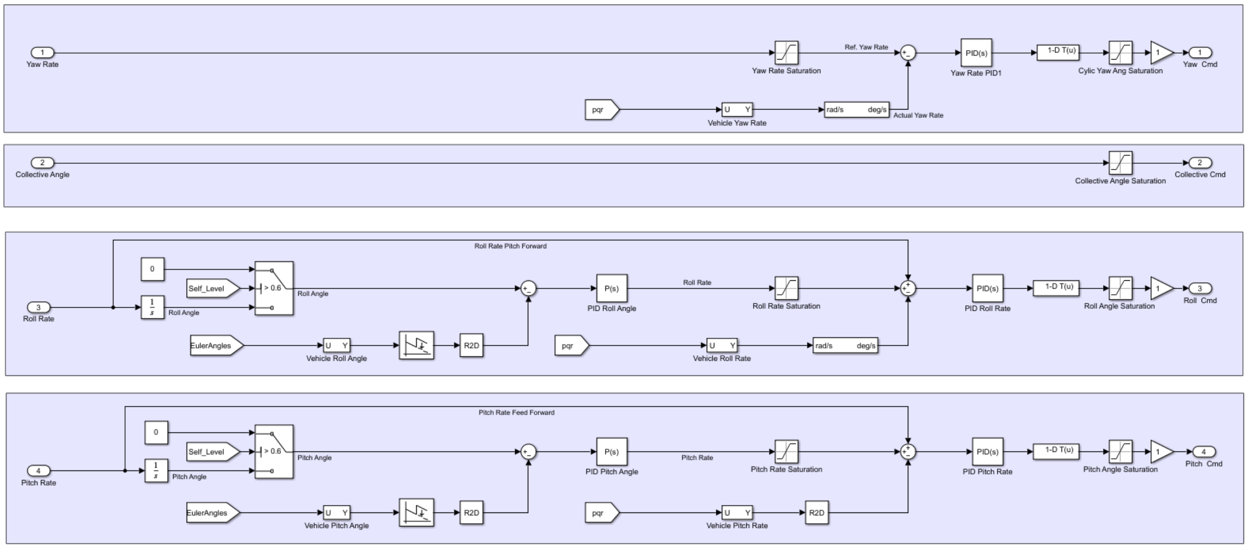

Figure 76. Cascaded feedforward controller

The block diagram in Figure 77 illustrates the process of designing, implementing, and testing the flight control algorithms for the vehicle. The mathematical models of the vehicle were analyzed to develop control laws that incorporate PID controllers. The flight control algorithms were iteratively tested and refined using FlightGear to tune the PID gains of the controller. Once the controller had been verified, it was uploaded to the vehicle and subjected to a series of flight tests to evaluate its stability and response to control input. Data was collected during these tests to provide insights into the performance of the controller.

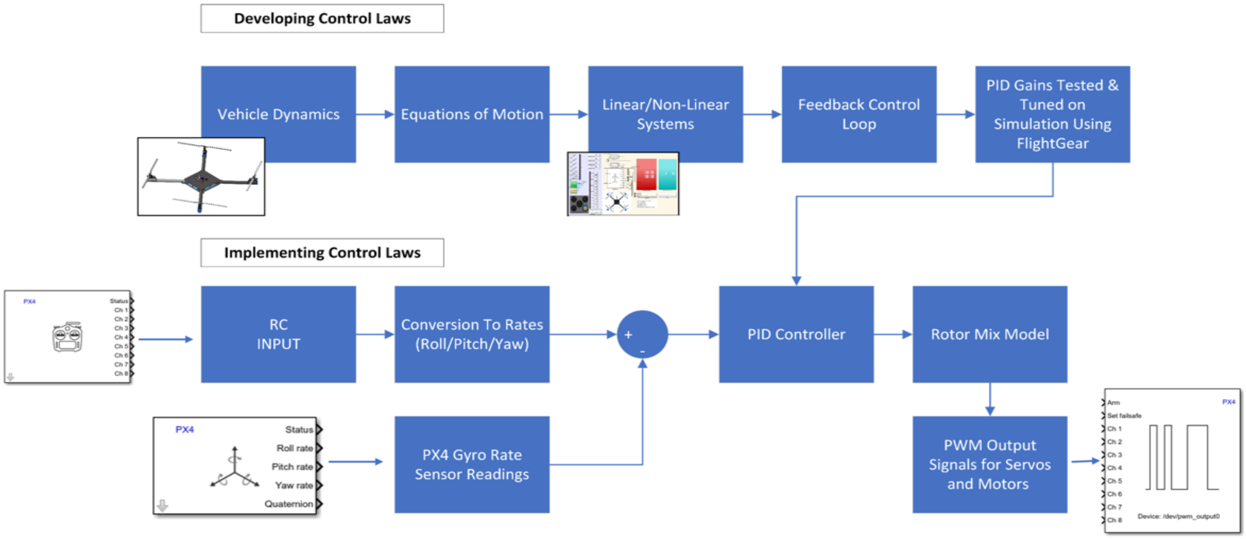

Figure 77. Control law development and implementation

Figure 78 and Figure 79 show the VP1 and VP2 flight mode controllers for PAVER V2 respectively. Both are based on the cascaded feedforward controller. The pilot can switch between predefined RPM presets, simulate a rotor failure, and command the drone to stabilize and maintain level attitude conditions. This controller also includes data logging.

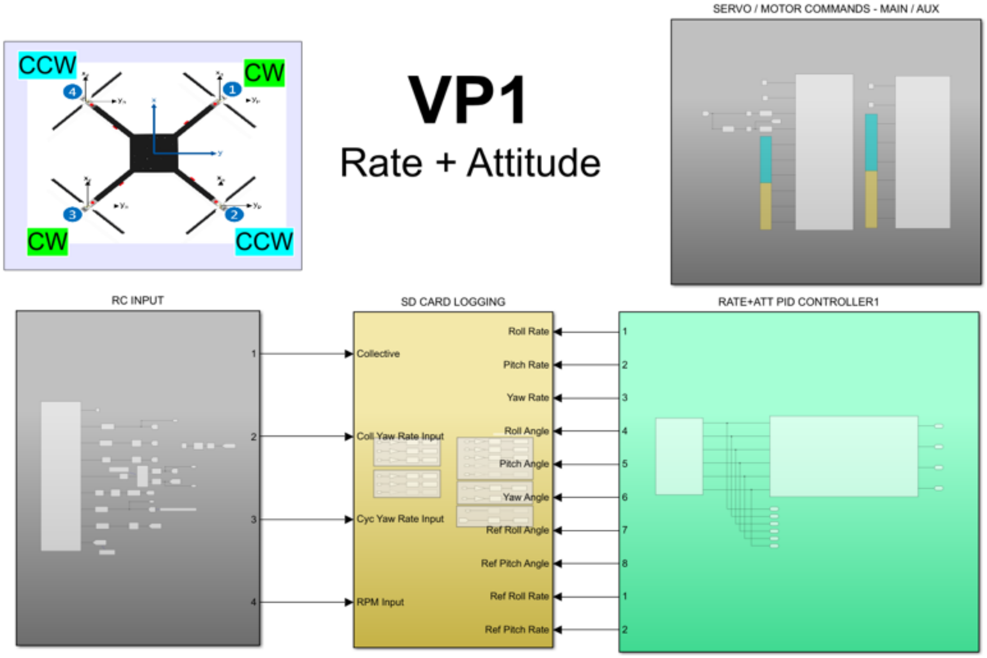

Figure 78. VP1 flight controller

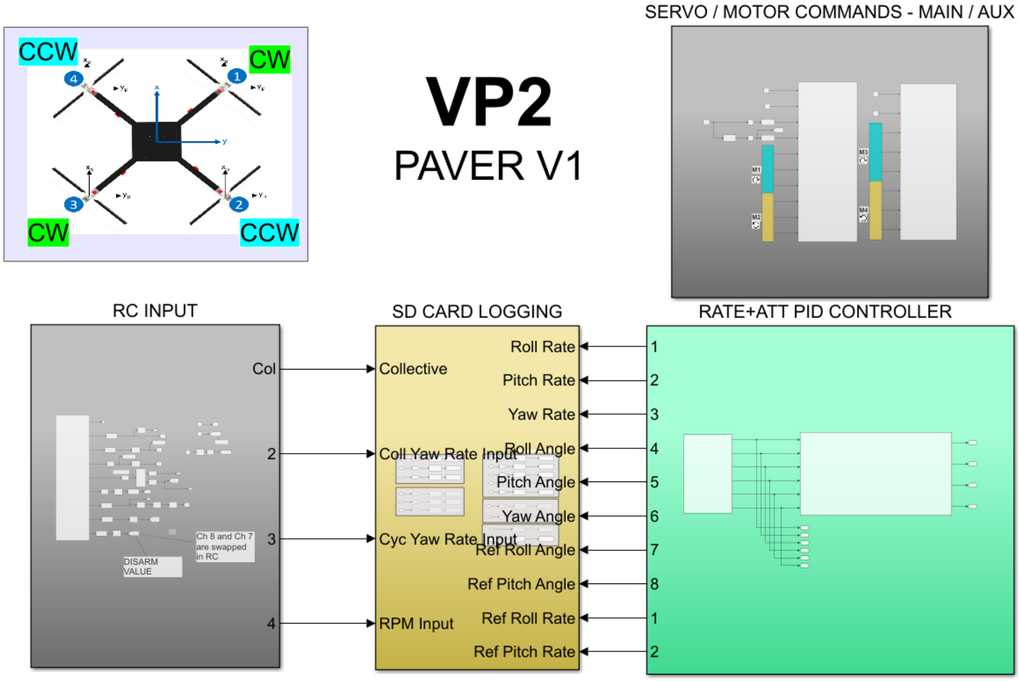

Figure 79. VP2 flight controller

5.8 Task H: Simulate DEP unit loss of thrust/moment

5.8.1 FlightGear

The use of the FlightGear simulator played a crucial role in the development and testing of the flight control system for the PAVER vehicle. In addition to the previously evaluated and validated RCAS and Simulink mathematical models, the simulator provided a virtual test environment where the control algorithms and controllers could be tested and adjusted. The 3D environment of the simulator allowed the team to interact with the vehicle and better understand its behavior control response. One of the key objectives of the tests was to study the closed-loop vehicle dynamics with a failed rotor.

FlightGear is a free and open-source flight simulator that offers several advantages over commercial alternatives. It allows users to modify and enhance the simulator experience by using custom aircraft models and flight control systems, and it includes dedicated blocks in the *Simulink Aerospace Blockset* for data transmission via User Datagram Protocol (UDP) network packets. These features were utilized to optimize the simulation experience while testing the control algorithms and controllers. To facilitate data transmission and visualization, the FlightGear simulator includes two dedicated blocks in the *Simulink Aerospace Blockset*: the *Preconfigured 6 DoF Animation Block* and the *Generate Run Script Block*. The *6DoF Animation Block* allows the user to drive position and attitude values to FlightGear's simulated vehicle using double-precision values for longitude (l), latitude (μ), altitude (h), roll (ϕ), pitch (θ), and yaw (ψ), respectively. The *Generate Run Script* block generates a customized FlightGear run script on the current platform.

A CAD model of PAVER was converted to an .ac file. The model was then imported into FlightGear, as shown in Figure 80, allowing the utilization of its features for development of the control algorithms and controllers.

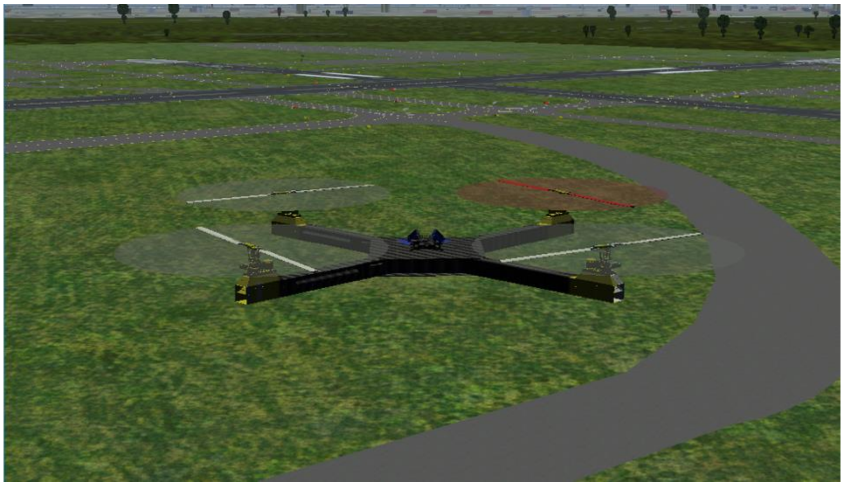

Figure 80. PAVER CAD model imported to FlightGear

All three flight modes (FP, VP1, VP2) of the PAVER vehicle were tested in the FlightGear simulation, along with the rate, attitude, and cascaded feedforward controllers that were incorporated within each flight mode. The primary aim of using FlightGear was to visually demonstrate the capabilities of the vehicle and facilitate easier interaction with the theoretical model. It also provided an environment where controller gains could be modified and tested, thereby facilitating the identification of optimal control settings. The three flight modes and controllers were repeatedly improved to achieve better tuned PIDs and overall vehicle control. Figure 81, Figure 82, and Figure 83 show PAVER performing yaw, pitch, and roll maneuvers in FlightGear.

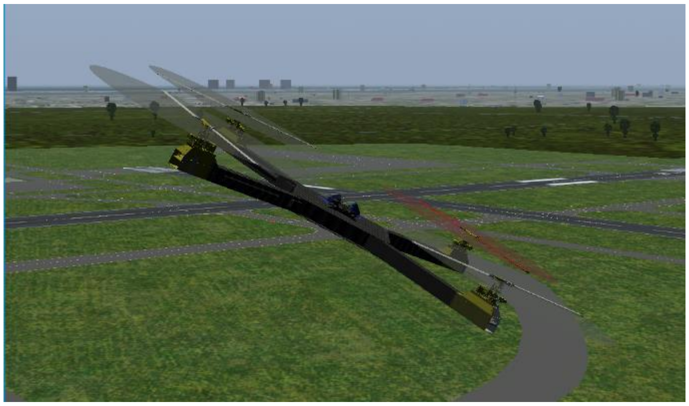

Figure 81. PAVER performing positive roll in FlightGear

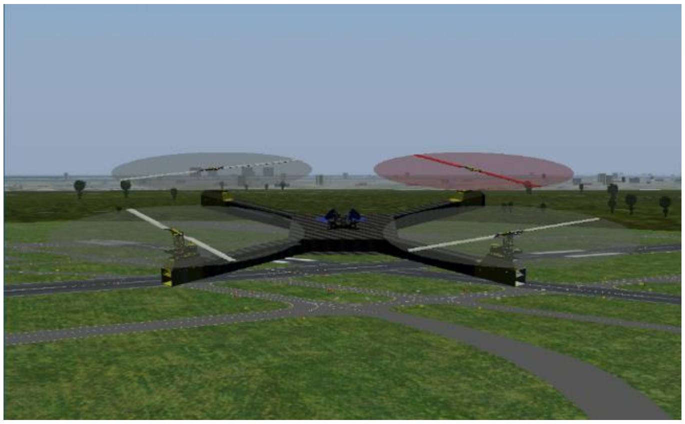

Figure 82. PAVER performing positive pitch in FlightGear

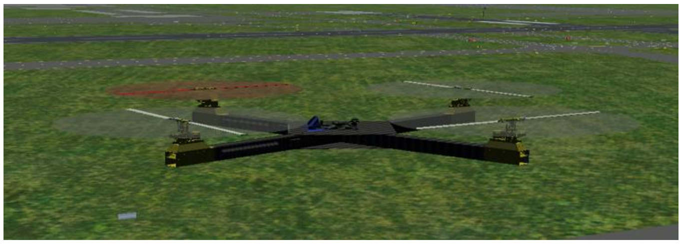

Figure 83. PAVER performing negative yaw in FlightGear

Figure 84 shows how the flight control algorithms can be implemented into both the flight controller as well as FlightGear.

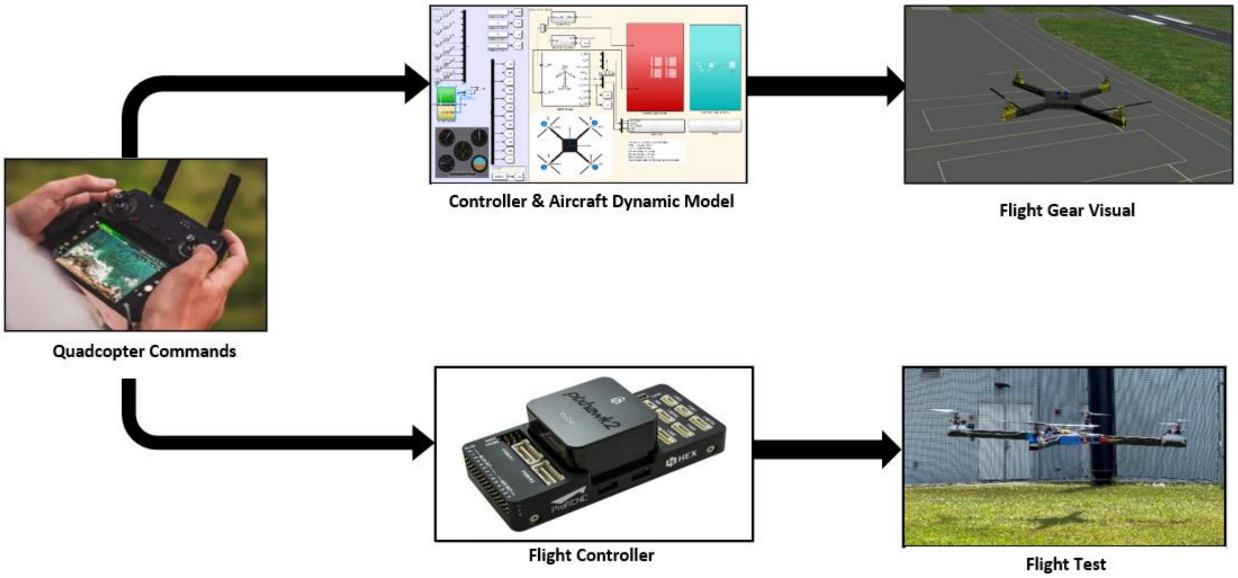

Figure 84. Control implementation from Simulink to Pixhawk Cube and FlightGear

5.8.2 Flight modes response under nominal flight conditions

5.8.2.1 Fixed pitch (FP) under nominal conditions

The Fixed Pitch controller enables PAVER to be controlled in a constant blade pitch mode, also known as constant collective mode. In this mode, the thrust is produced by adjusting the RPM of all four rotors together, while differential RPM allows the vehicle to roll, pitch, and yaw.

In simulation, the collective blade pitch was held at 7°, which was close to the trim condition of hover around 6.5° at 1500 RPM. The RPM range was set from 300 to 1530 to match the actual flight configuration. Higher RPM ranges were avoided out of an abundance of caution, following the previous high-vibration failures in flight-testing.

Figure 85 shows the nominal behavior of the quadrotor rate response for the Fixed Pitch controller. A time delay of 80 milliseconds was included to simulate the actual spool-up characteristics. The simulation tracks the reference yaw-rate command with a settling time of 3.5 seconds with roll and pitch rate settling times of 0.7 seconds when performing step response of the commanded rates.

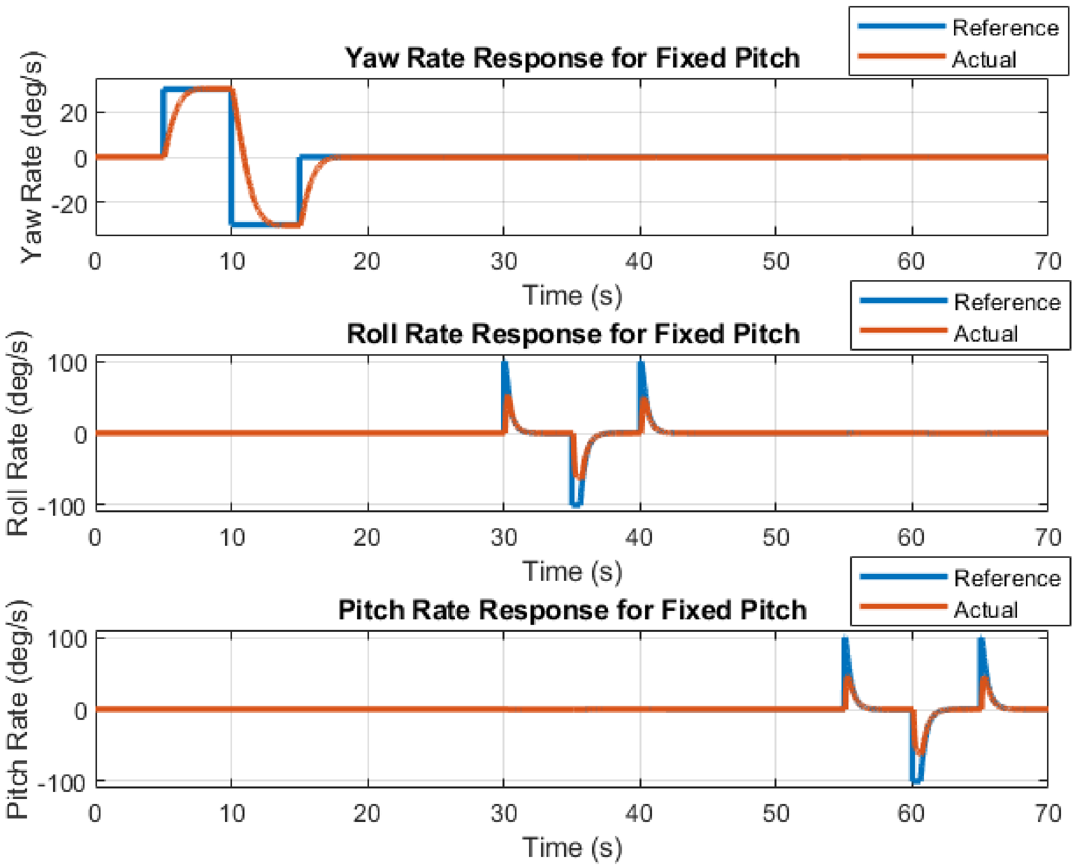

Figure 85. Rate response of PAVER in FP flight mode pre-failure

5.8.2.2 Variable pitch-1 (VP1) under nominal conditions

The VP1 controller enables the PAVER vehicle to be controlled in a collective-only mode while maintaining a constant RPM. In this mode, the thrust is produced by adjusting the collective blade angle of all the rotors together, which increases the net thrust. Differential collective pitch is used to allow the vehicle to roll, pitch, and yaw.

Similar step response commands were tested using this flight mode, and the rate response is shown in Figure 86. The simulation was performed at a constant RPM of 1500. The simulation tracks the reference yaw rate with a settling time of 1.6 seconds. The roll and pitch rates have a settling time of approximately 0.4 seconds when performing step response of the rates.

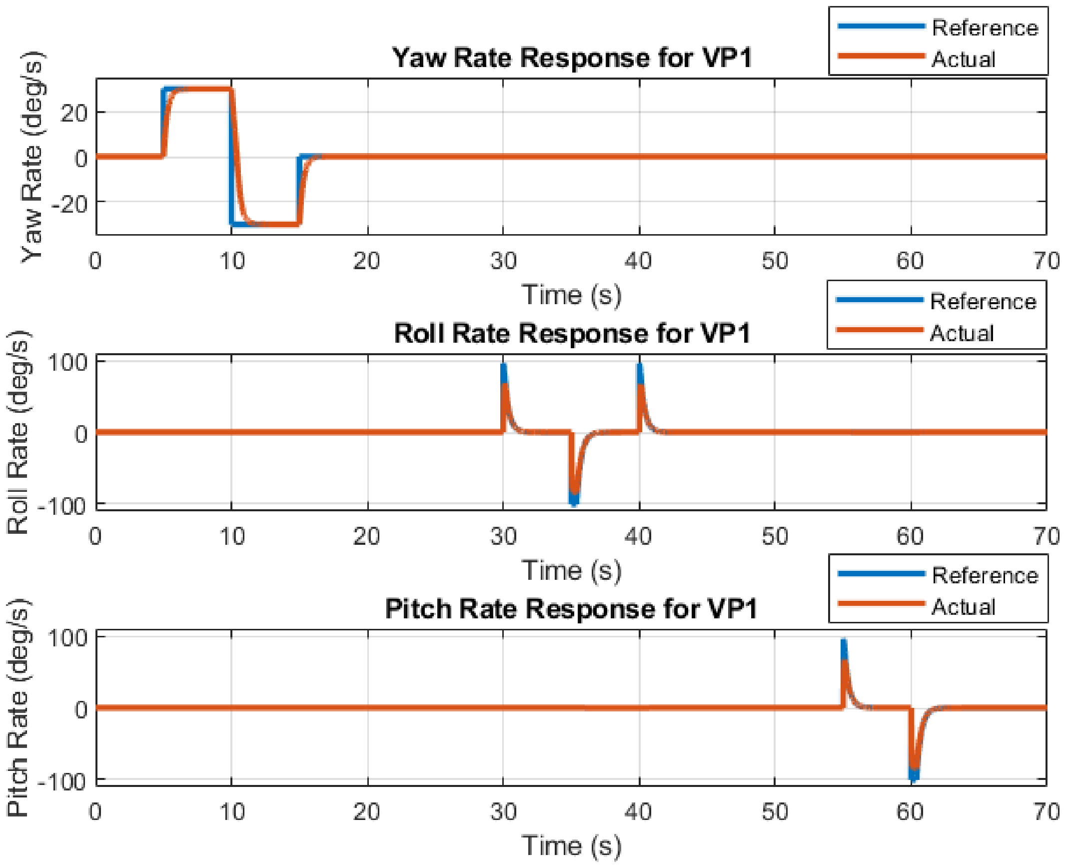

Figure 86. Rate response of PAVER in VP1 flight mode pre-failure

5.8.2.3 Variable pitch-2 (VP2) under nominal conditions

The VP2 model enables the PAVER vehicle to perform the essential maneuvers required for flight, similar to the VP1 model. However, the VP1 model may not provide sufficient yaw performance in certain situations, so the VP2 strategy was implemented to improve yaw performance.

The VP2 controller enables the PAVER vehicle to be controlled in a collective-only mode for heave, pitch, and roll, while using cyclic for yaw. In this mode, the thrust is also produced by adjusting the collective blade angle of all the rotors together. Differential collective pitch is used to allow the vehicle to pitch and roll, while the cyclic of the DEP units are slaved together to create a yawing moment about the CG.

The simulation was performed at a constant RPM of 1500. When performing step response of the rates, the simulation tracks the reference yaw rate with a settling time of 1.2 seconds. The roll and pitch rate settling time is the same as the VP1 model, as shown in Figure 87. The key difference between each flight mode is the yaw rate response to the inputs.

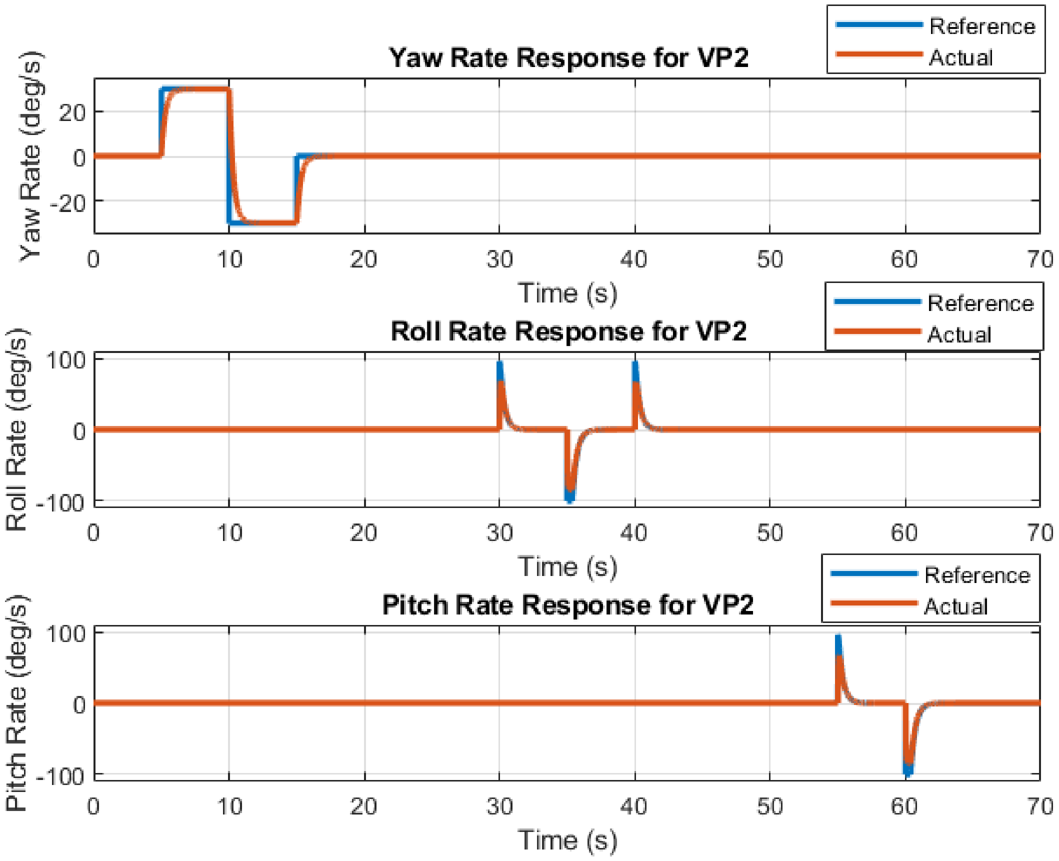

Figure 87. Rate response of PAVER in VP2 flight mode pre-failure

5.8.3 Flight modes response under rotor failure conditions

Figure 88 shows a simulated failed rotor case. The failed rotor is set to gradually spool down to 0 RPM starting at t = 10 seconds while the other rotors maintain the governed RPM. The RPM response is illustrated in Figure 89.

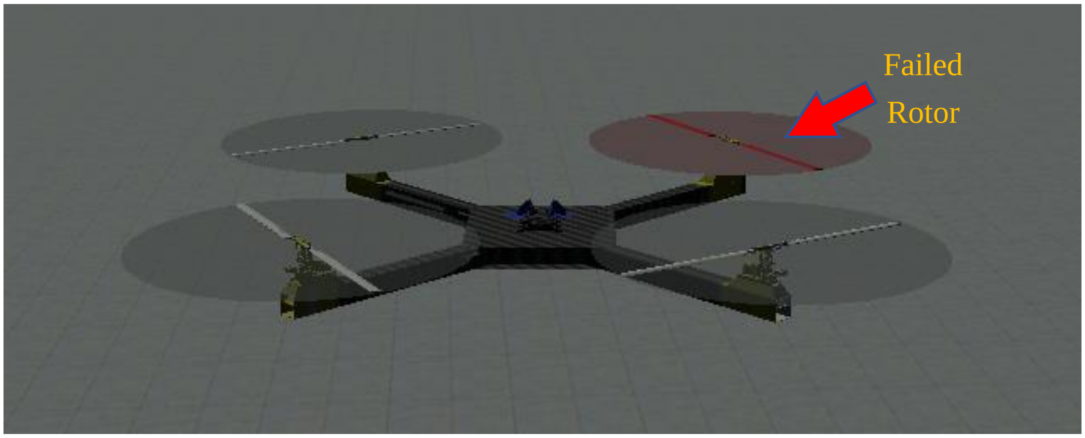

Figure 88. PAVER in FlightGear with failed unit

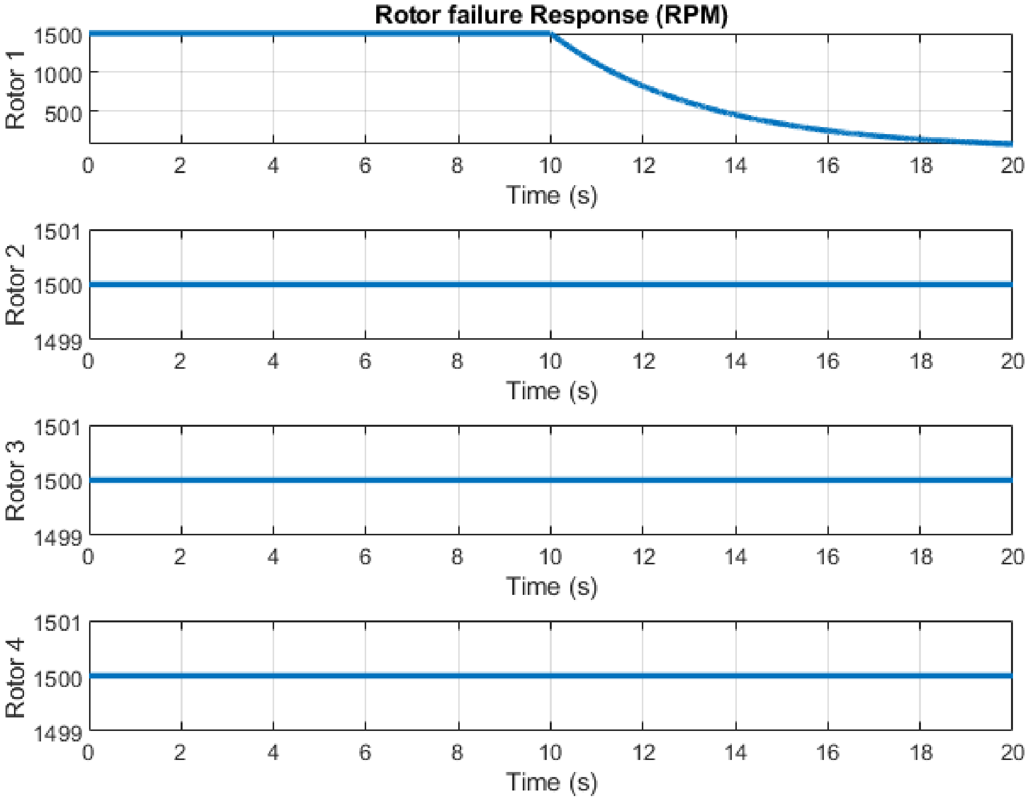

Figure 89. Rotor RPM in rotor failure scenario

5.8.3.1 Rate response under rotor failure for fixed pitch (FP)

Figure 90 shows the PAVER vehicle's rate responses to failure while in the FP flight mode. After rotor failure at 10 seconds, the vehicle continues to spiral uncontrollably towards the longitudinal axis (pitch) and in yaw, as shown in the yaw and pitch rate responses. The altitude of the vehicle drops rapidly and crashes within 8 seconds after the failure, shown in Figure 91. The vehicle is unstable and uncontrollable after rotor failure in fixed-pitch mode.

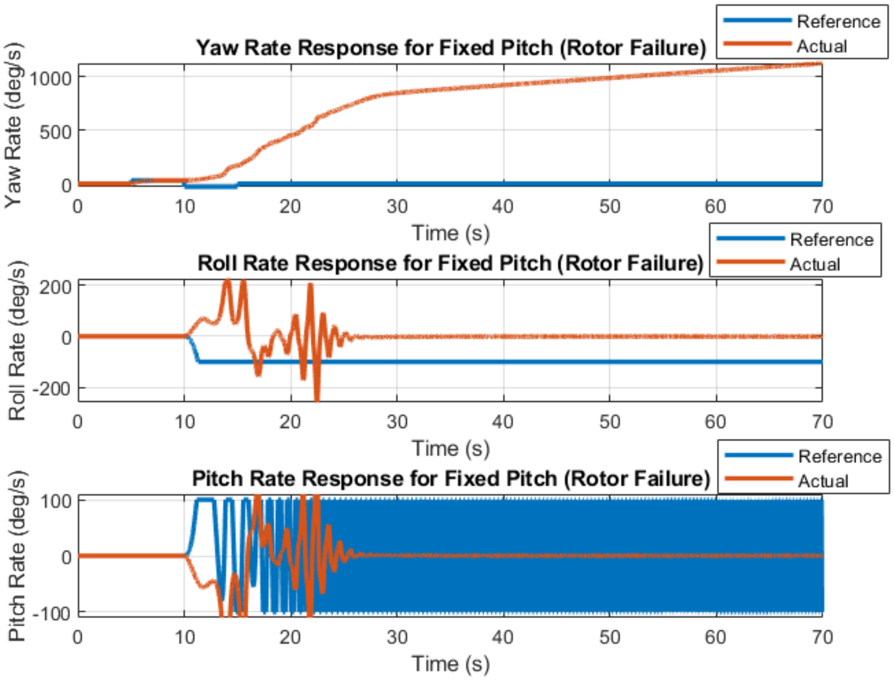

Figure 90. Rate response of PAVER after failure in FP flight mode

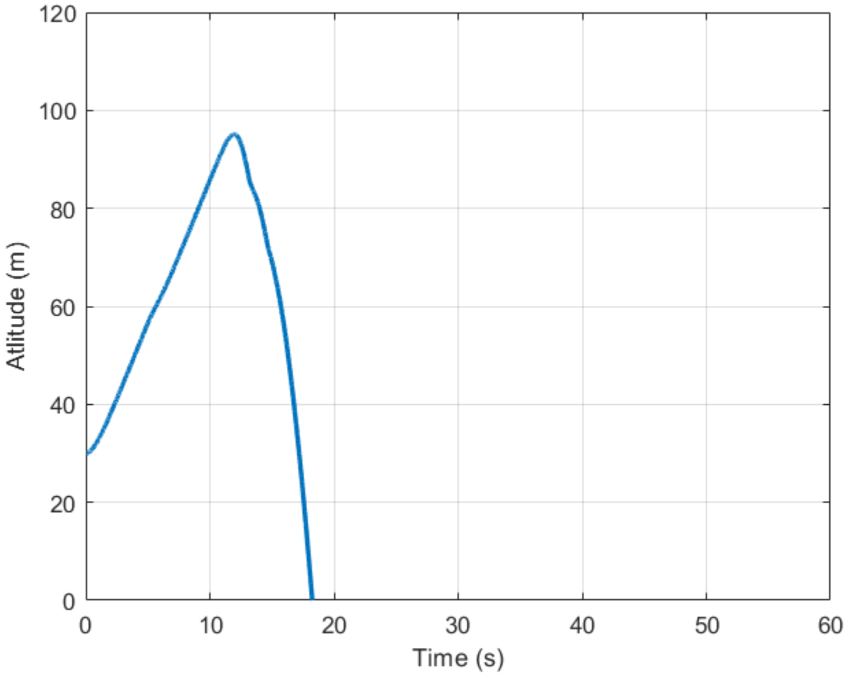

Figure 91. Altitude of PAVER after failure in FP flight mode

5.8.3.2 Rate response under rotor failure for variable pitch-1 (VP1)

Figure 92 shows the PAVER vehicle's rate responses after a failure in the VP1 flight mode. After a rotor failure at 10 seconds, the vehicle begins to yaw uncontrollably, as shown in yaw pitch and rate response. The controller attempts to follow the desired pitch and roll rates at an offset, as shown in the roll and pitch rate responses. The altitude of the vehicle drops rapidly and crashes within 12 seconds after the failure, shown in Figure 93.

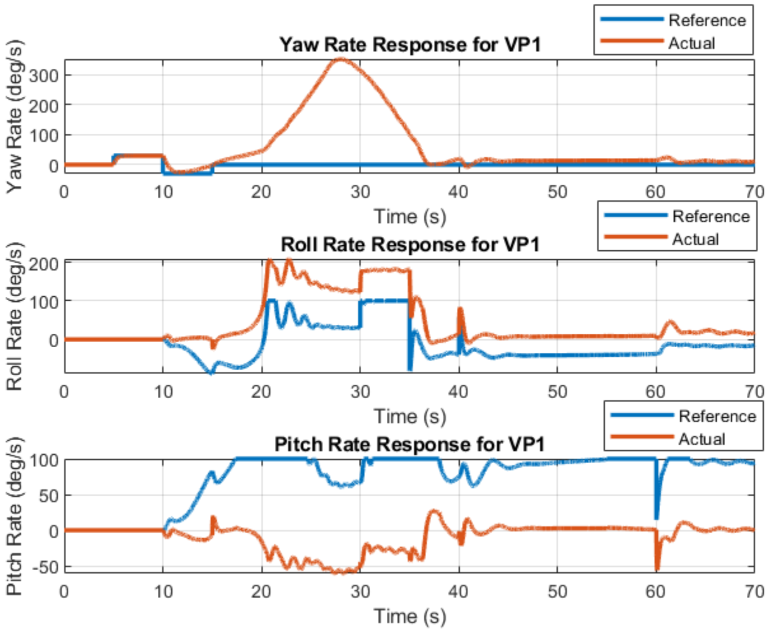

Figure 92. Rate response of PAVER after failure in VP1 flight mode

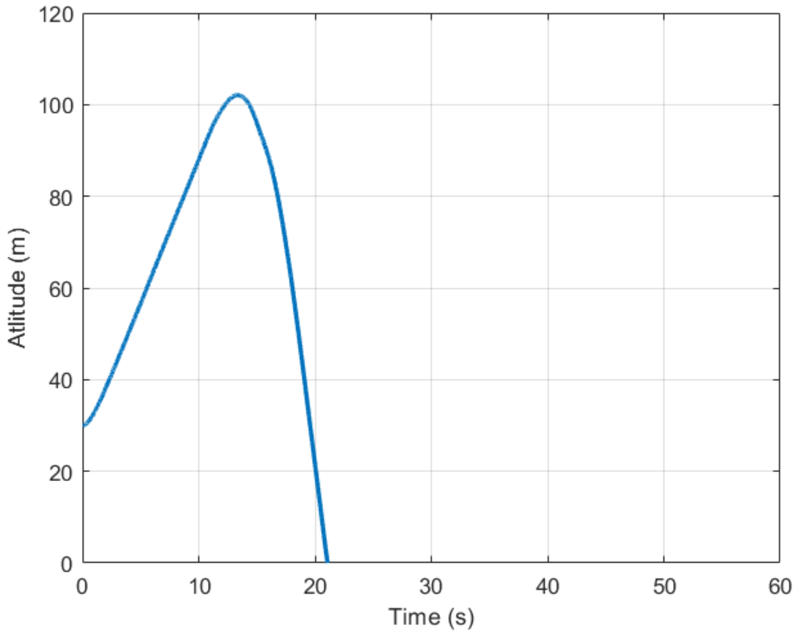

Figure 93. Altitude of PAVER after failure in VP1 flight mode

5.8.3.3 Rate response under rotor failure for variable pitch-2 (VP2)

Figure 94 shows the PAVER vehicle's rate responses after a failure in the VP2 flight mode. A rotor failure is induced at T=10 seconds. The vehicle is not completely unstable, and attempts to maintain its attitude and follow the commanded rates, as shown in the yaw, roll and pitch rate responses. Figure 95 shows the altitude plot of the vehicle, which shows that the vehicle is able to remain in the air after the failure.

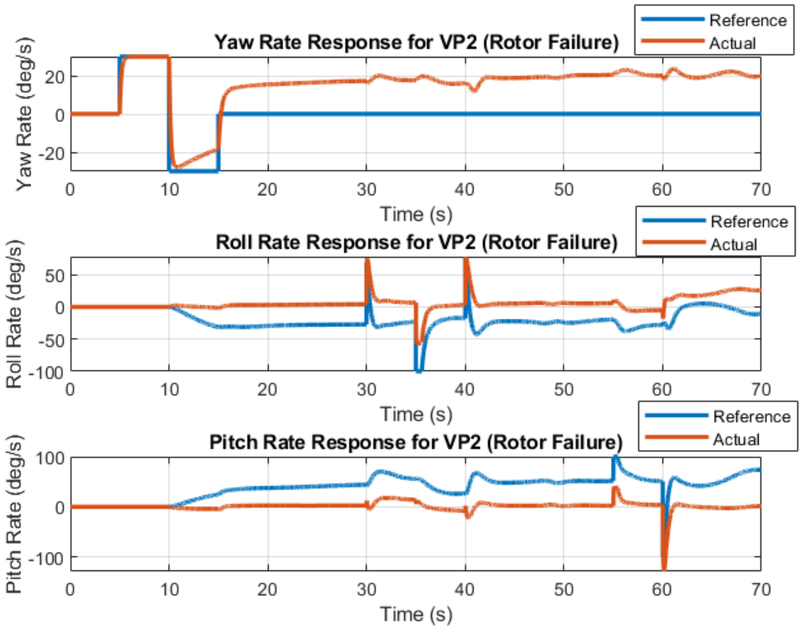

Figure 94. Rate response for VP2 after failure

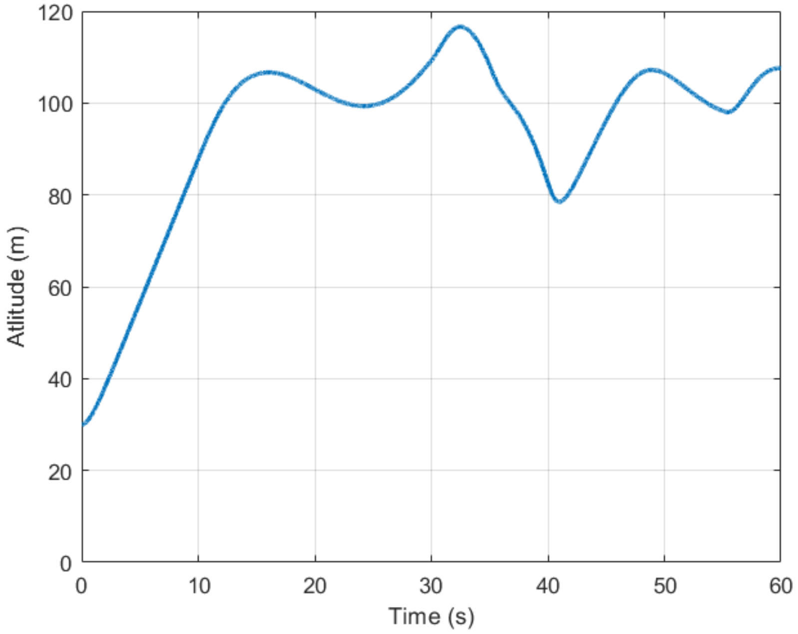

Figure 95. Altitude of PAVER after failure for VP2

5.8.3.4 Concluding remarks on flight mode response under failure conditions

The results of the failure scenarios show that the FP and VP1 flight modes perform as expected based on the theoretical analysis, as both have a fixed thrust direction. When a failure occurs, the vehicle becomes unstable, particularly in yaw, as it is unable to maintain yaw with a failed rotor.

The vehicle can track the reference commands when a failure is simulated in the VP2 flight mode at a constant RPM of 1500. However, due to insufficient control power at 1500 RPM, the tracking error gradually increases over time and a controlled crash scenario can be simulated with pilot commands. During flight-testing, it was observed that the vehicle can maintain a stable attitude with a rotor failure at 1650 RPM but loses control power to maintain attitude at 1500 RPM.

Figure 96 shows the stages of rotor failure in the FlightGear simulation for the FP mode. The right front rotor, indicated in red, fails at t = 10 seconds. In stage 1 the vehicle is trimmed to hover, with all rotors functioning at a constant RPM of 1500. The failure is then induced in the front right rotor resulting in immediate loss of thrust on the DEP unit. This causes the vehicle to tilt towards the right front rotor as shown in stage 2. This is followed by loss in yaw control due to torque imbalance, which causes loss of control, as seen in stage 3.

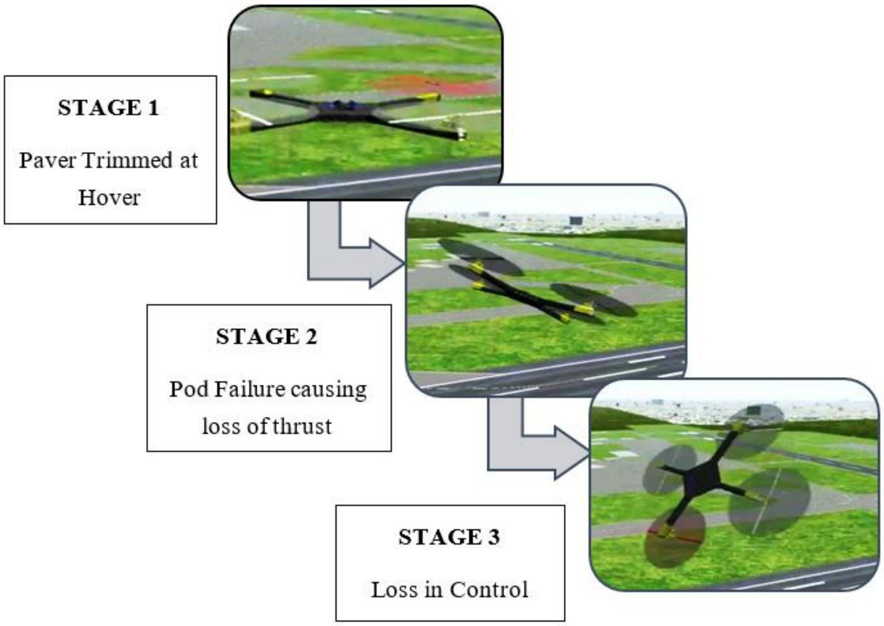

Figure 96. Phases of rotor failure (Fixed-Pitch)

5.8.4 Lessons learned: DEP unit failure simulation

The analysis of the failure scenarios has provided several key insights. The simulations were performed under ideal conditions, i.e., no wind disturbance was considered. Therefore, the actual responses after failure may differ in real-world conditions. Additionally, the simulations did not take into account the vibrations of the rotor system, which could affect the actual responses of the vehicle as observed during actual flight-testing. Another factor to consider is that in the simulations, all four rotors rotate at the same RPM, while in the actual vehicle, the RPM varies slightly between different DEP units. These factors should be taken into account in future simulations and flight-testing to understand the performance of the vehicle in various failure scenarios.

5.9 Task I: Develop quadrotor vehicle test matrix to validate simulation results

The results from the virtual experiments performed in FlightGear were used to create a physical experiment test matrix for vehicle tests (as described in section 5.10). These tests were conducted in part to verify and validate the simulation results (as described in section 5.11), both in nominal and single DEP unit loss conditions (as described in section 5.8). The data from these tests was analyzed to compare the vehicle's controllability in both of these conditions. The testing described in the matrix was planned on all three DEP unit control strategies (FP, VP1, and VP2). However, given that the simulation results showed that the FP and VP1 control strategies would not be able to maintain controllability after DEP unit loss, it was decided to prioritize testing the VP2 control strategy over the other strategies.

The test matrix shown in Table 7 outlines a list of maneuvers for the pilot to command and follow during vehicle tests. To ensure safety, these maneuvers were performed manually by the pilot rather than being programmed into the flight software to be carried out autonomously in an untethered environment. As seen in the matrix in Table 7, the tests were conducted in three environments – attitude test stand (ATS) as shown in Figure 97, tethered flights as shown in Figure 98, and untethered flights. Each test would start with nominal conditions by following rounds 1 and 2 on the test matrix. The same procedure was then followed, but under a DEP rotor failure condition. The ATS tests were conducted with the vehicle's arms tethered to restrict the angular motion of the vehicle. The pilot’s feedback on handling qualities were recorded after each round, and the flight software parameters such as the PID gains and angular rate limits were tuned accordingly.

Figure 97. Attitude test stand with vehicle’s arms tethered

Figure 98. Tethered flight of PAVER V2

Table 7. PAVER test matrix

Test Environment	**Pilot Commands**			
	Round 1		**Round 2**	
	Maneuver	**Magnitude**	**Maneuver**	**Magnitude**
Attitude Test Stand (ATS)	**Roll Angle**	±20°	**Roll Angle**	**±30°**
	Pitch Angle	±20°	**Pitch Angle**	**±30°**
	Yaw Angle	±20°	**Yaw Angle**	**±90°**
	Purpose		**Purpose**	
	Apply PID gains from Simulation on the vehicle, and check vehicle response. Tune the PIDs as required.		Record pilot feedback on handling qualities and response time to attitude commands.	
Untethered flight	**Hover**	4 $ft.$	**Hover**	10 $ft.$
	Roll Doublet	0°	**Roll Doublet**	±35°
	Pitch Doublet	0°	**Pitch Doublet**	±35°
	Yaw Doublet	±20°	**Yaw Doublet**	±35°
	Purpose		**Purpose**	
	Apply PID gains acquired from Simulation and ATS. Check vehicle response. Tune the PIDs as required.		Record pilot feedback on handling qualities and response time to translational commands.	

5.10 Task J: Perform quadrotor vehicle tests

To study the vehicle under nominal and failed rotor conditions, a series of flight tests were conducted. These tests were performed in accordance with the test matrix seen in Table 7. Most of them entailed testing different control laws and architectures, tuning PID gains and performing hardware-simulation validation. These flight tests were specific to the flight mode (FP, VP1, or VP2) and flying conditions (nominal, partial failure & full failure). The workflow followed included activities described in the following sections.

5.10.1 Dynamic model development

The development of the dynamic model is an important step in the workflow as it serves as a building block of the hardware-simulation validation. The development of the simulation model was discussed in detail in Section 5.3. The process involved developing and tuning the dynamic model to predict the vehicle’s dynamics and kinematics using its equations of motion. The forces and moments generated by the rotors (Figure 99) were studied and an MMA was created based on the flight mode desired. A PID-based controller architecture was designed as a stability augmentation system for the vehicle. The dynamic model was finalized and prepared for PID controller design and tuning. This dynamic model is versatile and can be easily modified to model any number of rotors.

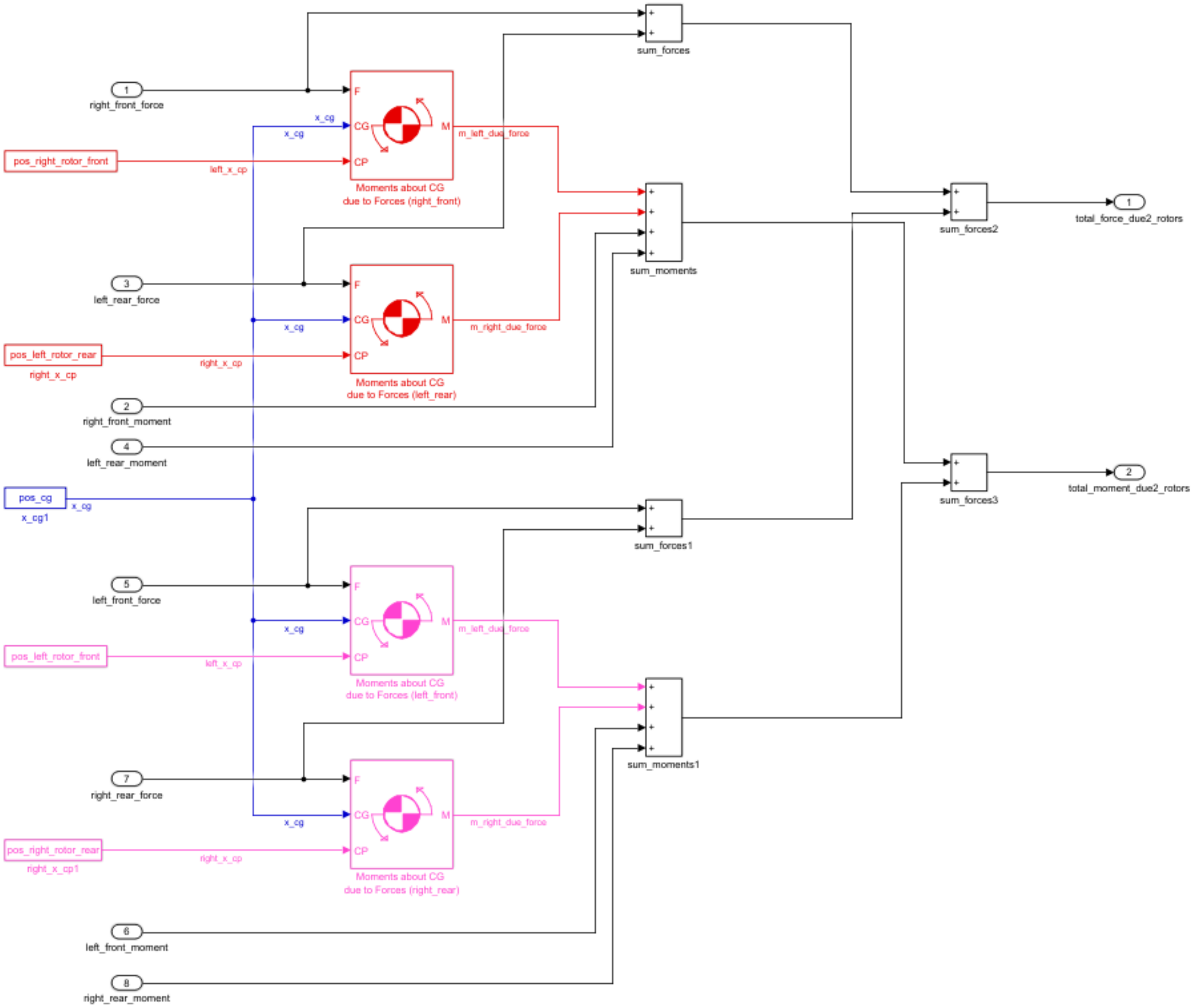

Figure 99. Dynamic model’s rotor forces and moments subsystem

5.10.2 PID controller design and tuning

A rate-only controller was tested as the first step in development of a PID controller for the PAVER vehicle. The angular rates of the vehicle were used as inputs, with the PID controller tuned to maintain the desired rate. An example of a step response for a rate feedback controller is shown in Figure 100 (The MathWorks, 2021).

It was observed that the vehicle had difficulty maintaining its attitude with this controller alone. To address this issue, an attitude controller was added to the outer loop of the rate controller, creating a cascaded PID controller. The PID gains were then modified based on the desired response time, handling qualities, and other relevant parameters. Once the PID controller had been finalized, it was ready for simulated flight-testing.

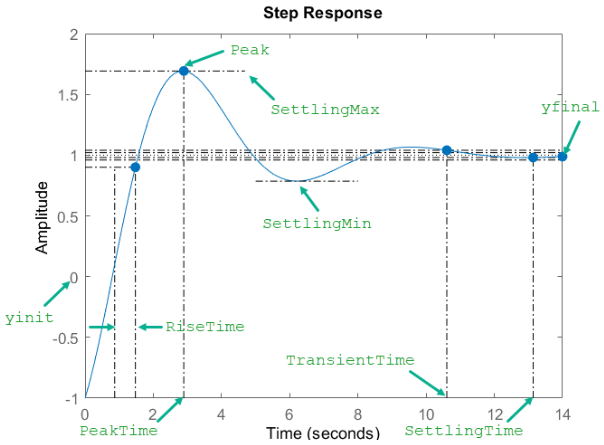

Figure 100. Step response parameters of a feedback controller

5.10.3 Simulated flight tests

The simulated flight tests were carried out using the dynamic model in Simulink connected to FlightGear as shown in Figure 101. These flight tests were performed to gain an understanding of the vehicle’s handling qualities for all three flight modes. These modes were tested under all three flying conditions (nominal, partial failure and full failure of the rotor). These simulated flight tests were used throughout the development of the flight software.

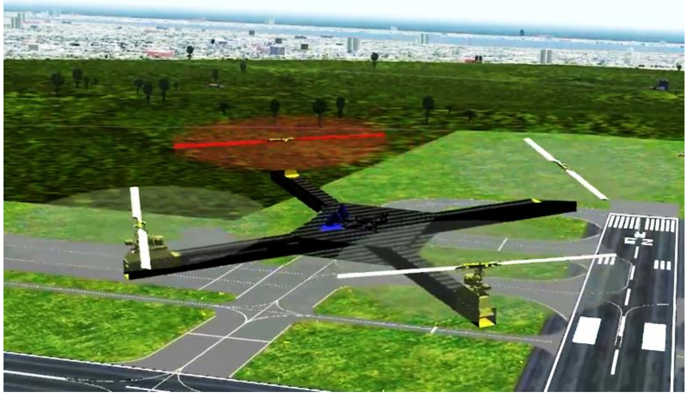

Figure 101. Simulated flight test in flight gear

5.10.4 Flight software development

The flight software is a set of algorithms that run on the vehicle's flight computer, managing the input and output signals for the vehicle. Developed in Simulink, it consists of three main subsystems: input, control/actuation algorithms, and output. The input subsystem receives and processes the incoming PWM signals from the pilot's remote control stick inputs and passes them to the control algorithms subsystem. In this subsystem, the signals are processed using various algorithms and then sent to the output subsystem. Here, the signals are converted to PWM and used to control effectors of the vehicle. The flight software was initially tested by uploading it to the flight controller and verifying the DEP unit servos moved the swashplates in the correct direction based on the pilot input. Figure 102 shows the assignment of channels from the RC controller in an earlier version that had the capability to switch between flight modes VP1 and VP2.

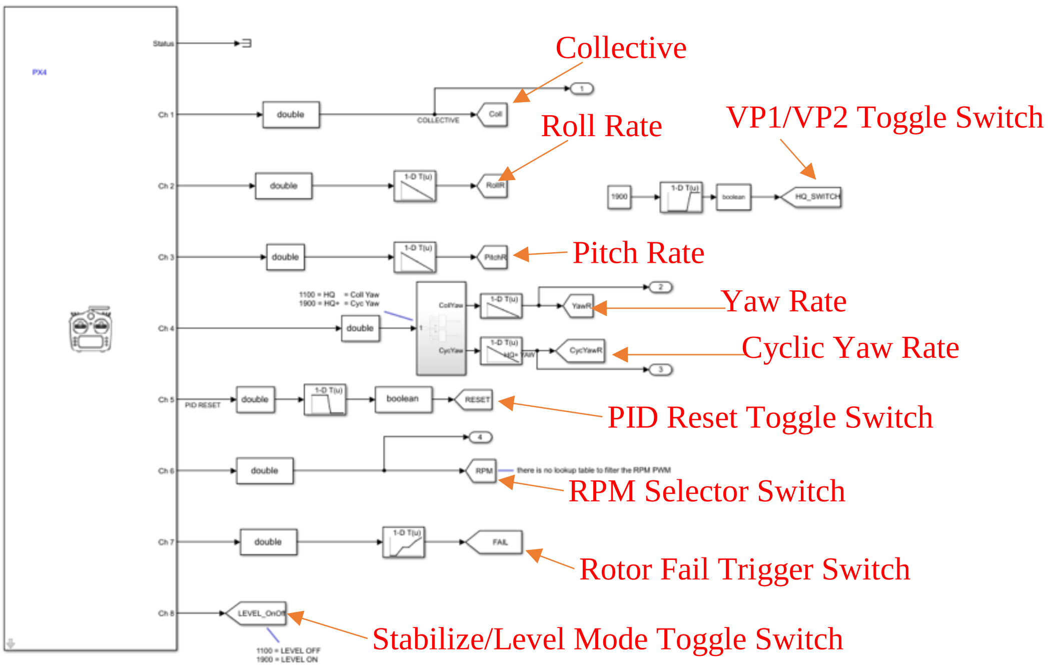

Figure 102. Input commands subsystem of flight controls software

5.10.5 Testing rotor blade control

Functionality verification of the flight software was performed prior to every flight. This was done by visually checking that the individual swashplates of each DEP unit responded correctly to pilot inputs and disturbances. This involved verifying that the rotor blades pitched in the correct direction in response to the PID controller's output when the vehicle was tilted to introduce an attitude disturbance. The data logging system was also checked to confirm that it was properly recording all necessary information. Once the vehicle passed the pre-flight checks performed as shown in Figure 103, it was ready to be tested on the attitude test stand.

Figure 103. Conducting pre-flight checks on cyclic pitch control

5.10.6 Attitude test stand

The attitude test stand (ATS) was used to evaluate the vehicle's angular response to pilot input, as shown in Figure 104. The PID controller gains were tested and tuned on the ATS by comparing the measured Euler angles and rates of the vehicle to the reference values. The PIDs were adjusted to achieve the desired handling qualities and optimize the vehicle's angular response time. Once the attitude test was completed and the PIDs were properly tuned, the vehicle would undergo some basic tethered flights before performing untethered flight tests.

Figure 104. Checking the vehicle’s bank & pitch limits on the ATS

5.10.7 Untethered flight

The untethered flight test was the next phase of testing after completing the ATS tests and initial tethered flights. This phase focused on evaluating the vehicle's translational response and adjusting the PIDs’ gains to meet the desired handling quality requirements. The pilot performed various maneuvers, including roll and pitch doublets and yaw pirouettes, as shown in Figure 105. During this test, the vehicle was untethered but still confined within the test cage.

Figure 105. PAVER performing maneuvers in an untethered flight-test

The vehicle was also flown successfully in hover during a motor-out condition, where a rotor was turned off. Figure 106 shows this flight condition.

Figure 106. PAVER hovering with one rotor off (motor-out condition)

5.10.8 Tethered flight zipline

5.10.8.1 Flight vehicle test harness design and implementation

The vehicle harness is a necessary component for testing the vehicle's performance during forward flight with a zipline. It must be able to withstand the loads experienced in the case of an uncontrolled drop in altitude and must not interfere with the rotors at any angle. The tethering line must also be kept clear of the rotors to ensure safe operation. The first iteration of the vehicle harness is shown in Figure 107.

Figure 107. First iteration of the test harness mounted to PAVER

The harness design selected was made of VECTRAN parachute cord threaded through ¼" aluminum tubes, forming a pyramidal shape. The parachute cord was chosen due to its high tensile strength, as it would carry most of the load during an uncontrolled drop in altitude. The aluminum tubes were chosen to keep the parachute cord from interfering with the rotors when the tether was slack. An adapter was mounted to the top of the harness to connect the four aluminum rods, as shown in Figure 108. This adapter also served as a rotation arrest, preventing the vehicle from banking into the ground or the zipline. It allowed for 30° of rotation before engaging the carbon fiber tube. The carbon fiber tube was mounted to the top of the rotation arrest adapter and connected to the tether.

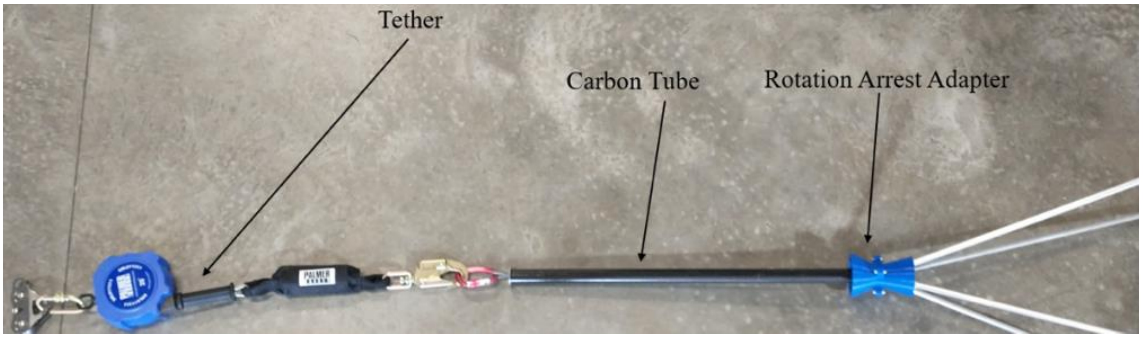

Figure 108. Test harness layout

The carbon fiber tube moved the center of rotation farther away from the mass and increased the moment of inertia, making it harder for the vehicle to rotate. After the initial design, the harness underwent a series of tests to verify its ability to carry the load of the vehicle.

5.10.8.2 Forward flight test matrix zipline design and implementation

The forward flight test matrix was the next phase in the testing process for the single rotor failure scenario. This test matrix consisted of two ziplines, the first of which was located within the drone cage and was designed as a proving ground for the flight vehicle and harness before moving on to the second, larger zipline. The first zipline was strung diagonally across the drone cage at a height of twenty feet from the ground and was approximately 80 feet long. Figure 109 shows this first zipline inside the drone cage.

Figure 109. PAVER strapped to the zipline in the test cage

The second zipline, set up outside the drone cage, was designed to enable testing of single rotor failure during forward flight at higher speeds. It is 400 feet long, with a height ranging from 10 to 25 feet above the ground. Figure 110 shows the second zipline, which includes a support pole made of a four-inch square steel tube welded to a baseplate and topped with a steel pulley for the main cable to rest on. The support pole is eight feet tall and is anchored in place by guy wires.

Figure 110. Support pole on large zipline

Both ziplines were made of a $\frac{5}{16}$" steel cord looped back on itself and secured with cable clamps as shown in Figure 111. A tensioner was added to each of the ziplines in line with the steel cable. The tensioners had the capacity to hold 2000 lbs of tension.

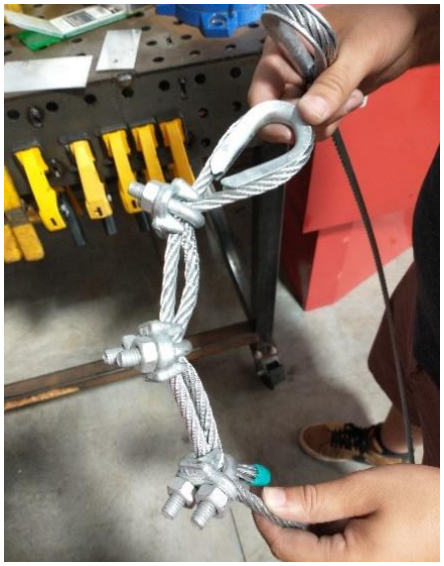

Figure 111. Zipline cable with clamps

A tether system used to support the flight vehicle during forward flight-testing. It consisted of a self-retracting safety line connected to the flight vehicle harness and the zipline trolley. The safety line was designed to catch the flight vehicle in the event of an emergency and had a maximum extended length of 25 feet. It functioned similarly to a seat belt in a car, locking the cable to prevent the flight vehicle from falling further in case of a large acceleration.

Additionally, the tether system was designed to retract so as not to interfere with the rotors when the flight vehicle was changing altitude.

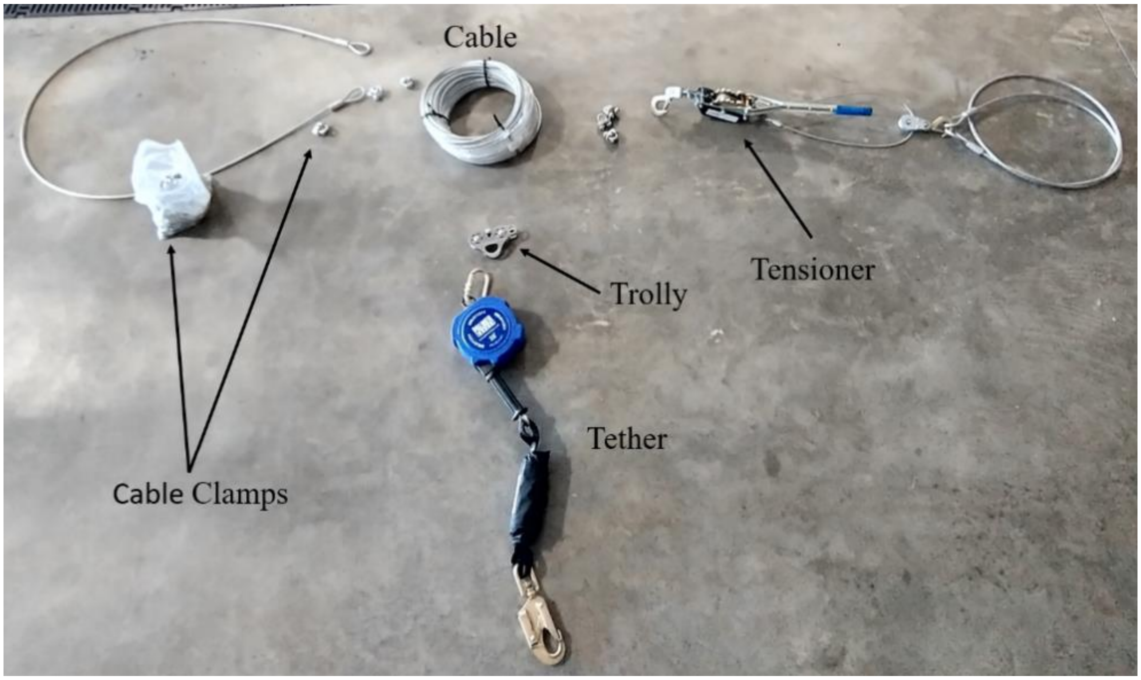

Figure 112. Parts for zipline

The two ziplines will allow the EFRC team to carry out additional tests in both nominal and degraded modes. This will be utilized in future research.

5.10.9 Single arm structural test

During two out of the several flight tests conducted, the vehicle’s arms faced severe vibrations and the pods came apart, resulting in damages to the rotor heads and blades. Upon investigation, it was found that these two flight tests had one thing in common – the operating RPM of the rotor head. Upon further examination, it was found that spinning the blades at/close to this RPM would excite the natural frequency of the arm, causing resonance induced lateral (side-to-side) oscillations. If left unchanged, these lateral oscillations would only amplify upon super positioning while traversing from the end of one arm to the opposite arm of the vehicle. The highest magnitude of these oscillations was felt at the tip of the arms, where the rotor heads were located.

Due to this, most of the flight tests were performed at RPMs lower than the one that caused these damages. In the meanwhile, the team worked on designing a test-rig that would help study the relationship between the rotor’s RPM and the induced lateral oscillations faced by the vehicle’s arms. The test was termed the single arm structural test (SAST), which was conducted on the stand shown in Figure 113 to study the structural characteristics of the arm while under loads from the spinning rotorhead at different RPMs. As seen in the figure, the setup consisted of a circular cantilevered beam with a rotorhead attached to one end. The beam was setup in a way such that it was identical to the PAVER V2 vehicle's arms. A flight controller was secured just underneath the rotor head to record the accelerations (along x, y and z axes) experienced at the tip of the arm.

Figure 113. Single arm structural test setup

The first part of the SAST was to compare the vibrations between 2 and 3-blade rotor heads. In this test, both the configurations were spooled up to about 1500 and 2500 RPM at a fixed collective angle, and a 0º cyclic angle, and their induced accelerations were compared. It was found that the 3-blade configuration did not oscillate as much as the 2-blade under the tested RPMs. Section 5.5.3 highlights additional details on 2-blade vs. 3-blade configurations.

Given that the 3-blade configuration performed better, the team decided to further test this configuration with additional independent variables. This phase of the SAST entailed three independent variables: rotor RPM, collective angle, and aileron cyclic angle, wherein the dependent variables were the induced accelerations/oscillations. This was the second and final part of the SAST, wherein the objective was to find the range of RPM that caused the most and least amount of vibration/acceleration at the pod. Using this data, the best operational RPM range for flight was determined. The test entailed spinning the rotors through the entire RPM range (RPM sweep) at increments of 100. There were several runs within this experiment, wherein the

RPM sweep was performed at different collective and cyclic angles of the swashplate. For instance, Figure 114 below shows the results from an RPM sweep at Collective = 0º, Cyclic = 0º, and Figure 115 shows the FFT plot from this run.

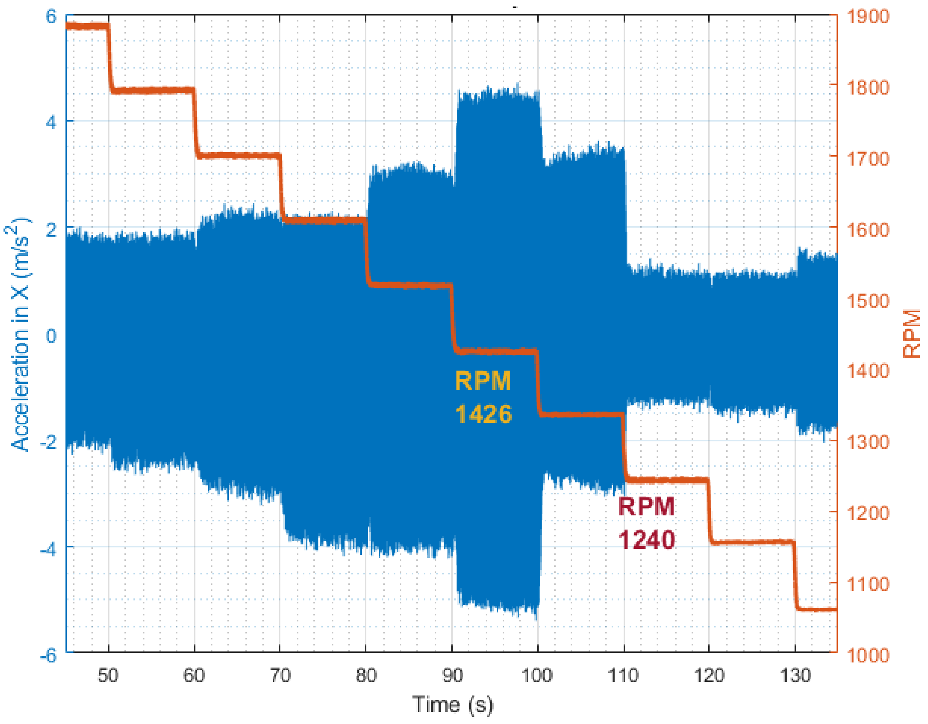

Figure 114. Lateral acceleration at different rotorhead RPMs (Collective = 0º, Cyclic = 0º)

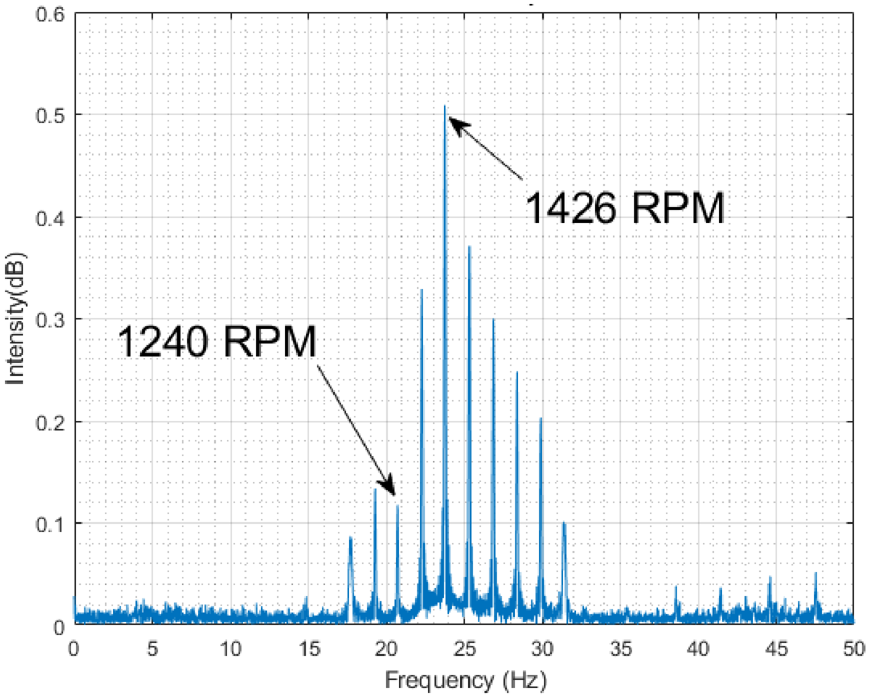

Figure 115. FFT of lateral acceleration at different rotor speeds (Collective = 0º, Cyclic = 0º)

The FFT plot in Figure 115 highlights that the maximum y-axis acceleration in this run was felt at 1426 RPM, and the minimum at 1240 RPM. Upon studying and comparing all the results from every run in this test, it was found that when adding collective, the peaks of the FFT shifted left. This meant that the RPM range producing the most intensity in the FFT plots also shifted left. Given that the test flights were to employ collective and cyclic control, operating at RPMs within 1600 to 1800 was determined to be the best option.

5.10.10 Gyroscopic precession offset

The gyroscopic precession in the rotor heads used was assumed 90 º for the majority of the flight tests. However, while studying and comparing the force and moment data from the RTS tests, it was found that the gyroscopic precession in reality was 45º. This precession offset from the assumed 90º resulted in a loss of control power for the VP2 flight mode during yaw maneuvers, since that was the only maneuver that used cyclic commands. To find out how much of the control power was lost due to this assumption, the percent loss in the total moments produced was calculated by comparing the assumed to the actual moments produced. To demonstrate this, it was assumed that the vehicle used only cyclic control for pitch, and was to perform a negative pitch maneuver by commanding a negative cyclic elevator on all four pods. This command on the clockwise rotating pods (pods 1 and 3) would result in the forces and moments seen in Figure 116.

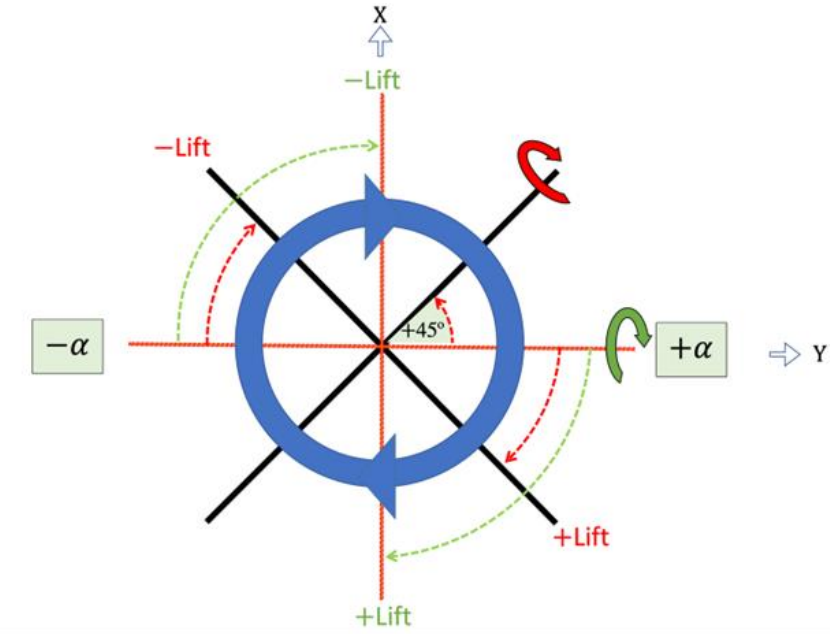

Figure 116. Negative cyclic elevator command on a clockwise rotating pod

As seen in Figure 116, upon commanding a negative cyclic elevator, the clockwise rotating blades will have a $+\alpha+\alpha$ on the right and $-\alpha-\alpha$ on the left, along the y-axis. Due to gyroscopic precession, the positive and negative lift forces, due to the $+\alpha+\alpha$ and $-\alpha-\alpha$ respectively, would be felt after a certain angular displacement along the direction of rotation of the blades. If this angular displacement was 90º, it would produce lift forces along the x-axis of the rotor head, as seen in Figure 116 - labelled in green. This differential lift would in turn produce a moment about the y-axis (also labelled in green in Figure 116), resulting in a negative pitching moment. However, in reality, the angular displacement was 45º along the rotation direction, and resulted in a moment along an axis offset by 45º as well (moment labelled in red in Figure 116). In the case of the counter-clockwise rotating pods (2 and 4), the offset would be the same, but in the opposite direction (-45º). The moments produce by the assumed precession of 90º (Figure 117) were compared to those produced by the actual precession of 45º (Figure 118).

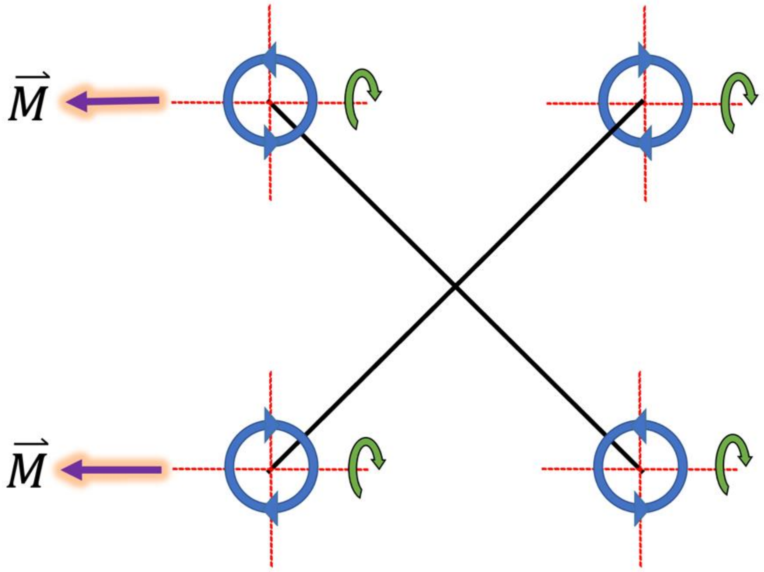

Figure 117. Negative pitching moment vectors produced with assumed precession (90º)

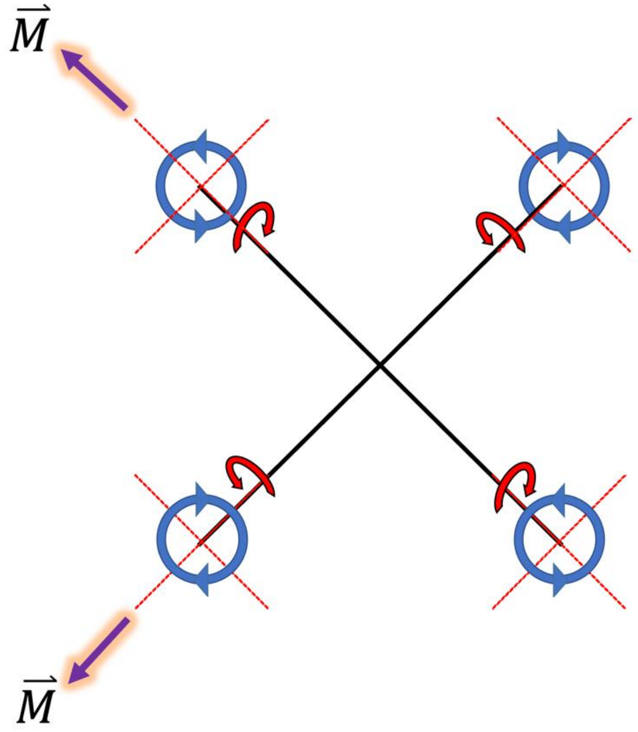

Figure 118. Negative pitching moment vectors produced with actual precession (45º)

The resultant negative pitching moment vector from the assumed precession was calculated to be

$$\vec{R}_{95^\circ} = 2\vec{M} \qquad (3)$$

Whereas that from the actual precession was calculated to be

$$\vec{R}_{45^\circ} = \sqrt{2\vec{M}^2} \qquad (4)$$

Upon comparison, it was found that:

$$\vec{R}_{95^\circ} > \vec{R}_{45^\circ} \qquad (5)$$

by about 30%, proving that the loss in the total moment produced due to the 45° offset was about 30%. After finding this, the flight software for VP2 was updated by accounting for this offset using a rotation matrix in the control mixer for the cyclic yaw commands.

5.10.11 Final test flight

The final test flight was performed on Dec 7, 2022, and accounted for all the lessons learned from the SAST and the gyroscopic precession offset. In that, this test was performed with the 3-blade configuration, at 1800 RPM and the precession offset was accounted for. This was an untethered test flight, using the VP2 flight mode, wherein the test matrix (Table 7) was followed to perform a sequence of maneuvers under both nominal and rotor failure conditions. The rotor that failed was pod 1 of the vehicle, as seen in Figure 119.

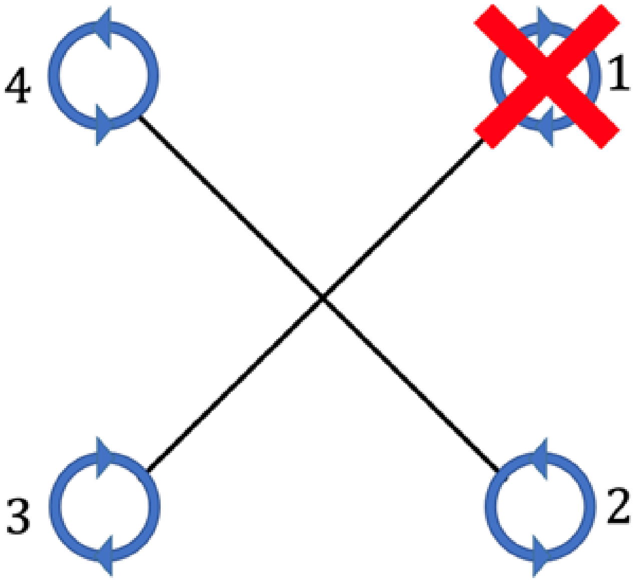

Figure 119.Test vehicle diagram showing failure pod 1

Upon the failure of pod 1, it was theorized that the control laws would stabilize the vehicle by countering the weight of this failed pod - by commanding a steady positive pitch and a negative roll simultaneously. As per the flight software's control mixer, these commands would cancel out in pods 4 and 2, however, they would add up in pod 3, making it solely responsible to counter the weight of pod 1 by producing a constant negative thrust, to stabilize vehicle's attitude, and keep the center of lift from shifting. Section 5.13.1 discusses the effects of the shift in the lift center from the center of gravity in more detail. Figure 120 to Figure 123 compare the nominal flight to the rotor failure flight in terms of the vehicle's tracking performance for the given roll, pitch, and yaw commands, respectively.

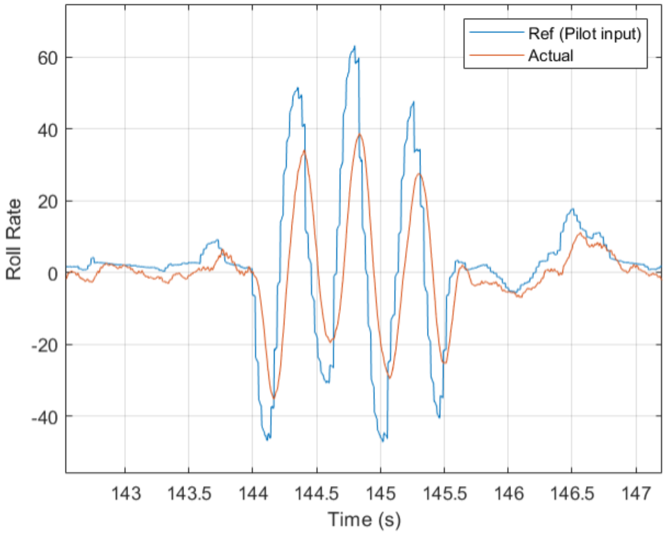

.

Figure 120. Roll rate response under nominal conditions

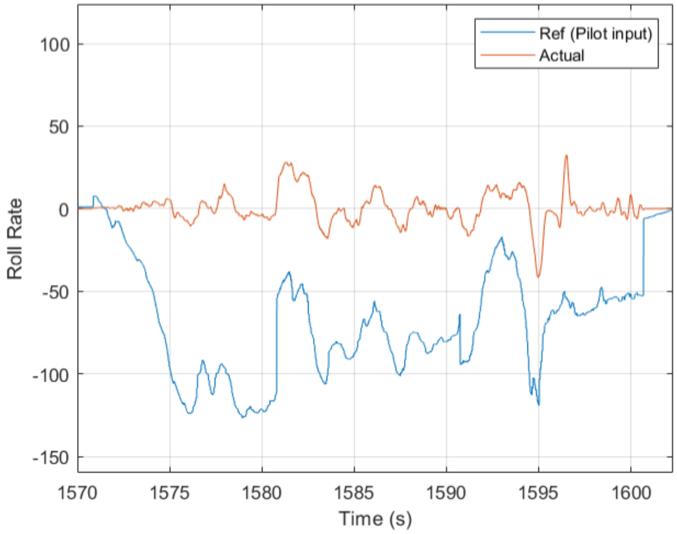

Figure 121. Roll rate response under rotor failure conditions

Upon comparing Figure 120 to Figure 121, it can be inferred that the vehicle tracked the roll rate command a lot more closely under nominal conditions (Figure 120), than under rotor failure conditions (Figure 121). The large offset under the rotor failure conditions consists of a steady state error of about -75 deg/s. This error was caused due to the cascaded nature of the control architecture. This negative roll rate steady state command was given by the controller itself in order to stabilize the vehicle during rotor failure. A similar steady state can be seen in the pitch rate response under rotor failure conditions in Figure 123. These commands together managed to counter the weight of the failed rotor. The reason these steady state commands show up as error in the response plots is that they are compensating for the failed rotor to zero/stabilize the vehicle. Therefore, the controller does not see this as a shift in the zero-point, but instead sees it as an error. This caused unnecessary build up due to the I-term of the PID controller, which ended up causing instability and degraded handling qualities toward the end of the flight. The perturbations from the steady-state error in Figure 121 were due to the feedforward structure of the control system, wherein the pilot’s rate command was directly fed into the inner rate controller loop.

The pitch rate response under nominal conditions in Figure 122 highlighted a steady-state error, proving the need for an increase in the integral gain of the PID controller. The pitch rate response under failure condition in Figure 123, however, had similar characteristics to the roll rate response under failure, as mentioned earlier. It showed a positive pitch steady state error/command to maintain stability of the vehicle.

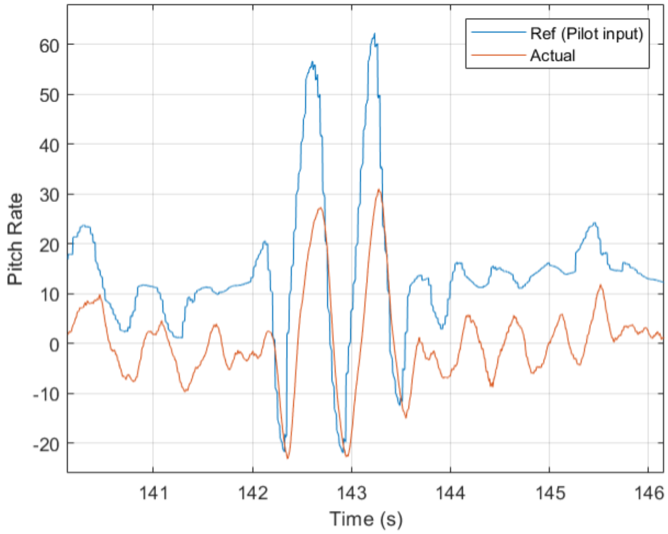

Figure 122. Pitch rate response under nominal conditions

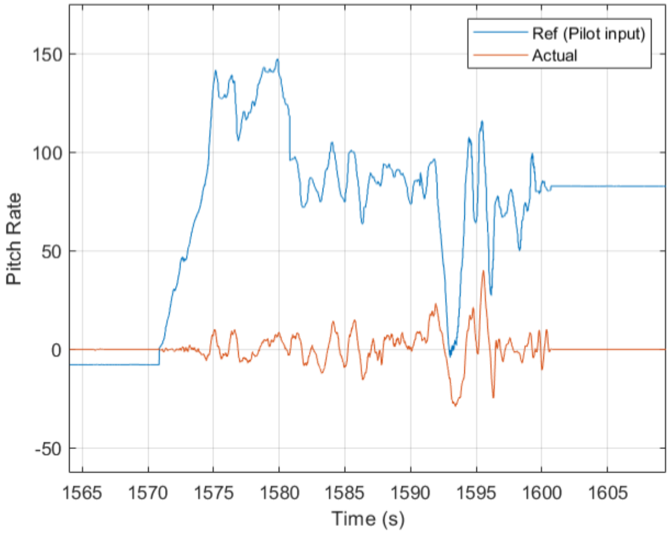

Figure 123. Pitch rate response under rotor failure conditions

Upon rotor failure of Pod 1, the yaw controller must command a negative steady state yaw rate to maintain heading of the vehicle, in turn countering the effects of the failed motor. Figure 124 shows the yaw rate response under nominal conditions, however its tracking is not as accurate as the roll and pitch rate response.

Looking at Figure 125, the reference command here is only that of the pilot. There is no feedforward signal in the yaw rate controller given that it only tracks yaw rate. Figure 125 showed that the pilot's input only made a difference after the 30 deg/s yaw rate mark. This is most likely due to the controller compensating and holding a steady heading using a yaw rate of -30 deg/s. This again proves a shift in the zero-point in yaw. Therefore, the swashplates did not react until the commanded signal reached +30 deg/s. This, however, could also lead to severe I-term build up.

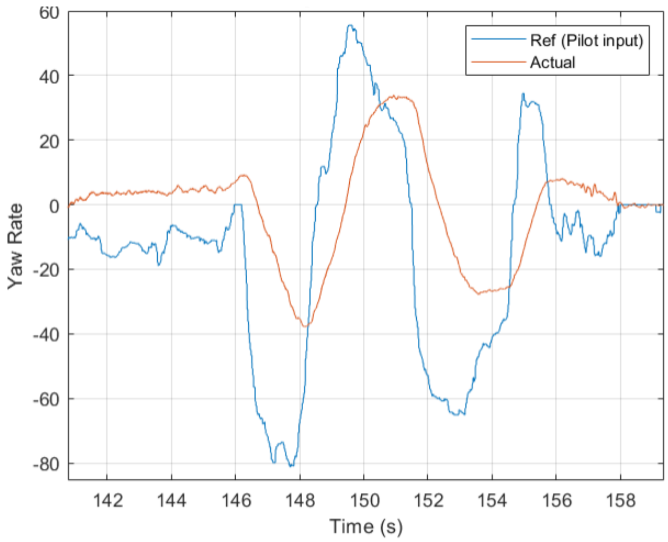

Figure 124. Yaw rate response under nominal conditions

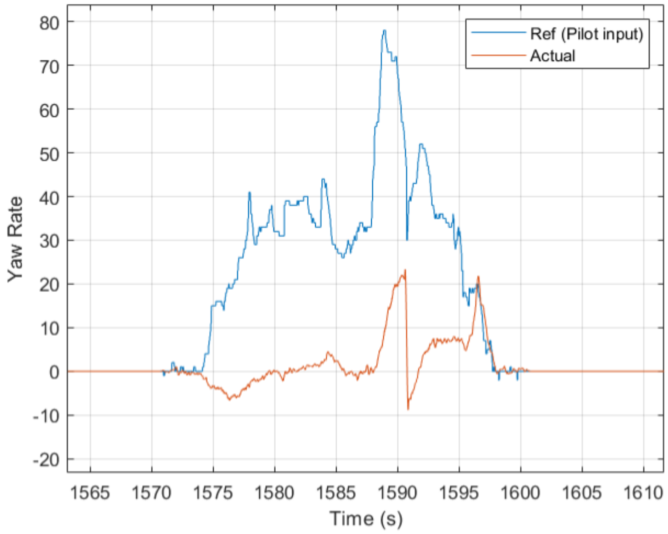

Figure 125. Yaw rate response under rotor failure conditions

Besides looking at just this data, observing the qualitative aspects of the vehicle's performance during the flight test under both nominal and failure conditions showed that this was possibly the most successful flight test conducted in Phase 1 of this project. Earlier, the vehicle could barely lift off the ground during rotor failure due to insufficient lift forces (given the low operational RPM used back then). Performing any maneuvers in those flights were not possible. However, this flight test incorporated all the lessons learned from every past test and proved that it was indeed possible to control the vehicle even with a failed rotor, while still leaving room for improvement in the flight control architecture.

5.10.12 Lessons learned

Flight-testing on real hardware proved extremely valuable and highlighted many different aspects of rotorcraft dynamics, more so when used in a quadcopter configuration. The setbacks and obstacles faced by the team were overcome with great perseverance, and ended up being some of the most significant learning experiences in this project. Listed below are some lessons learned that the team hopes to incorporate into the next phase of this project.

5.10.12.1 Multi-arm structural test

The SAST is limited, in that it is only meant to study the oscillations in one arm. Given the fact the quadcopter's airframe has all four arms connected as one body, and the importance of studying the relationship between the effects of oscillations of one arm on the other, the next version of this test could entail setting up two arms connected to the SAST frame, and studying how the oscillations of both arms traverse through the tube and amplify due to super-positioning. This could later be upgraded to a setup capable of testing all four arms

5.10.12.2 Landing gear & lead-lag damper

The possibility of the vehicle facing ground resonance can be minimized by equipping it with landing gear that is able to dampen any resonance, absorb the vibrations, and keep it from reaching the airframe. Though not straightforward, equipping the rotor-heads of the vehicle with lead-lag dampers will minimize the chance of rotor-failure due to sever flapping or lead-lag offsets during operation. This was a cause of failure during one of the test flights.

5.10.12.3 Data acquisition (DAQ)

The DAQ built into the flight controller was one of the most crucial aspects of this project, and allowed the team to record the vehicle's dynamics, such as roll, pitch and yaw rates and angles. However, it was limited in terms of its sampling rate and number of variables it could record at simultaneously. In the next phase, this DAQ should be upgraded in order to record more variables for a deeper understanding of the vehicle's dynamics. For example, recording the commands sent to each of the 12 servos 4 motor by the controller, especially during failure tests, would greatly help understand and improve the behavior of the control system and mixer.

5.10.12.4 Adaptive control

As mentioned earlier, it was clear from the last flight test that there was still room for improvement within the control system. A major issue of the current controller is that, upon rotor failure, it remains unaware of the pod's failure condition, and continues to send commands to its servos and motors. More importantly, the controller does not identify the shift in its zero-points upon failure. The failure causes the entire plant's (vehicle) dynamics to change, as it goes into this new state. This new state does not only require new controller gains, but would also require a new control mixer, given that the original mixer was for a symmetric quadcopter, and this new state, in a way, turns it into a tricopter with an added weight on one end (pod 1).

Switching control laws and mixer upon failure is one way to tackle this; however, that would only account for two states – nominal and failure of pod 1. Ideally, the flight controller should be designed such that it could adapt to any and every change in state. Implementing adaptive control laws would help the flight controller handle changes in its plant's dynamics in real-time. An adaptive controller combined with fault tolerance would further help detect and correct for any failures in the system. One such adaptive controller is called Model Reference Adaptive Control (MRAC), which is based on dynamic inversion. This controller works by using the inverse state-space model of the vehicle's dynamics as one of the reference signals in its architecture, and constantly compares it to the actual vehicle state. The advantage here is that the vehicle's dynamic model does not need to be completely accurate, as the controller consists of an uncertainty component as part of the adaptive subsystem, which tries to model the disturbances in real-time. This controller gets better with each additional data point, in turn getting more accurate in its curve fitting. The way it works is by constantly refining and adapting to the new plant dynamics, by changing the controller's feedback and feedforward gains (Stevens, Lewis, & Johnson, 2016).

5.10.13 Cascaded feedforward control

The cascaded feedforward controller, shown in Figure 76, is the final version of the controller used in PAVER for all control strategies. It combines aspects of both rate and attitude controllers, with the inner loop tracking rate commands and the outer loop tracking angle commands (Hall, 2012). This controller also has a feedforward loop that reduces the error between the reference and actual command more quickly, improving the efficiency of command tracking. The feedforward loop allows the rate input from the pilot to be instantly commanded into the rate controller (inner loop).

5.11 Task K: Validate vehicle simulation model with test data

The simulation of the complete vehicle dynamic model behavior was developed and validated using MATLAB/Simulink, similar to the rotor model validation in Section 5.6. As shown in Figure 126, the validation process involved iteratively improving the controller and verifying its performance with the Simulink model. This involved designing control laws in Simulink and fine-tuning them for each of the three control strategies, as well as testing and verifying the PID gains and control laws before implementing them on the flight controller. The simulation model was then tested with pilot input to assess the handling qualities and make any necessary adjustments. Once the response was deemed satisfactory, the control model from the simulation was transferred to the flight controller, preparing the vehicle for flight-testing.

After each flight test, the pilot's feedback and post-flight data were analyzed to determine the vehicle's performance. The flight data included angular rates, Euler angles, collective input commands, and sensor measurements. The analysis focused on how well the vehicle tracked the reference command provided by the pilot, and the control gains were modified on the simulation as needed to improve the controllability of the vehicle.

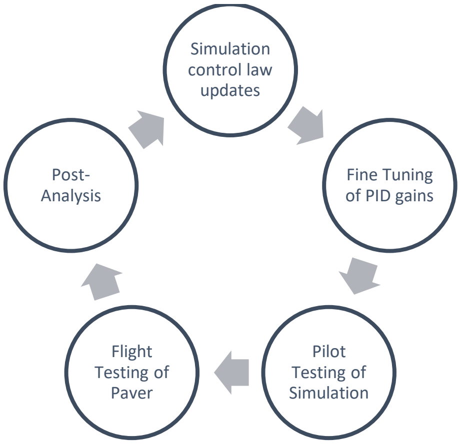

Figure 126. Iterative process of simulation-hardware validation and improving control

In the final phase of testing, the pilot commands from the flight test were fed into the simulator and its response was recorded and compared to that of the actual flight test. While the simulation's response closely matched that of the flight test, it does not necessarily confirm the validity of the hardware and software.

Figure 127, Figure 128, and Figure 129, respectively, compare the pitch, roll, and yaw rates of the vehicle in the flight test to those recorded in the simulation, where both the simulation and flight test share the same pilot input. In all figures, the vehicle response in simulation more closely tracks the commanded or reference values than the actual vehicle does. The reasons for this could be due to the following:

- The simulation does not include any realistic atmospheric wind or turbulence.
- The inertia values used in the simulation are approximations and may not be accurate.
- The simulation does not include any rotor or actuator time delays.

Although the PID gains have shown exceptional performance in controlling the system, it is important to note that this does not necessarily mean that the simulation itself is validated. Other factors may be at play, which would affect the accuracy or realism of the simulation. Additional testing and analysis may be necessary to verify the simulation's validity.

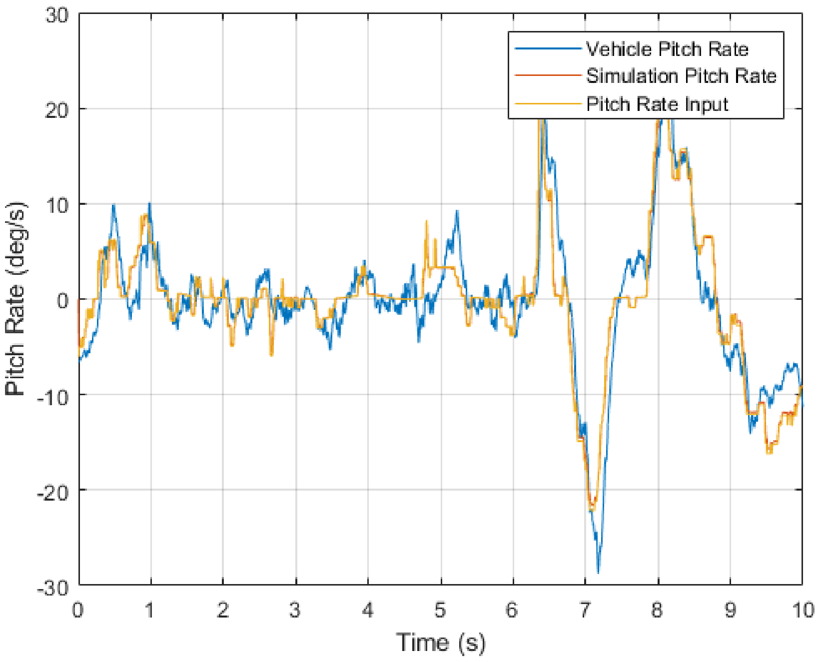

Figure 127. Hardware-simulation validation of pitch rate

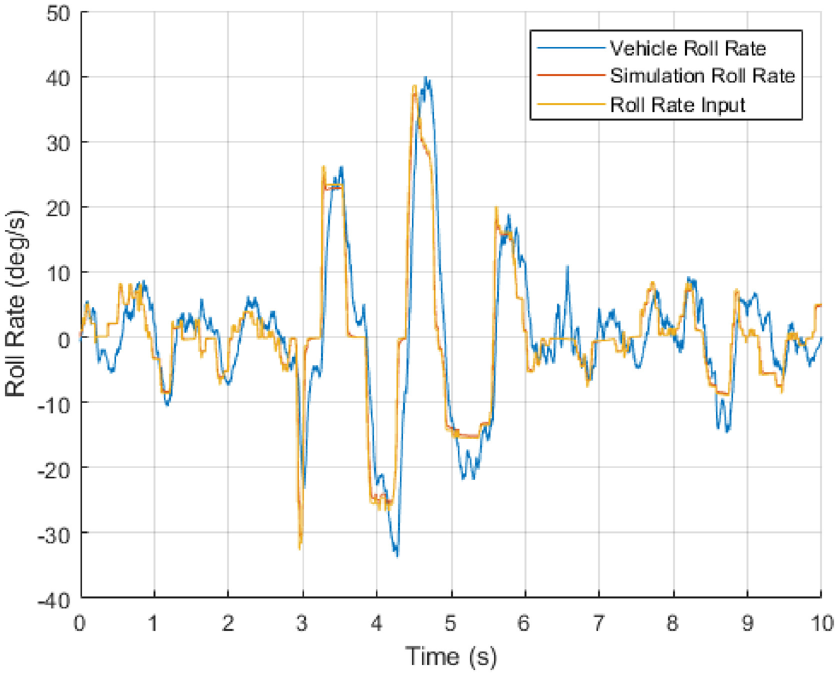

Figure 128. Hardware-simulation validation of roll rate

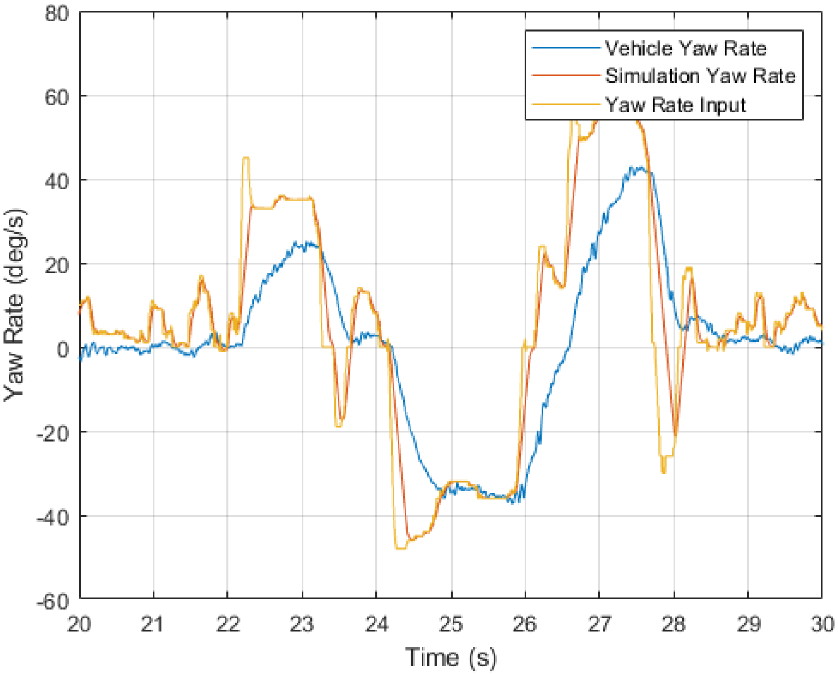

Figure 129. Hardware-simulation validation of yaw rate

5.11.1 Lessons learned: hardware-simulation validation

An important factor addressed during the process of validating the vehicle simulation model with test data was the data logging rates and precision. Many parameters were logged, and it was crucial to decide which parameters required higher sampling rates. For example, the angular rates were logged with a higher precision and sample rate when compared to the collective pilot input and RPM. This was carefully assessed to avoid data loss due to limitations in the flight controller's processing capabilities. External factors that might affect the experimental flight such as gusts were also taken into consideration for validating the hardware and simulation.

5.12 Task L: Simulation of DEP unit failure in 6- and 8-rotor vehicles

The parametric N-rotor dynamic model described in section 5.3 was used to design 6- and 8-rotor vehicle models to compare their performance with that of the quadrotor vehicle in the event of rotor failure. The design of the DEP units was not altered, but their configuration and number were changed based on the model. Other fundamental parameters, such as inertia, vehicle mass, force, and moment integration for each unit, were updated. A new MMA was also created based on the chosen vehicle, which helped to convert pilot commands into vehicle-level distribution of integrated unit and actuator commands. Figure 130 (PX4 Autopilot, 2022) and Figure 132 (PX4 Autopilot, 2022) depict the 6- and 8-rotor vehicles respectively, as well as showing the spin direction of the rotors. Table 8 and Table 9 show the MMAs for the 6- and 8-rotor vehicles respectively, indicating the thrust distribution for positive collective (ascend), roll (right), pitch (up), and yaw (clockwise) maneuvers. Additionally, Figure 131 and Figure 133 show the 6- and 8-rotor vehicles in FlightGear, with the rotor in red representing the vehicle's failed rotor.

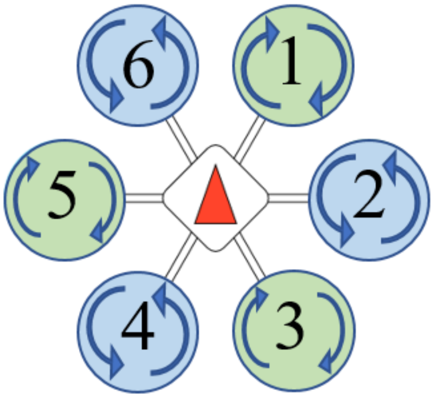

Figure 130. Hexarotor

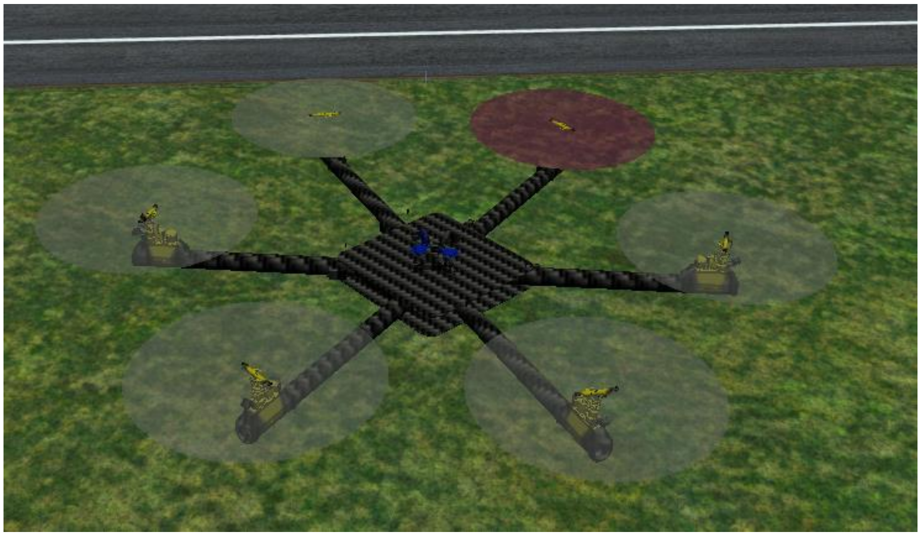

Figure 131. Hexarotor in FlightGear

Table 8. Hexarotor MMA

Input	Rotor					
	1	**2**	**3**	**4**	**5**	**6**
Collective	+	+	+	+	+	+
Roll	-	-	-	+	+	+
Pitch	+	0	-	-	0	+
Yaw	-	+	-	+	-	+

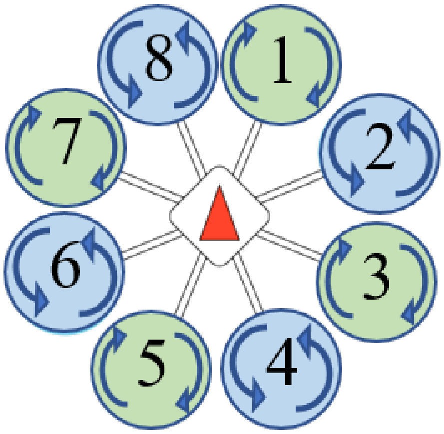

Figure 132. Octorotor

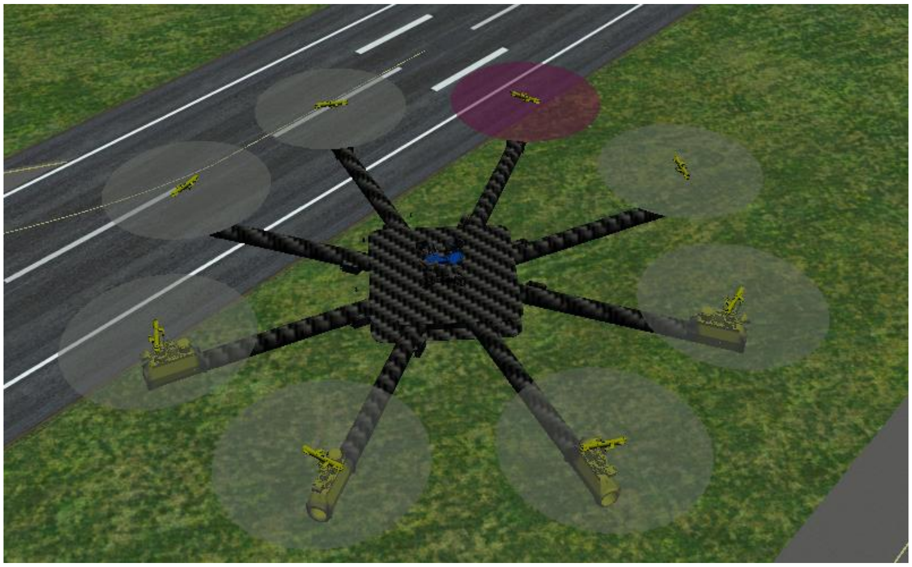

Figure 133. Octorotor in FlightGear

Table 9. Octorotor MMA

Input	**Rotor**							
	1	**2**	**3**	**4**	**5**	**6**	**7**	**8**
Collective	+	+	+	+	+	+	+	+
Roll	-	-	-	-	+	+	+	+
Pitch	+	+	-	-	-	-	+	+
Yaw	-	+	-	+	-	+	-	+

In the VP1 flight mode, the dynamic models for both the 6- and 8-rotor vehicles were tested under rotor failure conditions. Rotor 1 of each vehicle (as labelled in Figure 130 and Figure 132) was failed in simulation at t = 10 seconds and the vehicles were made to perform a set of preprogrammed maneuvers, similar to those performed by the quadrotor under failure scenarios in section 5.8. The results of these tests were then compared to those of the quadrotor in Task H in VP1 mode under failure conditions. This allowed for a comparison of the performance of the 6- and 8-rotor vehicles with that of the quadrotor under similar failure conditions.

5.12.1 Single rotor failure of 6-rotor vehicle in VP1 flight mode

The 6-rotor vehicle's response to a simulated failure of its DEP unit was studied by failing a single rotor and recording its response to commanded maneuvers at a constant collective pitch of 6º in the VP1 flight mode. The simulated failure occurred at t = 10 seconds, and the simulation lasted for 70 seconds. Figure 134 shows the actual rate response compared to the reference maneuvers. Figure 135 shows the rate response of the vehicle in normal conditions for comparison.

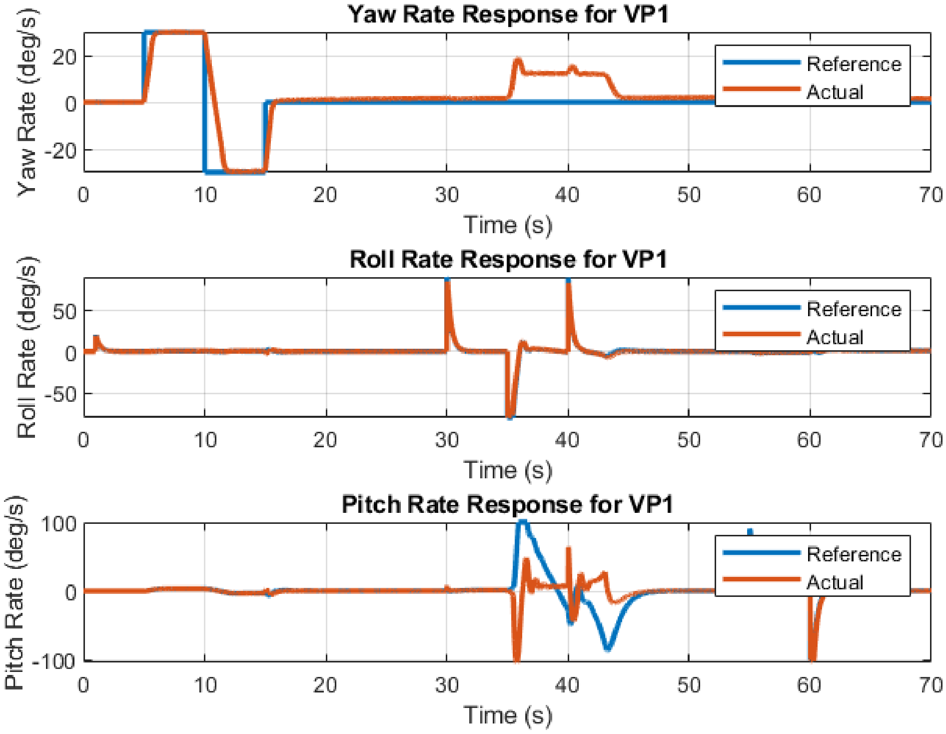

Figure 134. Rate response for 6-rotor vehicle after single rotor failure in VP1

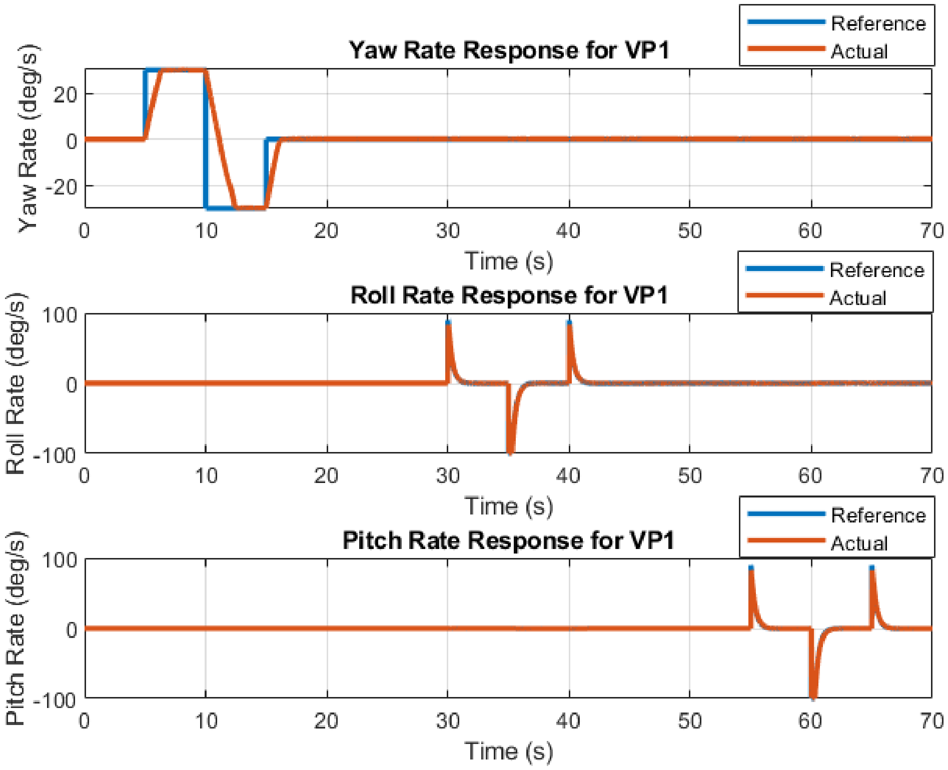

Figure 135. Rate response for 6-rotor vehicle in nominal flight - VP1

The 6-rotor vehicle demonstrated better stability and controllability than the quadrotor in VP1 flight mode upon a single rotor failure. The yaw and roll rates showed deviations from the reference command at around 40 seconds, but overall, the vehicle was able to track the reference rates closely.

5.12.2 Single rotor failure of 8-rotor vehicle in VP1 flight mode

The performance of an 8-rotor vehicle with failed DEP unit was evaluated by simulating a failure of a single rotor and examining the vehicle's response to commanded maneuvers at a constant collective pitch of 7º in VP1 flight mode. The simulated failure occurred at t = 10 seconds, as indicated by the blue dotted line in Figure 136, and the simulation lasted for a total of 70 seconds. Figure 137 shows the rate response of the vehicle in nominal mode for comparison.

The results, shown in Figure 136, demonstrate that the 8-rotor vehicle was able to track the reference rate with high accuracy. When compared to the rate response of a quadrotor in VP1 shown in Figure 92, it can be seen that the 8-rotor vehicle was able to track its reference command accurately, showing no deviations.

Comparing the rotor fail responses of the 6- and 8-rotor vehicles, it was found that the 8-rotor outperformed the 6-rotor in both rate and altitude response characteristics.

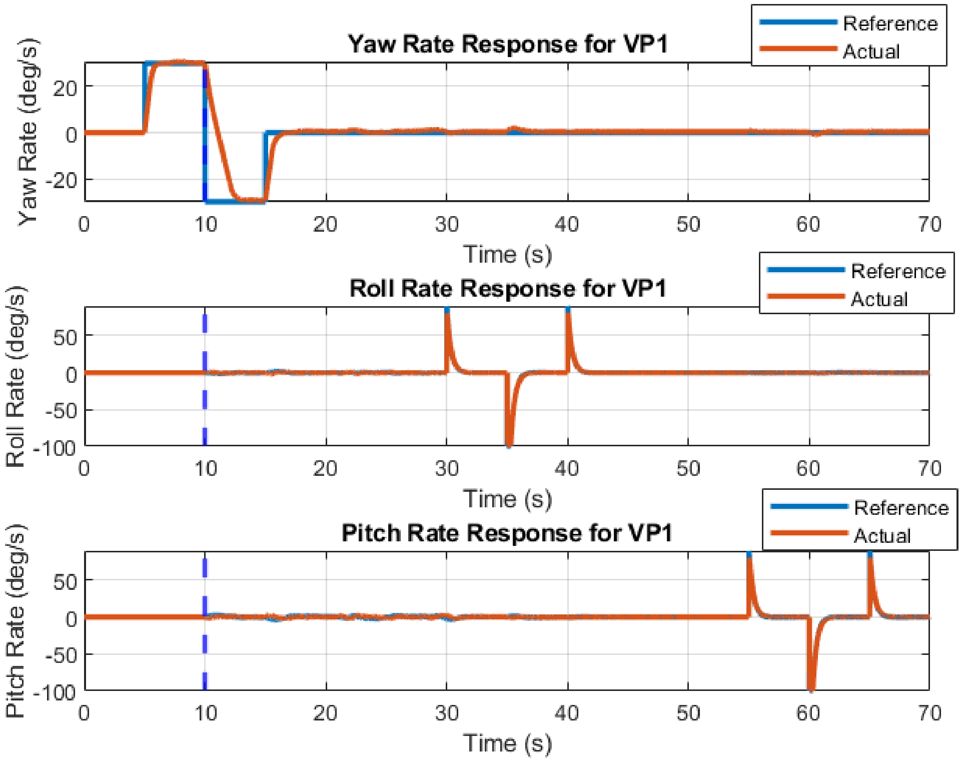

Figure 136. Rate response for 8-rotor vehicle after single rotor failure in VP1

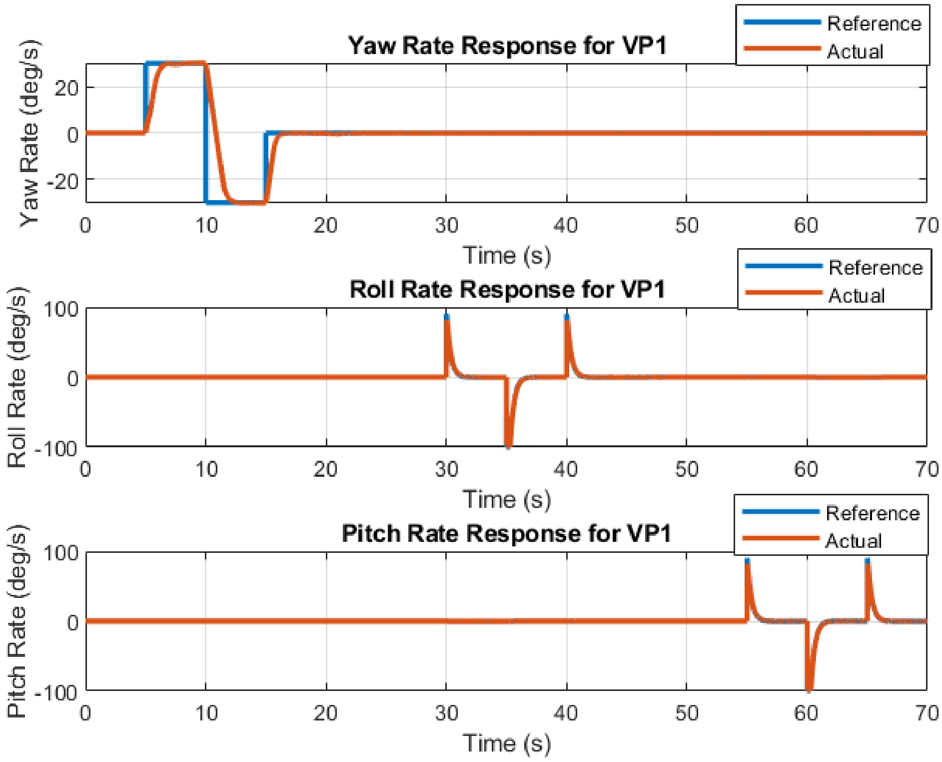

Figure 137. Rate response for 8-rotor vehicle in nominal flight - VP1

5.12.3 Lessons learned

Conducting the initial failure tests in hover mode would have allowed for a comparison of the vehicle's altitude before and after the failure. This would provide a more accurate assessment of the vehicle's performance. Future research will include the implementation of an altitude controller and altitude logging method.

5.13 Task M: Integrate test results with literature review

5.13.1 Vehicle thrust-to-weight requirements for FTC

Effective FTC using thrust and moment control methods requires a specific thrust-to-weight ratio for a vehicle to maintain stability after a rotor failure. When a rotor fails, the center of lift/thrust shifts away from the center of gravity, creating a moment around the center of gravity that must be counteracted to maintain stability. This moment is equal to the thrust multiplied by the offset distance between the center of lift/thrust and the center of gravity.

Assuming that the weight of the vehicle is constant, and the arm has a length of one unit, the offset distance between the center of lift/thrust and the center of gravity will vary based on the number of rotors. When the rotors are evenly distributed in the plane of rotation around the vertical axis through the vehicle's center of gravity (CG), as the offset distance decreases, the number of rotors increases. This relationship is shown in Figure 138 to Figure 140, which demonstrates that the percentage offset for 4, 6, and 8 rotors is approximately 33%, 20%, and 14% of the arm's length, respectively. It is important to note that these values are specific to the case where the rotors are providing the same amount of thrust at the moment when a failure occurred.

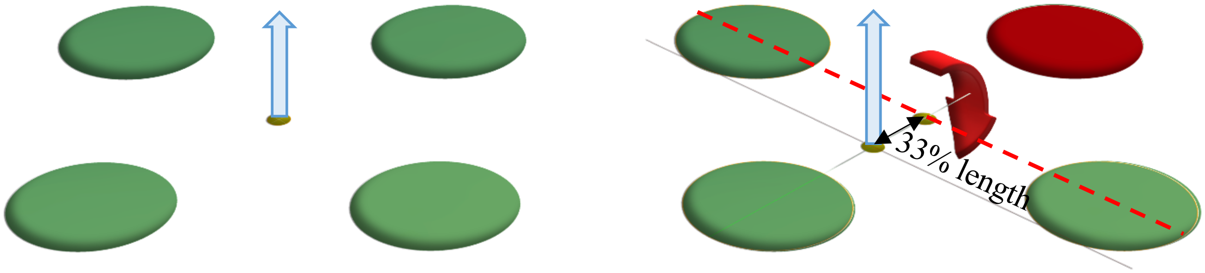

Figure 138. The theoretical lift-center offset when 1 out of 4 rotors fails

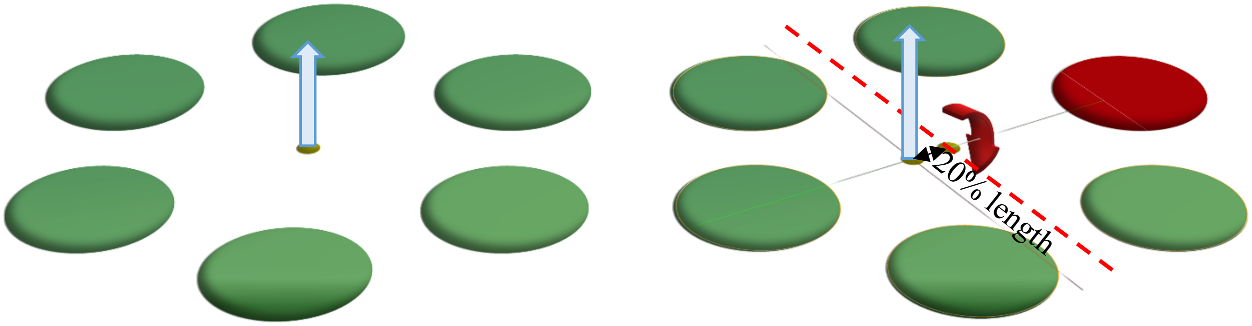

Figure 139. The theoretical lift-center offset when 1 out of 6 rotors fails

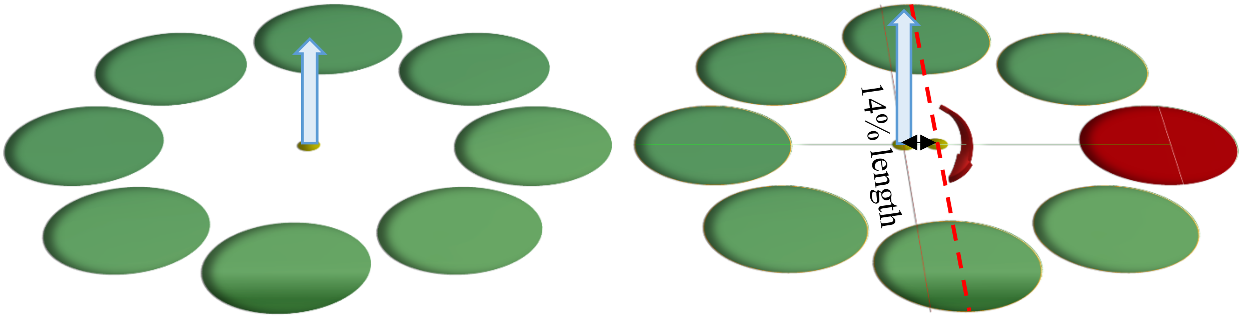

Figure 140. The theoretical lift-center offset when 1 out of 8 rotors fails

In the figures shown, the straight blue arrows represent the lifting force acting from the center of thrust, the green circles represent the functioning rotors, and a curved red arrow represents the moment caused by the failure of the rotor colored in red. The resulting moment, acting around the red dashed line through the vehicle's center of gravity (CG), can be represented by the remaining thrust multiplied by the offset distance at the moment of failure. For example, in Figure 138, the quadcopter has a thrust of ¾ units at the moment of failure, with an offset distance of 0.33 units, resulting in a moment of 0.25 units $(thrust \cdot length)$. The values for the 6 and 8 rotor configurations are 0.17 and 0.12 units, respectively. Despite the increase in remaining thrust, the theoretical resulting moment at the moment of rotor failure decreases as the number of rotors increases.

There are two methods shown in Figure 141 for balancing a vehicle using thrust and moment control in the event of a rotor failure. The first method is to remove thrust from the opposite side of the rotation axis, which can be achieved by stopping a rotor or decreasing the thrust of multiple rotors if the distribution is not axisymmetric. The second method is to use moment control, in which all rotors continue to generate thrust while each rotor contributes to an equal and opposite net moment to balance the failed rotor. These methods allow for the maintenance of stability and control of the vehicle despite the loss of one of its rotors.

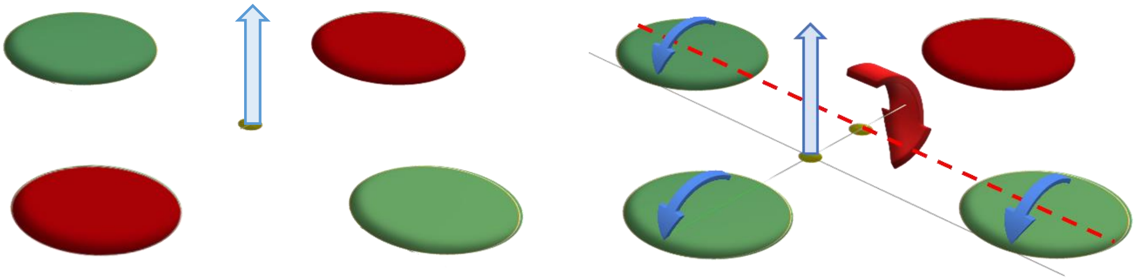

Figure 141. Concepts of failure tolerant DEP inputs with moment and thrust control

Theoretically, the minimum thrust-to-weight ratio required with thrust control is $\frac{f \cdot n}{n-2 \cdot a}$ where f is the factor of safety, n is the total number of rotors, and a is the number of malfunctioning rotors. It is expected that the thrust-to-weight ratio required for moment control with cyclic input would be lower, but during the test, little to no positive collective input was observed. This suggests that the thrust generated by the opposite rotor is minimal. It should be noted that a quadcopter will not be controllable with only two rotors without cyclic/moment control. A theoretical limit for the minimum thrust-to-weight ratio with a factor of safety ranging from 1 to 1.5 is shown in Figure 142. The effect of the number of rotors and the use of cyclic moment control on the performance of the vehicle are topics for further study.

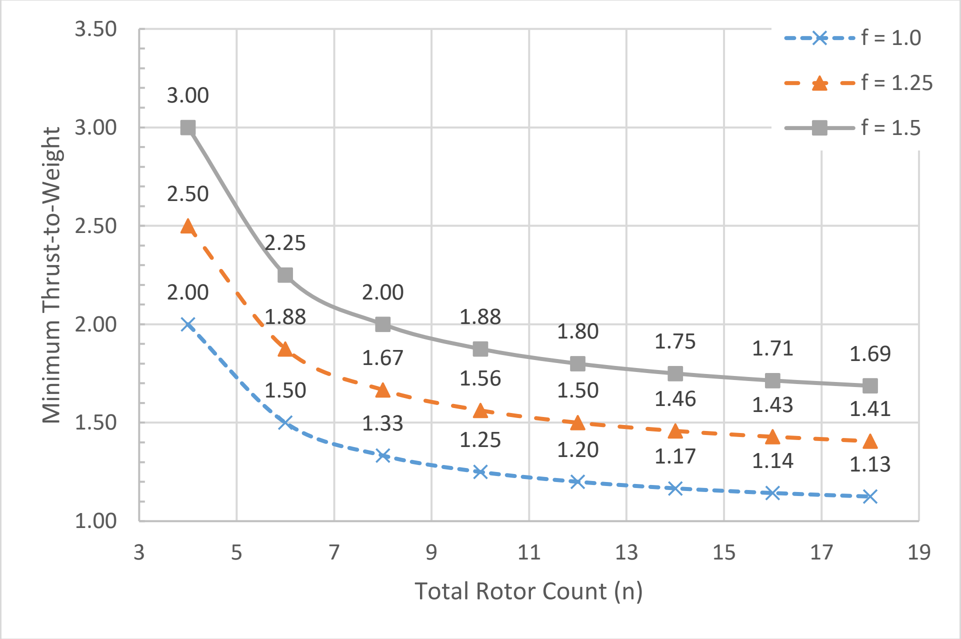

Figure 142. The minimum thrust-to-weight ratio for varying numbers of rotors

The simulations conducted in Task H demonstrate the difference between using thrust control and moment control to balance a vehicle following a rotor failure. As shown in Figure 92, the vehicle is not controllable in the yaw axis and experiences instability in pitch and roll. The vehicle crashed due to the lack of sufficient thrust, though even if the vehicle had sufficient thrust, the uncontrolled spinning would not be acceptable for humans onboard. In contrast, the results shown in Figure 94 indicate that the vehicle was able to maintain control and continue flying in the simulation after an initial deviation occurred following rotor failure. This demonstrates the effectiveness of moment control in maintaining yaw stability and control of the vehicle in the event of a rotor failure.

5.13.2 Multi-copter rotor vibration

One of the major challenges encountered during the testing of the vehicle was the issue of vibration. The blade motion of the PAVER testbed differs from that of traditional rotorcraft, leading to unique vibrational characteristics. The vibration of multi-copters with helicopter controls is a novel issue that has not been extensively studied in the literature. However, the team was able to draw upon existing research on traditional helicopters to understand and address the vibrational anomalies experienced during testing.

Articulating blades are necessary for the successful flight of rotorcraft, as first demonstrated by Juan de la Cierva (Leishman, 2006). The rotorhead of a rotorcraft typically has three hinges that allow the blades to flap, feather, and lead/lag. The flapping hinge "allowed the individual blades to flap up and down freely in response to the changing lift forces seen by the blades during their rotation, balancing aerodynamic forces on the machine, and all but eliminating adverse gyroscopic forces and blade root stresses" (Leishman, 2006, p. 700). The vertical hinge allowing lead/lag is necessary to “alleviate in-plane Coriolis induced forces” (Leishman, 2006, p. 700).

As the blades articulate, the center of mass (CM) of the blades may change, causing the CM of the rotor disc to shift away from the main shaft. This imbalance in-plane results in the horizontal displacement of the DEP units, and cannot be damped out by the rotor disc. In order to address vibration issues, the PAVER testbed was initially equipped with off-the-shelf 2-bladed rotorheads, which were later replaced with a 3-bladed assembly.

The dynamics of blade motion have been studied extensively, with National Advisory Committee for Aeronautics (NACA) conducting research in the 1940s on the three types of vibrations that can occur: "ordinary, self-excited, and shaft critical" (Coleman & Feingold, 1958). Of these, the two types of vibration that have the most significant impact are self-excited and shaft critical. Ordinary vibrations occur during spool-up, but are typically damped out once the blades are straightened by centrifugal force.

Self-excited vibrations, also known as odd-frequency vibrations, are more dangerous and are shown in Figure 143 to occur when the vehicle lifts off from the ground. In this mode, "a slight disturbance will tend to increase with time instead of damping out" (Coleman & Feingold, 1958). The arms of the rotorcraft deflect horizontally, with the DEP units and arms on the opposite side of the vehicle reacting to the force caused by the disturbance on one arm. If the vibration is not damped, the mirrored rotor blades can eventually sync up and swing out of phase, leading to instability.

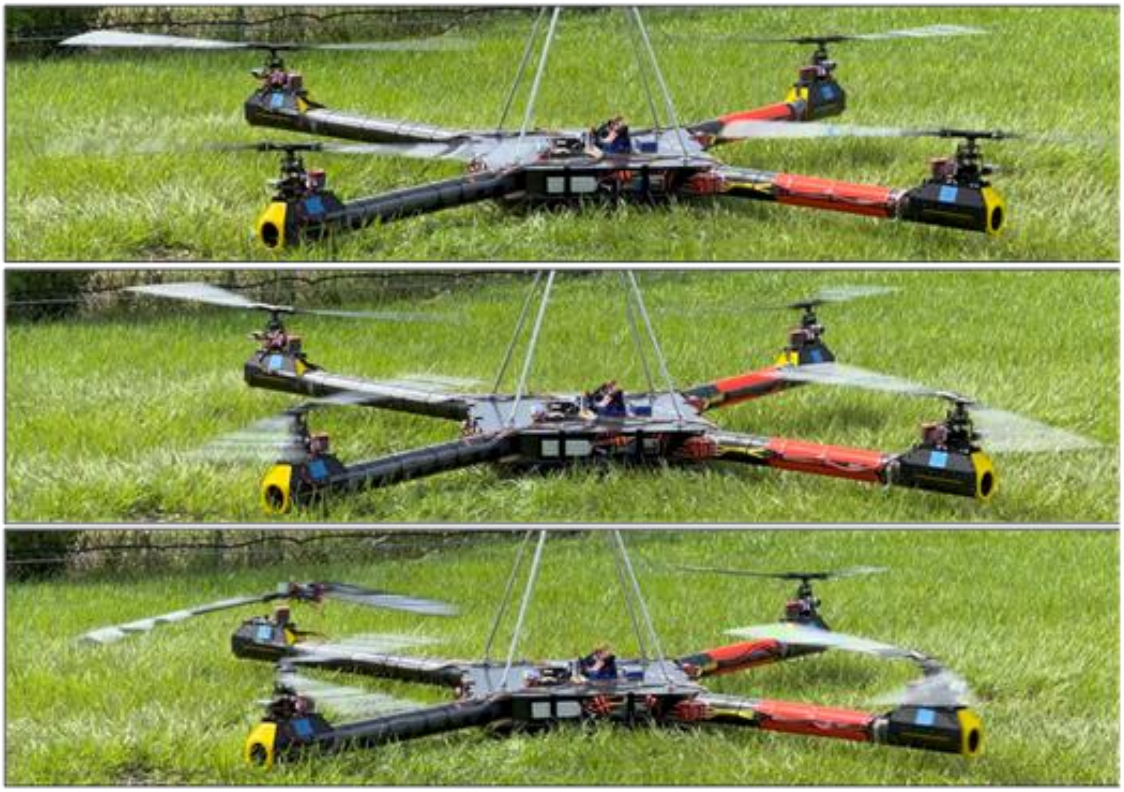

Figure 143. Key frames of PAVER ground resonance

The other type of vibration is known as shaft critical vibration, or one-to-one frequency vibration. This type of vibration was tested by running a rotor attached to a stand-alone arm with zero pitch, as shown in Figure 113. The experiment was conducted with 2- and 3-bladed rotorheads spooling up from 1400 RPM and 2300 RPM, and vibrational data was logged to an SD card in the Pixhawk, plotted in Figure 114.

The data showed that shaft critical resonance occurred when the unbalanced rotors "excite vibration that has peak amplitudes at certain rotational speeds" (Coleman & Feingold, 1958). In this case, the resonance was observed at approximately 1000 RPM, where the vibration was more severe than at other frequencies. The rotor was more stable when running at 2300 RPM compared to 1400 RPM, as shown in Figure 144. These studies provide insight into potential ways to mitigate the resonance caused by rotor vibration.

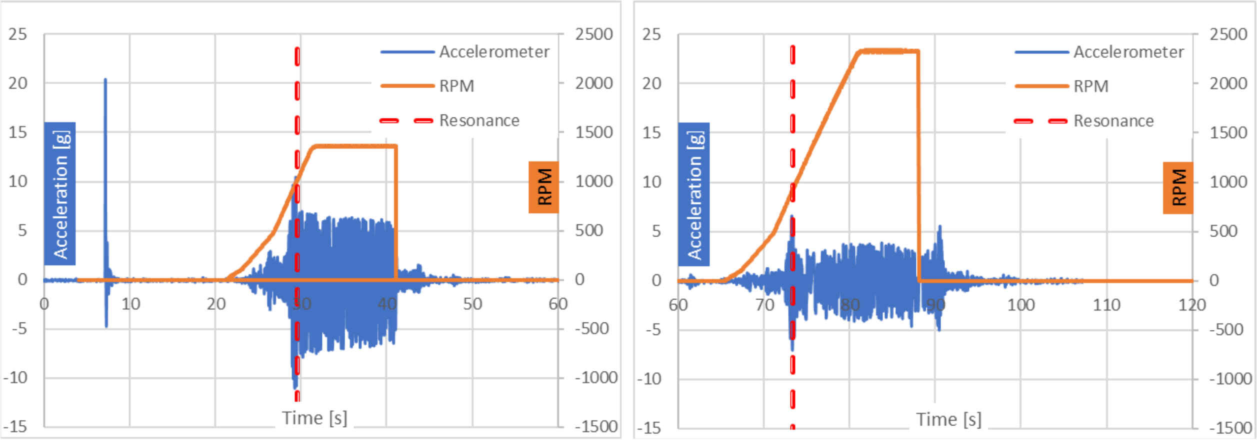

Figure 144. The vibration magnitude and RPM plot for 3-bladed rotorhead

The characteristics of a 3-bladed rotor differ from those of a 2-bladed rotor, and as a result, have different dynamic models. A 2-bladed rotorhead does not have polar symmetry, which is defined as the "absence of a preferred direction in the plane of the rotor" (Coleman & Feingold, 1958, p. 281). This results in different properties, as shown in Figure 145.

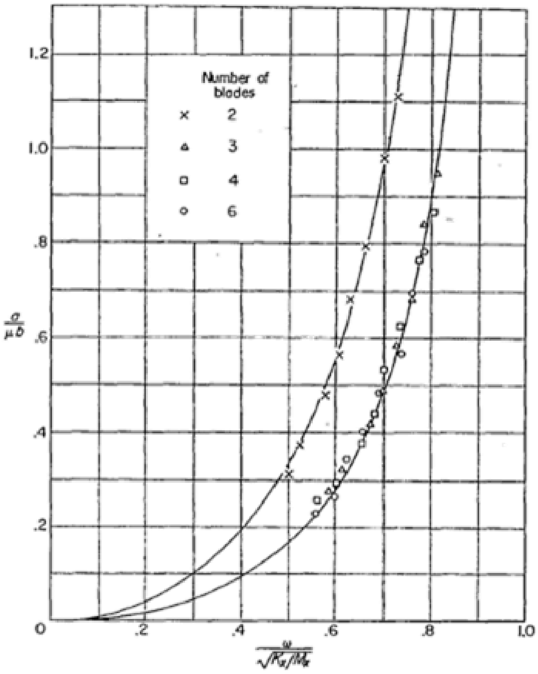

SYMBOLS

α	radial position of vertical hinge
μ	mass ratio, $\frac{nm_b}{m_f+nm_b}$
b	distance from vertical hinge to center of mass of blade
ω	angular velocity of rotor
K	spring constant
M	total effective “mass of blades and pylon

Figure 145. Experimental critical speeds on small models

The vibration modes of a 2-bladed rotor are generally elliptical, while those of a 3-bladed rotor are circular. This results in six natural frequencies for 2-bladed rotors and four natural frequencies for 3-bladed rotors (Coleman & Feingold, 1958), making the problem more complex. In addition, the 2-bladed design "gives rise to a range of rotor speeds in which self-excited divergence of the rotor occurs" (Coleman & Feingold, 1958, p. 288). Two shaft critical speeds bound this instability region, while 3-bladed rotors only have one shaft critical speed with no associated instability region.

The vibration reduction of a 3-bladed rotorhead was tested using a single arm. As shown in Figure 146, both rotors were spooled up to the same RPM range, but the 3-bladed rotor showed less acceleration at the end of the carbon fiber arm. This is true for both self-excited vibration and sustained vibration at an ordinary, constant rotor speed.

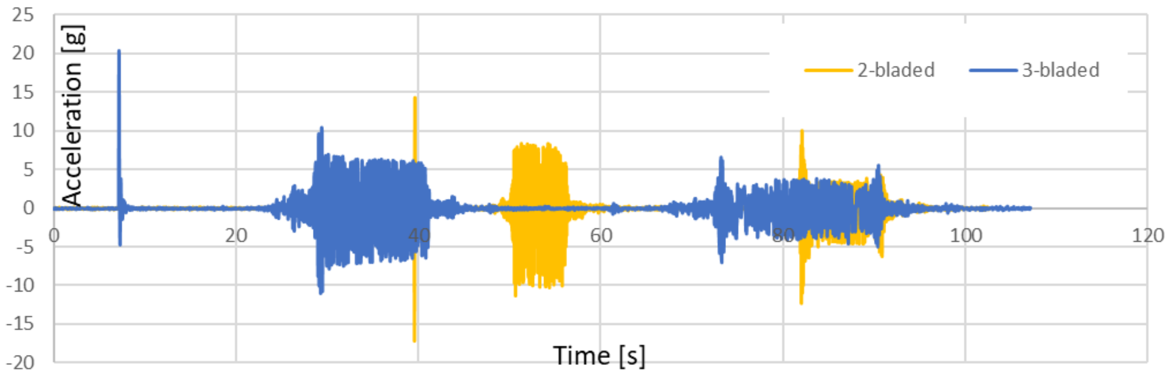

Figure 146. Vibration comparison of 2- and 3-bladed rotorheads

Vibration on a subscale rotorhead can be difficult to identify, model, and predict due to the many possible causes and modes of vibration of different rotor designs. The properties of these systems can vary widely, and using incorrect assumptions or equations can lead to inaccurate models. To avoid damage caused by vibrations, it is possible to operate the rotor at a different state or modify the properties of the rotor system. In addition to changing the damping and spring factors around the hinge axis, changing the design from a 2-bladed to a 3-bladed or more rotorhead can greatly affect the characteristics of the system.

Based on this study, it was found that the 3-bladed rotorhead was more stable than the 2-bladed design. Replacing the 2-bladed design with a 3-bladed one was a simpler solution to the previously experienced resonance issue. The increased solidity also allowed for operation at a rotor speed lower than the bound of the problematic frequency range.

5.13.3 eVTOL control allocation and simplified vehicle operation

To date, there are hundreds of concepts for Urban Air Mobility (UAM) vehicles being developed. The flight dynamics and handling qualities of these vehicles are in many ways different from those of fixed-wing airplanes and helicopters for which the FAA has certification standards. Handling qualities evaluations using actual flight tests are routinely performed on new type certificate applicants as part of the certification process. To make this process – as well as future mission flights – as safe as possible, pilots will need to know where their safety margins are. Through more than a century of flight tests of airplanes and helicopters and many accidents, test pilots have gained a general understanding of the margins, which, if crossed, would cause the vehicle to depart controlled flight. However, the flight envelopes of the many unconventional multirotor UAM concepts being researched are not as well understood. Methods are needed to quantify these prior to initial test flights in order to prevent any mishaps.

In general, the eVTOL and UAM vehicles that are emerging in the market tend to be over-actuated, which means that they have more control surfaces and actuators than required for nominal operation. In order to determine optimal control laws for these vehicles, control allocation methods must be employed. When failures occur to elements of the propulsion and/or control systems, the over-actuated design may allow for a reconfiguration that enables continued flight to a safe landing. To prepare for this, control allocation methods must be used in simulations as part of a failure modes and effects analysis.

Moreover, planning for these vehicles should include setting requirements for thrust-to-weight ratios so that the remaining rotors have enough thrust to provide lift and control in the event of total power loss on a rotor. Part of this planning must also include predicting the force and moment capability of the bare airframe in both nominal and failed modes.

There has been some research that has merged control allocation methods with the prediction of attainable moments (Durham, 1994), which can be leveraged in future phases along with other sources to assist in the development of a force and moment envelope prediction methodology. These force and moment envelopes could be created by assuming the effectors can move to their extents in an ideal way, without any commands from a control law. This would yield the maximum force and moment the vehicle is capable of producing and in general, it would be a function of the state of the vehicle. By predicting the forces and moments required for a specific configuration to fly a given trajectory and comparing them with the predicted force and moment envelopes of that configuration, a necessary condition can be established about the vehicle's ability to fly that trajectory. However, this may not be sufficient as the control law that translates the pilot’s commands to the fly-by-wire effector actuator movements on the airframe may limit those force and moment envelopes. The actuators themselves will also have rate and saturation limits.

With respect to the control law translating the pilot’s commands to effector actuator movements, the future of eVTOL and UAM will involve simplified vehicle operations or as defined previously, SVO. SVO refers to control laws that can make the vehicle easy to fly, provide envelope protection, and reduce the overall training required. If this is the case, it will be important to apply the force and moment envelope methodology to a vehicle using SVO to investigate if limits to control power could negatively affect a pilot's ability to recover from an upset in attitude. In future phases, research exploring the intersection between over-actuated flight control, control allocation, control requirements analysis, and flight control design will be used to create methods for predicting the force and moment envelopes of generic configurations.

6 Performance of mission statement tasks

6.1 Mission statement

Flight quality assessments of hardware-validated simulations are used to evaluate an MTE approach to inform specific vehicle certification testing. In Phase 1 of this research, the simulation focused on the case of a quadcopter MTE transitioning from hover to forward flight with a rotor failure in three different cases (constant pitch, collective-only, and collective and cyclic). Future phases may expand on this to include other cases of interest, such as octocopters or partial power failures, using hardware-validated simulations of units and vehicles.

6.2 Handling qualities prediction

This section introduces the terms used for ACAH and RCAH responses as mentioned in Section 5.1. Using the linearized model of the vehicle at EFRC, the ACAH and RCAH pitch responses (which are consistent with roll responses due to symmetry) are shown with and without input delay (Gandhi, 2016). Figure 147 (United States Army, 2000) presents phase bandwidth, gain bandwidth, and phase delay definitions that are important elements of the ADS-33 level criteria approach, which uses Bode diagrams. Specifically, the 180° phase reference/neutral stability (ω_{180}) is a crucial element because it represents a potential stability boundary for closed-loop tracking control by the pilot. According to ADS33, there are two bandwidth specifications: Phase and Gain Bandwidth. The bandwidth portion of the criteria describes the frequency at which the effectiveness of the pilot's control is evaluated within the system's neutral stability.

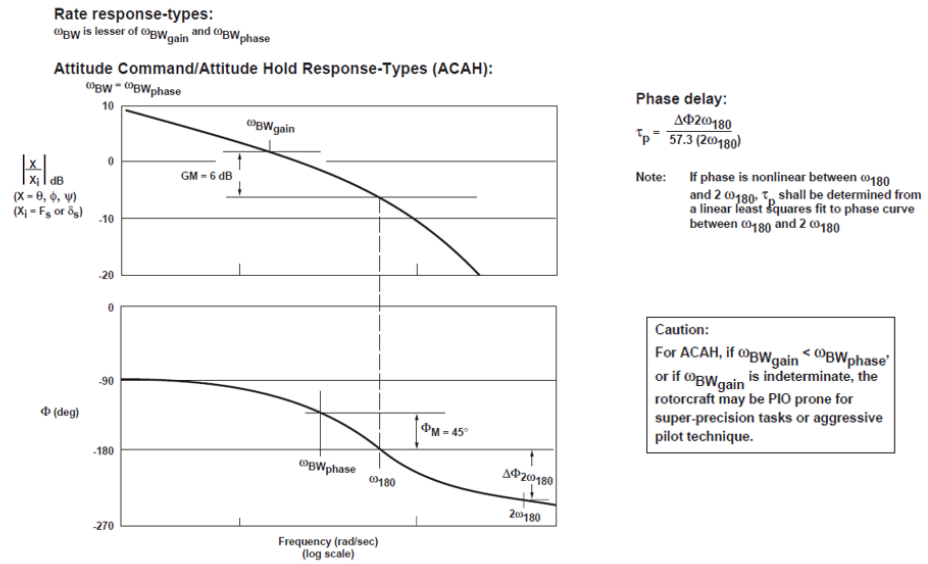

Figure 147. Definitions of bandwidth and phase delay

The Phase Bandwidth ($\omega_{\mathrm{BW_{phase}}}$) is the frequency at which the phase angle is equal to -135 degrees. The Gain Bandwidth ($\omega_{\mathrm{BW_{gain}}}$) is the frequency which is 6 dB higher than the gain value of the phase crossover frequency (ω_{180}). The Bandwidth (ω_{BW}) is defined as the lesser of two frequencies, the phase-limited or gain-limited bandwidth, derived from the frequency response Bode Plot, for rate response types. For attitude response types, the bandwidth is defined as $\omega_{\mathrm{BW_{phase}}}$. Time delays have no effect on the system's gain response, but they have a linear effect as a phase shift/delay on the system. The rate at which the higher frequency phase drop occurs is determined by "$2\omega_{180}$", and the phase delay at that frequency is calculated by the ratio of this phase drop to the frequency of the drop in degrees. If the phase is nonlinear in this region, the phase delay can be determined from a linear least-squares curve fit.

$$\tau_p = \frac{\Delta\Phi_{2\omega_{180}}}{57.3\ (2\omega_{180})} \tag{6}$$

The phase delay of a system is a measure of the equivalent time delay of the system, which describes how quickly the phase drops after the system reaches neutral stability. This aspect of the criteria is important for evaluating the handling qualities of the pitch axis/target acquisition and tracking system, as shown in Figure 148 (United States Army, 2000). The system bandwidth and phase delay findings can be used to assess the performance of the pitch axis in terms of target acquisition and tracking

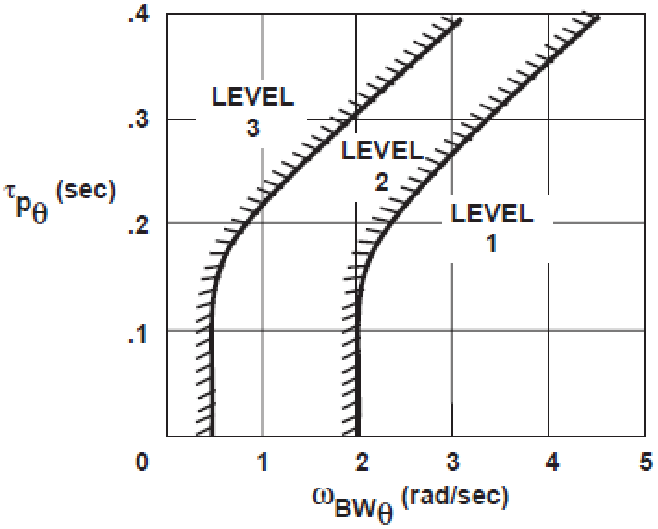

Figure 148. Level of handling qualities for pitch axis

The phase and gain margins are important elements of the frequency analysis that can be found in Bode diagrams. The phase margin measures the amount of phase variation needed at the gain crossover frequency to lose stability, while the gain margin measures the relative gain variation needed at the same frequency to lose stability. These two measures provide an estimate of the stability margin for closed-loop systems. If a closed-loop system is stable, both the gain margin and the phase margin must be positive. Figure 149 shows the graphical representation of stable and unstable systems in terms of phase and gain margins. The elevator input to pitch output Bode plot in this case indicates that the system is unstable. It is important to note that the stability margins play a crucial role in determining the handling qualities of the pitch axis and target acquisition and tracking system.

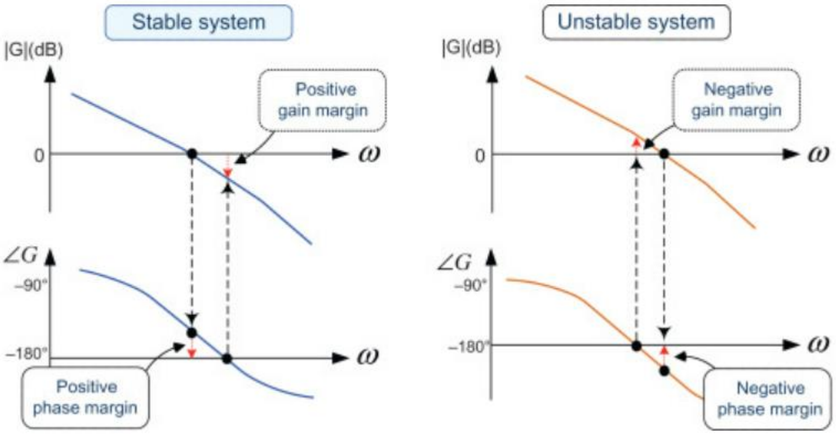

Figure 149. Stable-unstable systems Bode diagrams

The Bode plot of an unstable system can provide valuable information when used in conjunction with a controller designed to stabilize the closed-loop system (Kumar, 2008). This plot can be used to infer important details about the system's stability and performance.

In this study, the pitch axis of a quadcopter was analyzed using a linear model. The response of the vehicle was evaluated using two control methods: rate command/attitude hold (RCAH) and attitude command/attitude hold (ACAH). An optimized PI controller was used to stabilize the linear model for both control methods. The necessary rules for finding bandwidth and phase delay parameters were also applied. Both RCAH and ACAH responses were analyzed with and without a 100ms time delay to meet the requirements of the ADS-33 approach. It should be noted that the symmetrical geometry of the quadcopter means that the same conclusions can be drawn for the roll axis, which represents the longitudinal dynamics of the vehicle RCAH response of lateral dynamics – pitch axis (Gandhi, 2016)

One axis model (see Figure 150 for RCAH closed loop model for pitch axis used in this section) taken from the linearized given model is

$$\dot{\mathrm{q}} = -6.76\, q - 7.58\, \delta_{pitch} \tag{7}$$

where the pitch rate model transfer function is obtained as

$$\dot{\mathrm{q}} = -6.76\, q - 7.58\, \delta_{pitch} \tag{8}$$

$$G(s) = \frac{q}{\delta_{pitch}} = \frac{-7.58}{s + 6.76} \tag{9}$$

In addition, the inner loop controller transfer function given by

$$C_i(s) = \frac{Kp_i s + Ki_i}{s} \tag{10}$$

is used to find the inner loop closed loop system transfer function that is

$$C(s) = \frac{G(s)C_i(s)}{1 + G(s)C_i(s)} \tag{11}$$

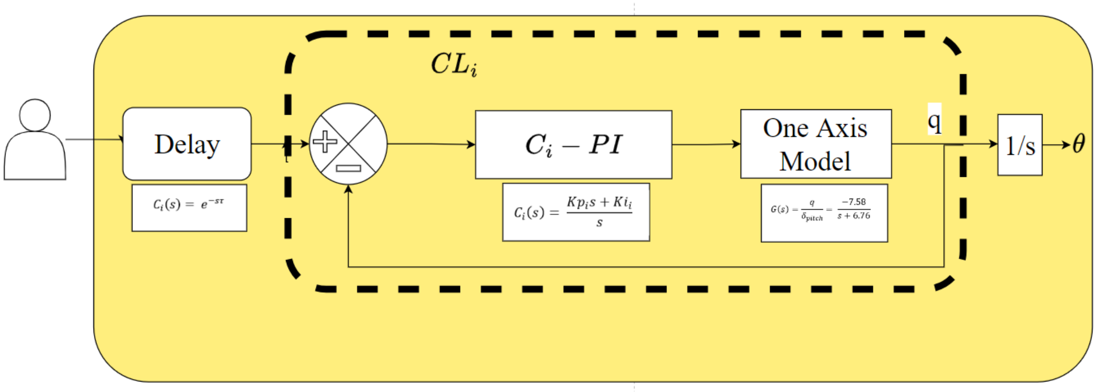

Figure 150. RCAH closed loop model for pitch axis

Figure 151 shows the Bode plot for the RCAH response with no time delay. A PI controller was used to stabilize the linear model, with coefficients ($K_p = -0.3 \ and \ K_i = -22$). These coefficients were optimized using the MATLAB (*pid_tuner*) function. In the bode plot, the gain bandwidth frequency is lower than the phase bandwidth frequency, and the system bandwidth is therefore 6.21 rad/s. The Phase Bandwidth is 9.92 rad/s, and the Gain Bandwidth is 6.21 rad/s. The phase delay can be calculated using the ADS-33 formula from section 6.1, as follows.

$$\tau_p = \frac{226 - 180}{57.3\ (27.6)} = 0.02s \qquad 12$$

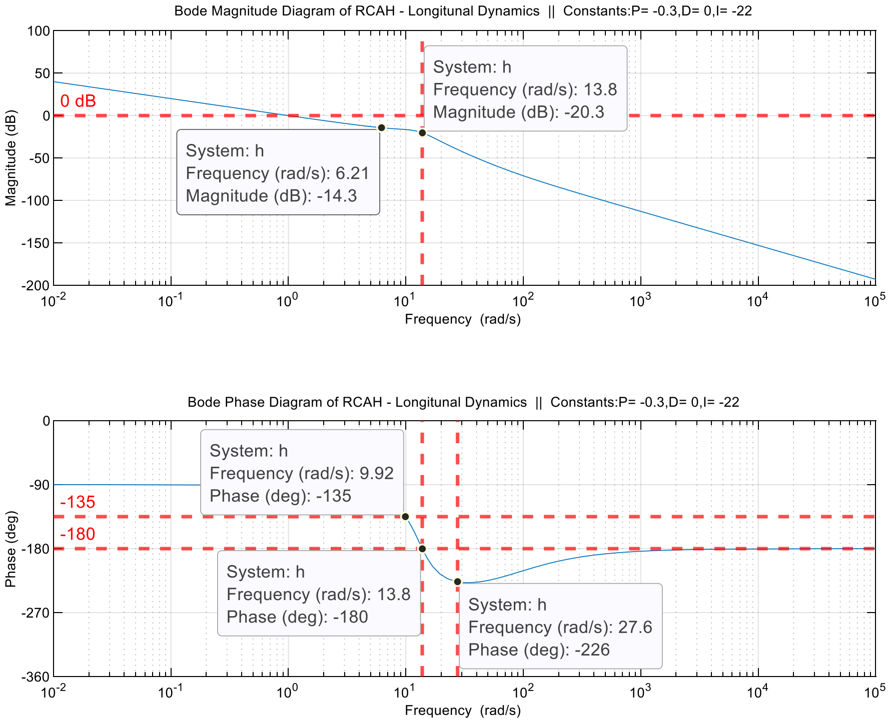

Figure 151. RCAH – Bode plot with no time-delay case

The results of the analysis of the pitch axis-lateral dynamics using a linear model show that the system is stable with positive phase and gain margins. The gain margin is 20.25 dB, and the phase margin is 87.6 rad/s. These values correspond to Level 1 Handling Qualities, as defined by the ADS-33 criteria. This indicates that the system has good stability and control performance and is suitable for use in aircraft applications.

Figure 152 the RCAH response with a 100ms time delay is shown. The same coefficients $(K_p = -0.3\ and\ K_i = -22)$ were used to stabilize the given model, but with the addition of a 100ms time delay. For rate response types, the bandwidth is defined as the lower of the two frequencies: the phase-limited or gain-limited bandwidth. As can be seen in the bode plot, the gain-limited bandwidth frequency is lower than the phase-limited bandwidth frequency, so the system bandwidth is taken as the frequency that is 6 dB higher than the gain value at the phase crossover frequency (ω_{180}). The Phase Bandwidth ($\omega_{\mathrm{BW}_{\mathrm{phase}}}$) is 5.28 rad/s, the Gain Bandwidth ($\omega_{\mathrm{BW}_{\mathrm{gain}}}$) is 3.36 rad/s, and the Calculated Bandwidth is 3.36 rad/s. The phase delay is calculated as 0.12s. Both margin values are positive, indicating that the system is stable with these phase and gain margins. The Gain Margin is 16.08 dB, and the Phase Margin is 81.89 rad/s. It is worth noting that, as expected, the addition of input delay to the system results in smaller gain and phase margins, corresponding to a more fragile response. The calculated bandwidth and phase delay correspond to Level 1 Handling Qualities as shown in Figure 148.

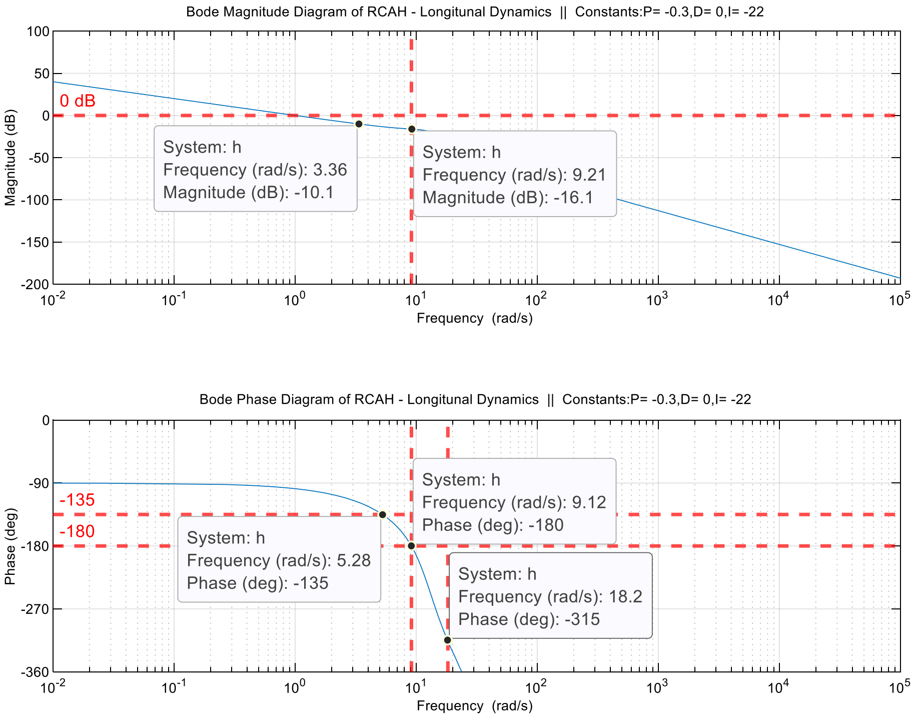

Figure 152. RCAH – Bode plot with 100ms delay case

6.2.1 ACAH response of lateral dynamics – pitch axis

The one-axis model used in the RCAH response was utilized for the ACAH response. This model includes the pitch rate ($\dot{q}$) dynamics, which were derived from the linearized vehicle dynamics. Figure 153 shows the closed-loop model for the pitch axis used in this section for the ACAH response.

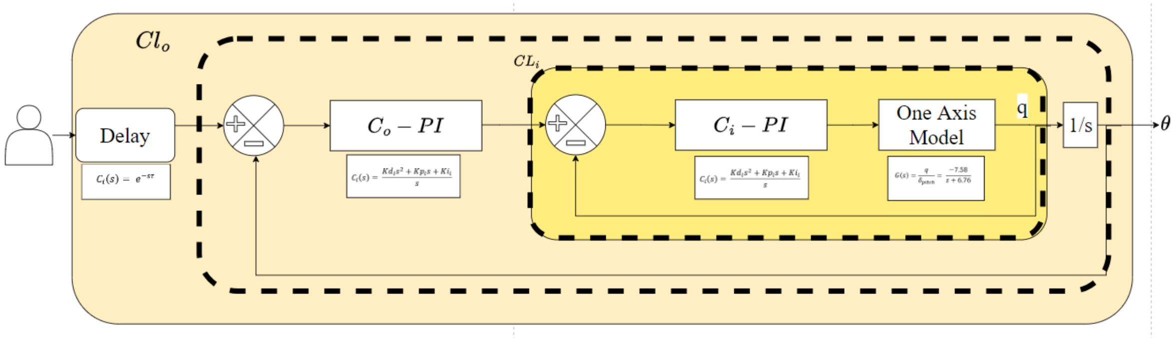

Figure 153. ACAH closed loop model for pitch axis

In addition to the inner loop controller, an outer loop-controller transfer function was added:

$$C_o(s) = \frac{Kp_o s + Ki_o}{s} \tag{13}$$

where it yields an outer loop closed loop system transfer function given by

$$Cl_o(s) = \frac{C_o(s)Cl_i(s)\frac{1}{s}}{1 + C_o(s)Cl_i(s)\frac{1}{s}} \tag{14}$$

In Figure 154, the bode plot for the ACAH response with no time delay is shown. The inner loop of the ACAH response was stabilized using an optimized PI controller with coefficients $K_p = 0.8 \ and \ K_i = 0.4$. For attitude response types, the bandwidth is defined as the frequency at which the phase angle equals -135 degrees. The Phase Bandwidth is 10.1 rad/s and the Gain Bandwidth is 7.6 rad/s, resulting in a calculated Bandwidth of 10.1 rad/s. According to ADS-33, if the gain bandwidth is less than the phase bandwidth or undefined, the rotorcraft may experience Pilot Induced Oscillations (PIO) and a flight test should be conducted to determine acceptability. The phase difference can be approximately calculated using the formula provided by ADS-33, resulting in a calculated Phase Delay of 0.03 s. Both the Gain Margin and Phase Margin are positive, indicating that the system is stable with these margins. The Gain Margin is

21.16 dB and the Phase Margin is 118.97 rad/s, corresponding to Level 1 Handling Qualities (as shown in Figure 139).

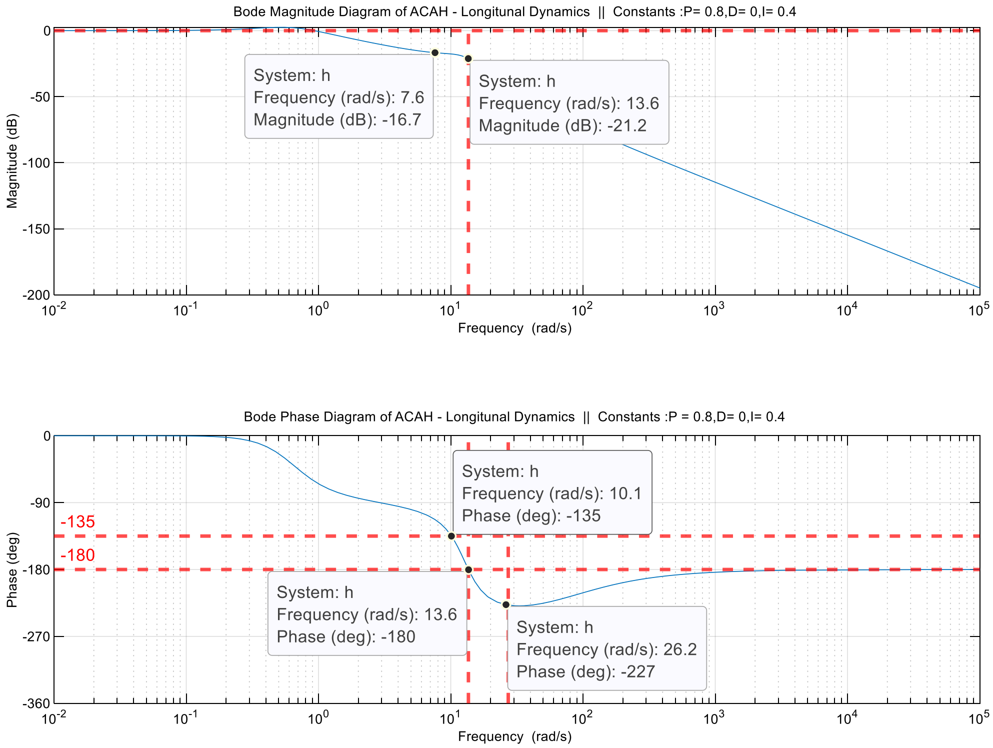

Figure 154. ACAH – Bode plot with no time-delay case

In Figure 155 the ACAH response with a 100ms delay is shown in the bode plot. The same coefficients ($K_p = 0.8\ and\ K_i = 0.4$) were used as in the previous ACAH response with a 100ms time delay. For attitude response types, the bandwidth is defined as the frequency at which the phase angle is equal to -135 degrees, resulting in a phase bandwidth of 5.69 rad/s. The gain bandwidth is 3.29 rad/s, and the calculated bandwidth is 5.69 rad/s. Since the gain bandwidth is less than the phase bandwidth, the rotorcraft may experience Pilot-Induced Oscillation (PIO). In this case, flight tests should be conducted to determine acceptability. The phase delay can be calculated approximately using the formula given by ADS-33, resulting in a calculated phase delay of 0.13s. Both the gain margin and phase margin are positive, indicating that the system is stable with these values. The gain margin is 17.3 dB and the phase margin is 113.66 rad/s. It is important to note that, as expected, when an input delay is added to the system, both the gain and phase margins yield smaller values, corresponding to a more fragile response. The calculated bandwidth and phase delay correspond to Level 1 Handling Qualities, as shown in Figure 148.

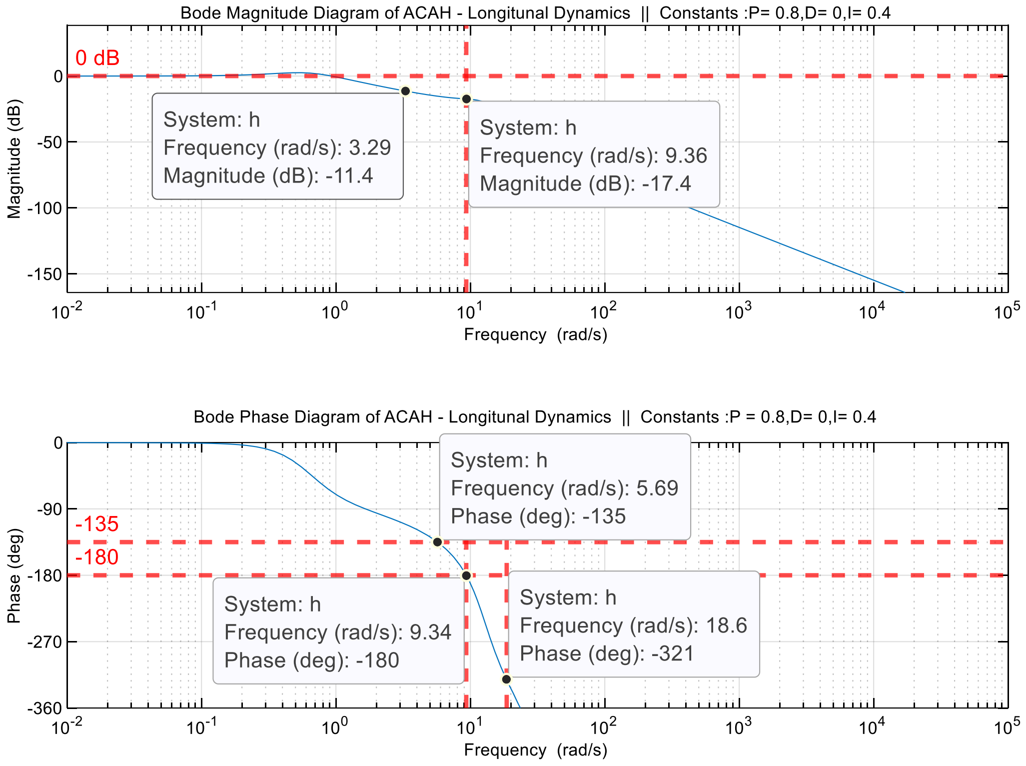

Figure 155. ACAH – Bode plot with 100ms delay case

6.3 Trajectory following

6.3.1 Nonlinear simulation of control requirements

A nonlinear simulation model of a generic coaxial multi-rotor vehicle with 6 degrees of freedom has been developed. The aim of the simulation is to generate flight trajectories that represent typical mission task elements (MTEs) in order to evaluate the resulting control requirements. These flight trajectories are created by defining a reference flight trajectory and using a nonlinear dynamic inversion (NLDI) controller to make the vehicle follow the reference trajectory. The NLDI controller is implemented using accurate data about the vehicle's parameters and states (e.g., noise-free sensor data), so it can be considered an ideal control law that represents the maneuvering capabilities of the vehicle under idealized conditions. It is worth noting that while a version of the simulation has been developed that includes rotor dynamics, the simulation results in this section assume that the commanded forces and moments generated by the NLDI controller are implemented directly by the control system. This was done to focus on control requirements that are independent of rotor type (e.g., fixed pitch, collective pitch, or collective and cyclic pitch) or any specific control allocation.

6.3.2 Vehicle simulation model

The vehicle simulation was developed in the MATLAB / Simulink environment. The simulation model consists of various subsystems, including a block for multi-rotor vehicle dynamics and a block for guidance and control, which incorporates the NLDI controller. The simulation generates output data for the inertial position (north-east-down), body-referenced inertial velocity components, body-referenced angular rates, and attitude (roll, pitch, and heading) of the vehicle. Additionally, the simulation produces output data for other relevant variables, including the required control forces and moments. Table 10 shows the mass and inertia properties of the simulated multi-rotor vehicle.

Table 10. Vehicle mass and inertia parameters

Parameter	**Symbol**	**Value**	**Units**
Weight	*W*	75	lb
Mass	*m*	2.329	slug
Moment of Inertia about the X-axis	*Ixx*	4.548	slug-ft2
Moment of Inertia about the Y-axis	*Iyy*	4.548	slug-ft2
Moment of Inertia about the Z-axis	*Izz*	6.772	slug-ft2
Product of Inertia – XY	*Ixy*	0	slug-ft2
Product of Inertia – XZ	*Ixz*	0	slug-ft2
Product of Inertia – YZ	*Iyz*	0	slug-ft2

The dynamics model assumes that the vehicle behaves as a rigid body, resulting in a set of 12 nonlinear, time-invariant equations of motion that can be expressed in state-space form:

$$\underline{\dot{X}}(t) = \underline{F}\left(\underline{X}(t), \underline{U}(t)\right) \tag{15}$$

The state vector is defined as:

$$\underline{X} = (u, v, w, p, q, r, \phi, \theta, \Psi, x, y, h)^T \tag{16}$$

Where (u, v, w) denote the body-referenced translational velocity components, (p, q, r) represent the body-referenced angular velocity components, (ϕ, θ, Ψ) are the roll, pitch, and yaw (heading) angles, and (x, y, h) denote the inertial position in distance North, distance East, and altitude respectively. The control inputs depend on the type of rotor system used, such as fixed pitch, collective pitch, or collective and cyclic pitch. For example, in the case of a quadcopter with fixed pitch, the controls would correspond to the thrust commanded to each of the four rotor units.

The individual equations of motion are numerically integrated to determine the state variables at every simulation time step. The translational equations of motion take the form:

$$\dot{u} = rv - qw - gsin\theta + \frac{1}{m}\left(T_x^B + F_{x,areo}^B\right) \tag{17}$$

$$\dot{v} = -ru + pw + gsin\phi cos\theta + \frac{1}{m}\left(T_y^B + F_{y,areo}^B\right) \tag{18}$$

$$\dot{w} = qu - pv + gcos\phi cos\theta + \frac{1}{m}\left(T_z^B + F_{z,areo}^B\right) \tag{19}$$

$\left(T_x^B, T_y^B, T_z^B\right)$ represent the components of total thrust generated by the control system, expressed in the vehicle body frame. Similarly, $\left(F_{x,aero}^B, F_{y,aero}^B, F_{z,aero}^B\right)$ corresponds to the components of the aerodynamic force in the body frame.

In this work, the aerodynamic force was modeled as a drag force acting at the CG in the direction of the relative wind at the CG. The vehicle drag force is given by

$$D = \frac{1}{2}\rho V_a^2 C_d S \tag{20}$$

where ρ is the sea-level air density, $C_D S$ represents an estimated flat-plate area for this notional multi-rotor vehicle, and V_a is the total airspeed, given as the magnitude of the difference between the inertial velocity vector $\underline{V}_{cm}^B$ and the wind velocity vector $\underline{V}_W^B$. The wind velocity vector corresponds to a user-specified steady-state wind vector, which was set to zero in these simulations. The drag force *D*, which acts in the direction of the relative wind, is then expressed in the body frame as follows:

$$F_{x,areo}^B = -D\ cos\alpha\ sin\beta \tag{21}$$

$$F_{y,areo}^B = -Dsin \tag{22}$$

$$F_{z,areo}^B = -D\ sin\alpha\ cos\beta \tag{23}$$

Where α and β are the angle of attack and sideslip angles.

The rotational equations of motion, which are obtained by summing external moments about the CG, and equating them to the rate of change of angular momentum, take the form:

$$\dot{p} = \frac{1}{I_{xx}} M_x^B + \frac{1}{I_{xx}}\left(I_{yy} - I_{zz}\right)qr \tag{24}$$

$$\dot{q} = \frac{1}{I_{yy}} M_y^B - \frac{1}{I_{yy}} (I_{xx} - I_{zz}) pr \qquad 25$$

$$\dot{r} = \frac{1}{I_{zz}} M_z^B + \frac{1}{I_{zz}} \left(I_{xx} - I_{yy}\right) pq \qquad 26$$

These equations are simplified due to symmetry, which renders the products of inertia zero. $\left(M_x^B, M_y^B, M_z^B\right)$ represent the control moments, resolved into components about each of the body axes. Given that the aerodynamics model only includes a drag force at the CG, and there are no pure aerodynamic moments, no aerodynamic moments are acting about the CG.

The attitude kinematic equations, which are derived by relating the Euler angle rates to the body-referenced angular rates, are given by

$$\dot{\phi} = p + q \sin\phi \tan\theta + r \cos\phi \tan\theta \qquad 27$$

$$\dot{\theta} = q \cos\phi - r \sin\phi \qquad 28$$

$$\dot{\psi} = q \sin\phi \sec\theta + r \cos\phi \sec\theta \qquad 29$$

Finally, the inertial position kinematic equations, which are derived by transforming the body-referenced inertial velocity components into the inertial north-east-down (NED) frame and integrating them, are given by

$$\begin{bmatrix} \dot{x} \\ \dot{y} \\ \dot{z} \end{bmatrix} = \begin{bmatrix} V_N \\ V_E \\ V_D \end{bmatrix} = R_B^E \begin{bmatrix} u \\ v \\ w \end{bmatrix} \qquad 30$$

where $R_B^E = (R_E^B)^T$, the transpose of the Direction Cosine Matrix (DCM) that relates the inertial axes to the body-fixed axes. The DCM is derived in terms of the roll, pitch, and yaw Euler angles as follows:

$$R_E^B = \begin{bmatrix} 1 & 0 & 0 \\ 0 & \cos\phi & \sin\phi \\ 0 & -\sin\phi & \cos\phi \end{bmatrix} \begin{bmatrix} \cos\theta & 0 & -\sin\theta \\ 0 & 1 & 0 \\ \sin\theta & 0 & \cos\theta \end{bmatrix} \begin{bmatrix} \cos\psi & \sin\psi & 0 \\ -\sin\psi & \cos\psi & 0 \\ 0 & 0 & 1 \end{bmatrix} \qquad 31$$

The position kinematic equations are integrated to compute the inertial (NED) position of the vehicle at each simulation time step. Note that the z-axis is in the inertial down direction, Z_D, but for the purpose of clarity in presentation, the simulation outputs the altitude $h = -Z_D$.

6.3.3 Guidance and control system

The vehicle simulation is designed to simulate user-defined or pre-loaded flight trajectories. The reference trajectory is defined in terms of time histories of the inertial (NED) velocity$\left(V_{N,ref}, V_{E,ref}, V_{D,ref}\right)$. The reference velocity can be defined at any sampling rate and the vehicle is assumed to travel at a constant heading in the downrange direction. The reference data is generated at a simulation sample rate of 1000 Hz for the control system to track and achieve the desired reference inertial position history.

A control system based on nonlinear dynamic inversion (NLDI), also known as feedback linearization, is implemented to enable the vehicle to track the reference trajectories. NLDI is based on the principle that the control input can be used to cancel the inherent nonlinear dynamics of the system and track desired reference trajectories while imposing desirable linear dynamics. The NLDI control laws used in the vehicle simulation are implemented in an outer and inner loop structure. The outer loop represents slower, translational dynamics required to track the reference trajectory, while the inner loop represents faster dynamics associated with stabilizing the attitude of the vehicle. Previous work by the ERAU team has demonstrated the effectiveness of this implementation in simulating multi-rotor systems.

The outer loop first generates inertial (NED) velocity commands using a PID controller based on the NED position error, which is simply the difference between the reference position and the vehicle position, as would be given by the onboard INS:

$$v_{x,com} = K_{P,x}\left(x_{ref} - x\right) + K_{I,x}\int_0^t \left(x_{ref} - x\right)d\tau + K_{D,x}\frac{d}{dt}\left(x_{ref} - x\right) \tag{32}$$

$$v_{y,com} = K_{P,y}\left(y_{ref} - y\right) + K_{I,y}\int_0^t \left(y_{ref} - y\right)d\tau + K_{D,y}\frac{d}{dt}\left(y_{ref} - y\right) \tag{33}$$

$$v_{z,com} = K_{P,z}\left(z_{ref} - z\right) + K_{I,z}\int_0^t \left(z_{ref} - z\right)d\tau + K_{D,z}\frac{d}{dt}\left(z_{ref} - z\right) \tag{34}$$

Inertial acceleration commands are then computed based on the difference between the commanded inertial velocity and the vehicle inertial velocity:

$$a_{x,com} = K_{P,vx}\left(v_{x,com} - v_x\right) + K_{I,vx}\int_0^t \left(v_{x,com} - v_x\right)d\tau + K_{D,vx}\frac{d}{dt}\left(v_{x,com} - v_x\right) \tag{35}$$

$$a_{y,com} = K_{P,vy}\left(v_{y,com} - v_y\right) + K_{I,vy}\int_0^t \left(v_{y,com} - v_y\right)d\tau + K_{D,vy}\frac{d}{dt}\left(v_{y,com} - v_y\right) \tag{36}$$

$$a_{z,com} = K_{P,vz}\left(v_{z,com} - v_z\right) + K_{I,vz}\int_0^t \left(v_{z,com} - v_z\right)d\tau + K_{D,vz}\frac{d}{dt}\left(v_{z,com} - v_z\right) \tag{37}$$

Roll, pitch, and vertical force commands are then generated as follows:

$$\phi_{com} = sin^{-1}\left(\frac{m\left(a_{x,com}\,sin\,\psi - a_{y,com}\,cos\,\psi\right)}{F_{z,com}}\right) \tag{38}$$

$$\theta_{com} = sin^{-1}\left(\frac{m\left(a_{x,com}\,cos\,\psi + a_{y,com}\,sin\,\psi\right)}{F_{z,com}\,cos\,\phi}\right) \tag{39}$$

$$F_{z,com} = \frac{m\left(a_{z,com} - g\right)}{cos\,\phi\,cos\,\theta} \tag{40}$$

The commanded roll and pitch angles serve as inputs to the inner loop, which are then used to generate commanded angular rates. The commanded Euler angle rates are computed using PID controllers operating on the Euler angle errors:

$$\dot{\phi}_{com} = K_{P,\phi}(\phi_{com} - \phi) + K_{I,\phi}\int_0^t (\phi_{com} - \phi)d\tau + K_{D,\phi}\frac{d}{dt}(\phi_{com} - \phi) \tag{41}$$

$$\dot{\theta}_{com} = K_{P,\theta}(\theta_{com} - \theta) + K_{I,\theta}\int_0^t (\theta_{com} - \theta)d\tau + K_{D,\theta}\frac{d}{dt}(\theta_{com} - \theta) \tag{42}$$

$$\dot{\psi}_{com} = K_{P,\psi}(\psi_{com} - \psi) + K_{I,\psi}\int_0^t (\psi_{com} - \psi)d\tau + K_{D,\psi}\frac{d}{dt}(\psi_{com} - \psi) \tag{43}$$

The commanded Euler rates are then converted to commanded body-referenced angular rates:

$$p_{com} = -\dot{\psi}_{com}\,sin\,\theta + \dot{\phi}_{com} \tag{44}$$

$$q_{com} = \dot{\psi}_{com}\,sin\,\phi\,cos\,\theta + \dot{\theta}_{com}\,cos\,\phi \tag{45}$$

$$r_{com} = \dot{\psi}_{com}\,cos\,\phi\,cos\,\theta - \dot{\theta}_{com}\,sin\,\phi \tag{46}$$

Commanded moments about the body axes are then generated from the commanded angular rates using the moment equation:

$$\underline{M}^B_{com} = \underline{\omega}^B \times I^B_{cm}\underline{\omega}^B + \dot{\underline{\omega}}_{com} \tag{47}$$

where $\dot{\underline{\omega}}_{com} = [\dot{p}_{com} \quad \dot{q}_{com} \quad \dot{r}_{com}]^T$ are commanded body-referenced angular accelerations:

$$\dot{p}_{com} = K_{P,p}(p_{com} - p) + K_{I,p}\int_0^t (p_{com} - p)d\tau + \frac{d}{dt}(p_{com}) \tag{48}$$

$$\dot{q}_{com} = K_{P,q}(q_{com} - q) + K_{I,q}\int_0^t (q_{com} - q)d\tau + \frac{d}{dt}(q_{com}) \tag{49}$$

$$\dot{r}_{com} = K_{P,r}(r_{com} - r) + K_{I,r}\int_0^t (r_{com} - r)d\tau + \frac{d}{dt}(r_{com}) \tag{50}$$

The objective of this simulation study was to determine the required control forces and moments, independent of rotor configuration or control allocation. In practice, these commanded forces and moments would be translated into appropriate control commands for the rotors. The NLDI control law was tuned by adjusting the various PID controller gains to represent an ideal control system with a fast response for tracking the reference trajectories, which approximates the best-case performance of a physical flight control system.

6.3.4 Simulation results

Simulations were performed for two representative multi-rotor trajectories. In the first case, the vehicle starts at hover and accelerates downrange at a constant altitude, then flies at a constant velocity, and finally decelerates back to zero forward velocity at the same altitude. This case is meant to replicate the experimental setup at the EFRC corresponding to the vehicle testbed constrained to a zipline. The second case corresponds to the vehicle starting on the ground and then climbing to a forward flight condition at a constant altitude. In both cases, varying acceleration was used to generate reference trajectories.

6.3.4.1 Case 1: Acceleration from hover at constant altitude

In this simulation case, the vehicle is initially hovering and then accelerates at a constant altitude over a downrange distance of 120 feet, follows by 20 feet of flying at a constant velocity. Then, the vehicle decelerates at a constant altitude for an additional 120 feet downrange until it reaches a zero-velocity condition. These distances were chosen to replicate the experimental zipline setup at the EFRC.

Figure 156 to Figure 158 summarize simulation results for this trajectory with accelerations of 2, 5, and 10 ft/s^2. Because the distances were the same in each case, the total flight time decreases with increasing acceleration. Figure 156 presents the time histories of several vehicle states, including the downrange position, forward velocity, pitch rate, and pitch angle. The flight trajectory takes a similar form for each acceleration case, but the magnitudes clearly vary with acceleration. For the largest acceleration of 10 ft/s^2, the vehicle reaches a peak velocity of 50 ft/s and covers the 260 ft total distance in approximately 10 seconds. In contrast, for the smallest acceleration of 2 ft/s^2, the vehicle reaches a maximum velocity of 22 ft/s and travels the full distance in approximately 23 seconds. In each case, the vehicle initially pitches forward in order to accelerate downrange. When the vehicle terminates the acceleration phase, it quickly pitches upward and experiences a transient pitch response. These pitching maneuvers are more aggressive in the 10 ft/s^2 acceleration case, resulting in a pitch angle of approximately -20 deg (nose-down pitch) during the acceleration phase, followed by a rapid transition to 20 deg (nose-up pitch) when the acceleration phase ends. During the deceleration phase, the vehicle settles to a constant upward pitch angle in order to point a component of the thrust vector in the negative downrange direction.

Figure 157 and Figure 158 depict the control requirements for tracking these trajectories with varying acceleration. Figure 157 shows the commanded vertical force from the NLDI controller in the vehicle body frame. Because the simulated vehicle is a quadcopter, thrust can only be applied in the vertical direction. Figure 157 also shows the commanded pitch moment from the controller, which is used to point the vehicle thrust vector in the appropriate inertial direction. For example, a negative (nose-down) pitching moment points a component of the thrust vector forward, resulting in forward acceleration. In each case, the total required force is composed of a vertical inertial component of 75 lbs, corresponding to the weight of the vehicle, in addition to a forward inertial component required to overcome drag and achieve the desired forward acceleration. In the maximum acceleration case of 10 ft/s^2, the required pitch moment from the control system for this maneuver is almost 10 ft-lbs. Figure 158 depicts the required control forces resolved into inertial components (downrange and vertical). Note that this simulation starts in the hovering state, and the inertial vertical force is simply the vehicle weight of 75 lbs, whereas the forward inertial force varies with the vehicle acceleration. In the maximum acceleration case of 10 ft/s^2, the required inertial downrange force reaches a magnitude of approximately 30 – 35 lbs in the positive and negative direction for the acceleration and deceleration phases respectively.

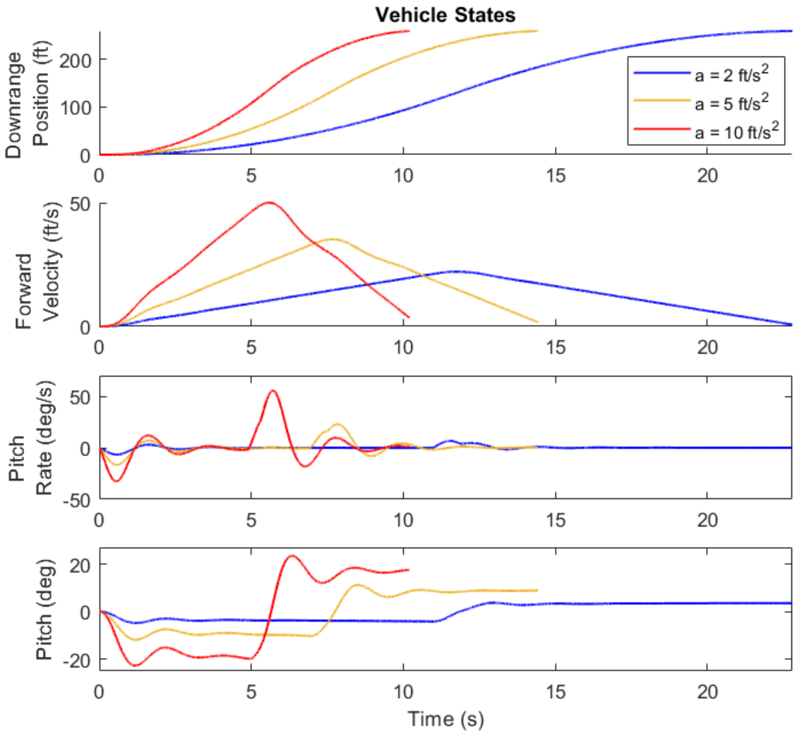

Figure 156.Vehicle states for simulation case 1 with varying acceleration

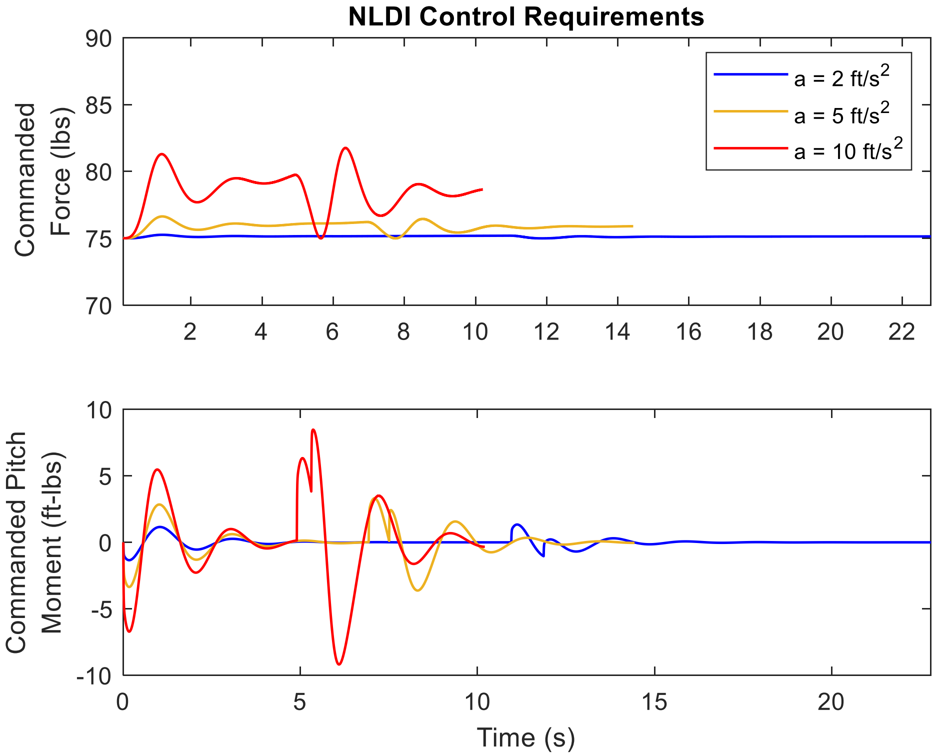

Figure 157. Commanded body-z force and pitch moment for case 1 with varying acceleration

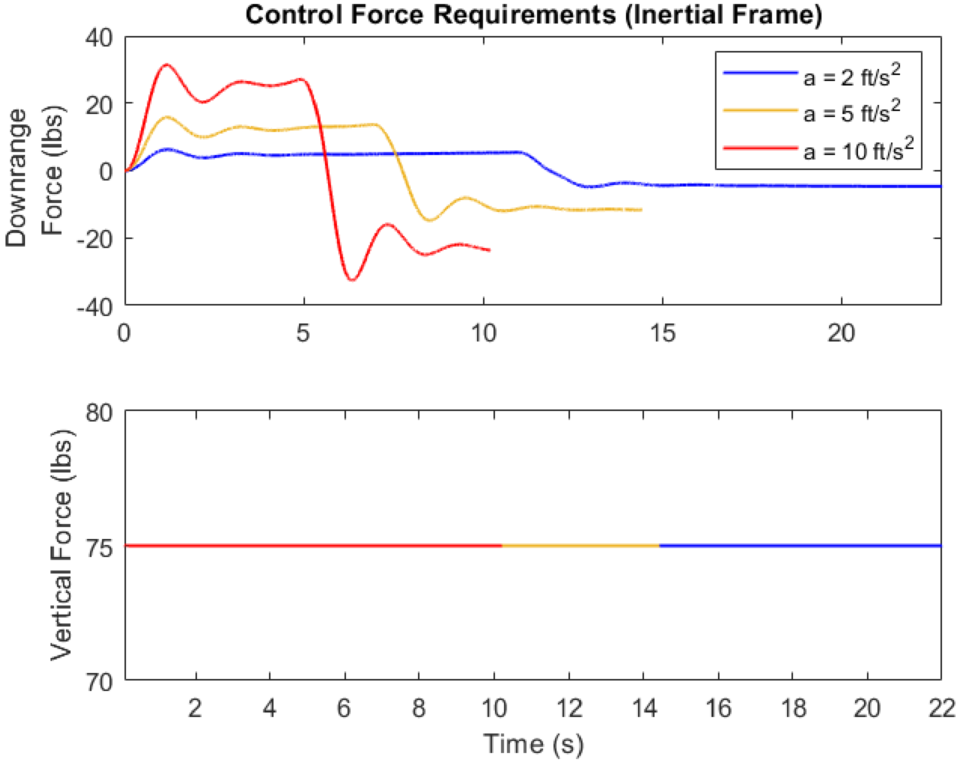

Figure 158. Required inertial control forces for simulation case 1 with varying acceleration

6.3.4.2 Simulation case 2: Climb-out to constant altitude and forward velocity

In this simulation case, the vehicle starts from rest on the ground and then climbs, transitioning to a constant altitude and constant forward velocity condition. This trajectory was simulated for varying acceleration levels of 2, 5, and 10 ft/s^2. In each case, the acceleration is initially set at an angle of 60 deg. from the horizon (i.e., the vehicle takes off with a 60 deg. vertical flight path angle) and is then linearly decreased to zero deg. (horizontal) after 10 seconds. As a result, the vehicle reaches a constant altitude, constant forward velocity condition after 10 seconds.

Figure 159 to Figure 162 summarized simulation results for this trajectory with accelerations of 2, 5, and 10 ft/s^2. Because the climb-out flight phase was set to 10 seconds, the flight trajectories in Figure 159 illustrate that the vehicle reaches a higher steady-state altitude for larger acceleration levels. Similarly, the vehicle states shown in Figure 160 indicates that the vehicle settles to a higher constant forward velocity for larger acceleration. In each case, the vehicle initially pitches forward to accelerate downrange and upward. When the vehicle terminates the acceleration phase, it quickly pitches upward and reaches a steady-state nose-down pitch to overcome drag and maintain constant forward velocity. For example, for the 10 ft/s^2 acceleration case, the pitch angle reaches a maximum of almost -40 deg. (nose-down pitch) during the climb-out phase before settling to a -12 deg. pitch to maintain a constant forward flight velocity of 100 ft/s.

Figure 161 and Figure 162 depict the control requirements for tracking these climb-out trajectories at varying acceleration. Figure 161 shows the commanded vertical force from the NLDI controller in the vehicle body frame and the commanded pitch moment from the controller. In each case, the total required force is composed of the force required to balance the weight and drag of the vehicle in addition to providing the required acceleration. The commanded pitch moment initially is in the negative (nose-down) direction to provide forward acceleration. At the end of the 10-sec. acceleration phase, there is a sharp nose-up pitch moment to reduce the acceleration to zero. In the maximum acceleration case, this pitch moment reaches a magnitude of 20 ft-lbs. Figure 162 depicts the required control forces resolved into inertial components (downrange and vertical). The required inertial vertical force is equal to the vehicle weight plus the required vertical component of acceleration. The required inertial downrange force is equal to the vehicle drag in addition to the required downrange component of acceleration. In the maximum acceleration case, this downrange force reaches a maximum of 40 lbs, and the vertical force reaches a maximum of 90 lbs during the initial climb-out.

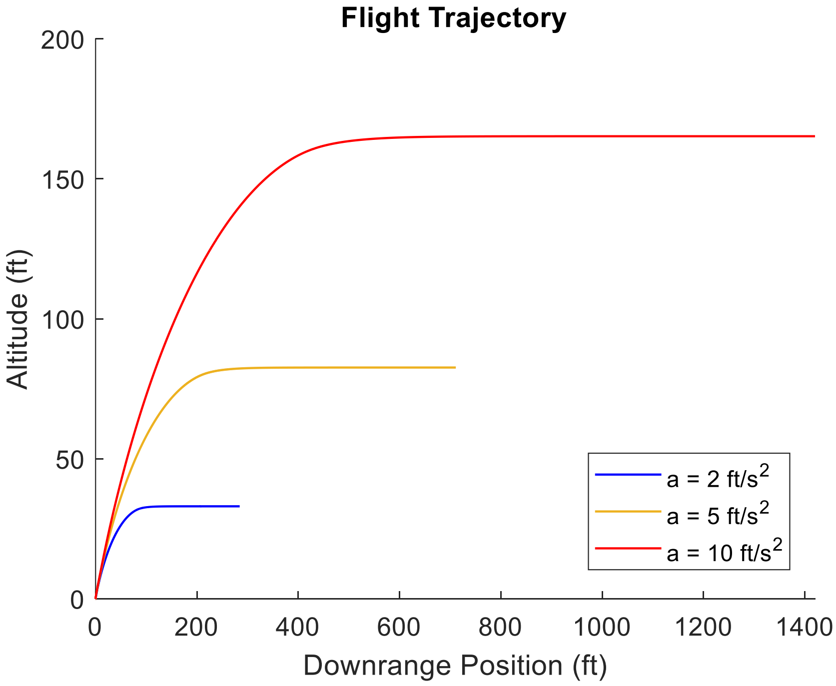

Figure 159. Flight trajectory for simulation case 2 with varying acceleration

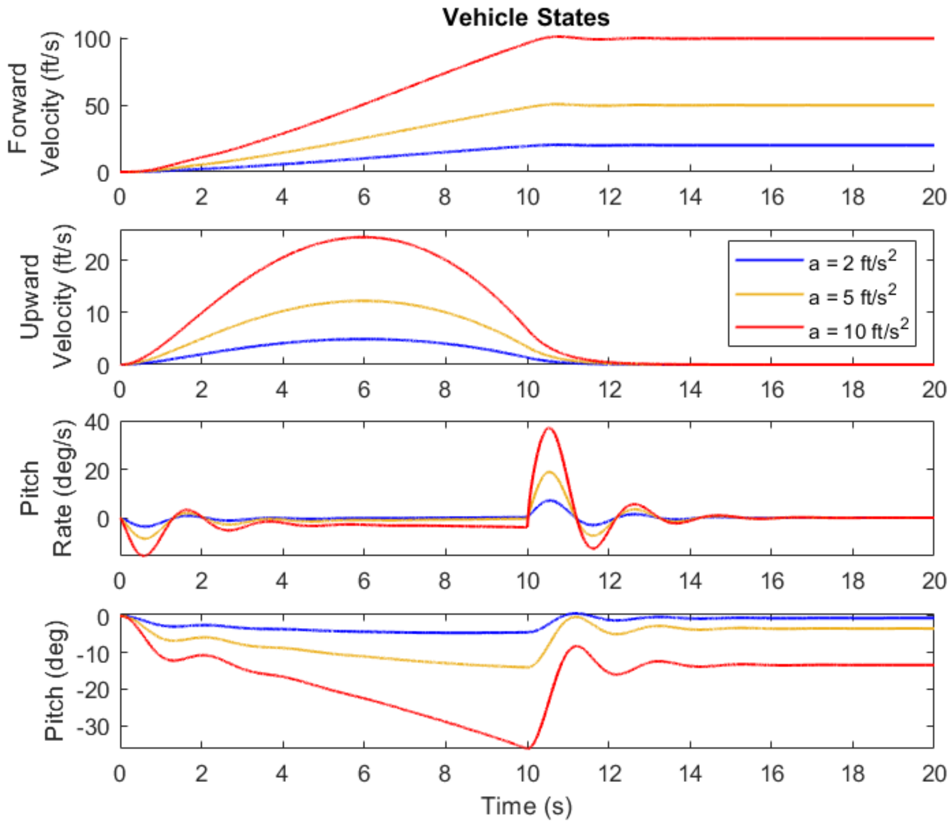

Figure 160. Vehicle states for simulation case 2 with varying acceleration

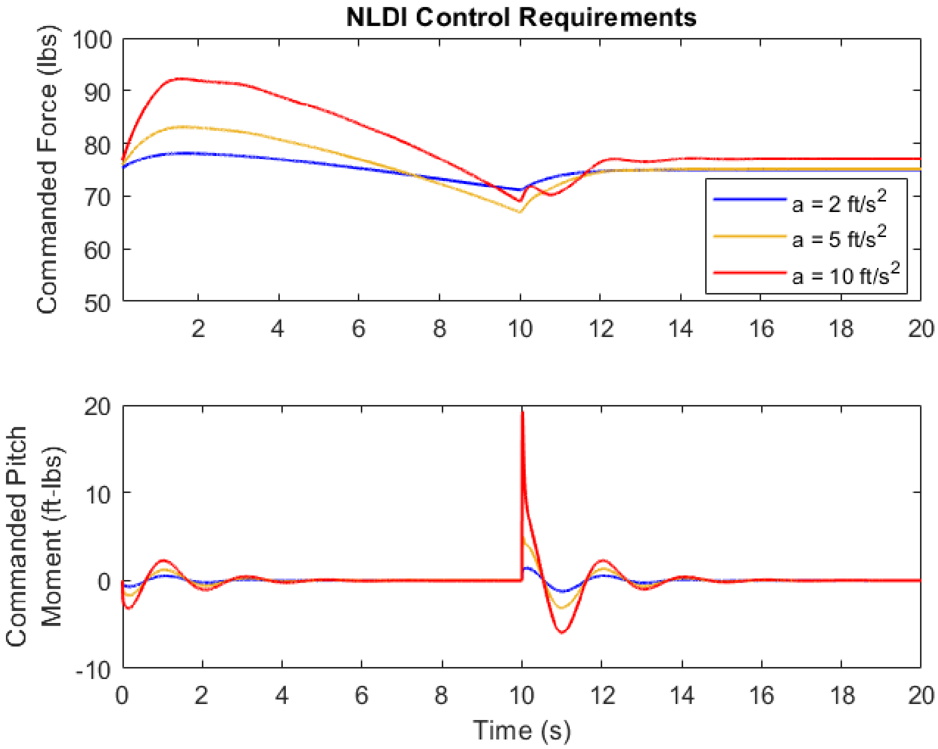

Figure 161. Commanded body-z force and pitch moment for simulation case 2 with varying acceleration

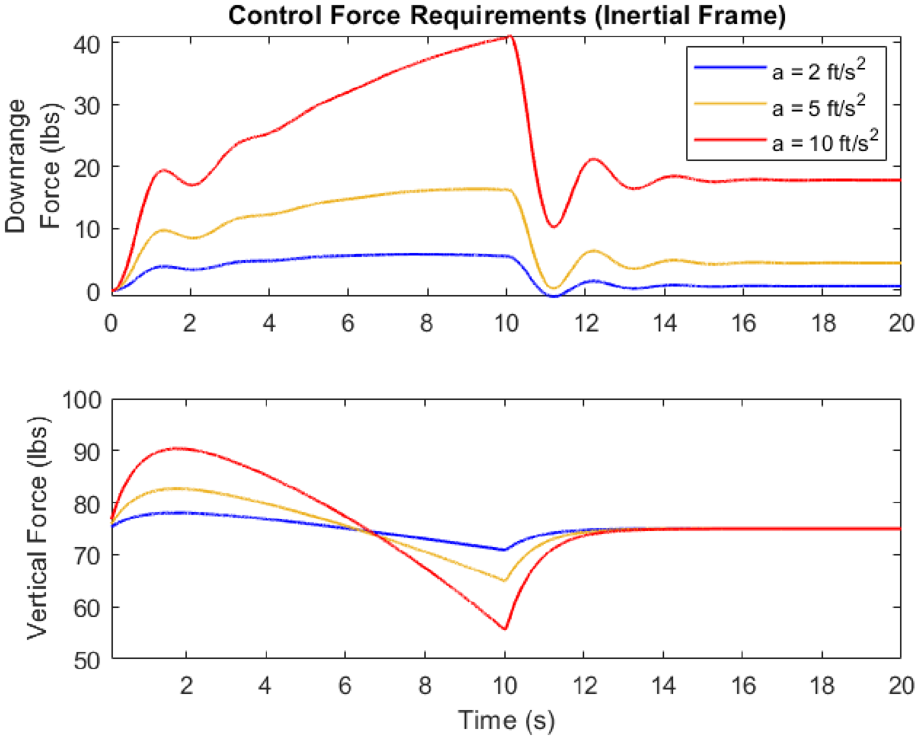

Figure 162. Required inertial control forces for simulation case 2 with varying acceleration

7 Conclusions

Through this research effort the world saw, for the first time, a quadcopter flying with one rotor completely stopped. The goal of this project was to evaluate the performance and scalability of different control methods used by DEP systems. Out of the three control strategies examined, one was found to be superior. That control strategy is not one that is used by UAM manufacturers today. It was discovered that stable flight with one rotor out is made possible only by using cyclic pitch-capable helicopter mechanics, and that the control strategy that is implemented in current UAM vehicles was not able to keep a quadcopter airborne after the failure of one rotor. Simulation and flight-testing revealed that the control response and authority provided by a speed-governed collective and cyclic pitch rotor system is superior to a fixed-pitch, speed-controlled strategy. The PAVER aircraft is built around systems that are fully scalable, and their implementation into UAM vehicles should be advocated. However, these outstanding capabilities do not come without their drawbacks, and the lessons learned during this research can promote safer aircraft designs.

The PAVER quadcopter was built specifically to test three control strategies without any modifications. The three control modes- fixed-pitch RPM control (FP1), speed-governed collective pitch mode (VP1), and speed-governed collective and cyclic pitch mode (VP2), were compared with respect to response time, overall stability, and controllability, in nominal and degraded modes. Simulation and flight test data showed that the common fixed-pitch RPM control strategy (FP1) currently used by UAM manufacturers had the slowest response time and was unable to keep a quadcopter airborne after the loss of one rotor. The VP1 control strategy used in this study provided 42.8% faster response time in roll and pitch maneuvers, and notably had 54% faster response in yaw control than the standard RPM-based control mode. However, the implementation of cyclic pitch to the VP1 mode to control yaw (VP2 mode) improved response time by an additional 20%, which provided an overall 65.7% improvement in yaw control response time than the standard RPM-based control mode. Cyclic pitch control added so much yaw authority that flight with one rotor completely disabled was made possible while requiring minimal pilot effort to maintain stable hover.

From a control system standpoint, understanding the gyroscopic precession of the rotor was crucial when implementing cyclic pitch control to a multirotor vehicle. In the case of a quadrotor, two pairs of counter=rotating rotors are fixed to a single rigid airframe. To properly deflect the swashplate of each rotor for cyclic control, the precession of the rotor (i.e. flap frequency) had to be well understood and predictable to achieve optimal cyclic pitch control authority. Data from a load cell during ground testing identified the exact angles for the mechanics used on PAVER.

Two structural failures prompted research into rotorcraft vibration and resonance. The rotor design directly affected modes of vibration and in the case of PAVER, hingeless flap and articulated lead/lag of the rotor systems required additional considerations. Airframe structures had to be designed such that their natural frequencies did not match the rotors' natural frequencies. Low frequency high amplitude vibrations had proven destructive in testing where a harmonic frequency existed within the operating rotor speed, and the ability for a blade to lead and lag in its mount only worsened these effects. Static rotor testing helped to determine the problematic RPM range and create procedures to operate outside of it. Airframe structural analysis should therefore prioritize the in-plane mode of vibration.

Another solution to minimize vibrations was to opt for a 3-blade rotorhead rather than a more common 2-blade system. From ground testing, it was seen that the 3-blade rotorhead had smaller peak vibration amplitudes at resonance frequencies. While mechanical blade tracking adjustments were more difficult as the blade count increased, the 3-blade configuration presented quieter operation and higher performance than the standard 2-blade system.

A drawback to the implementation of helicopter rotorheads is their inherent mechanical complexity. While a standard fixed-pitch, speed-controlled system only requires one channel for control (because all it can do is augment thrust), a helicopter rotor requires one channel for its motor, and three channels for its servo actuators. With four channels being required for each rotor on a vehicle like the PAVER, off-the-shelf electronic hardware quickly presented limitations. With the knowledge gained during this phase, a custom flight control system will be easier to develop for future research.

When a rotor failure occurs, the performance of a multirotor vehicle is degraded. A minimum thrust to weight ratio is required for the vehicle to remain airborne. Using any control, the theoretical minimum thrust-to-weight ratio of a quadcopter with one rotor failed should be greater than two. Tolerance to rotor failure increases as more rotors are added. A noticeable drop in minimum thrust-to-weight happens when increasing rotor count from four to six, but this effect become less observable as number of rotors increases. The number of rotors can be suggested based on the required tolerance to rotor failure, but a minimum thrust-to-weight prior to failure should be enforced.

Development of PAVER's control laws always began in the Simulink environment then proceeded to virtual flight-testing in a FlightGear simulation. The PID gains developed in the simulation environment were then applied to the test vehicle. While the real test vehicle flew very well, it was not identical to that in simulation, falling short of being “fully validated”. Analysis of simulation flight data compared to real flight data presented large discrepancies- the simulation model simply tracked the target setpoint too well. The PID gains obtained through simulation could be tuned better by performing hardware in the loop (HITL) simulations. Furthermore, as per current industry practice, the system model could be improved by performing system identification to get the bare airframe model, which represents the actual vehicle dynamics more accurately.

Future work will expand on the operational envelope of the PAVER drone, looking into autorotation capabilities and maneuvering envelopes for fly-by-wire multirotor aircraft. Through study of control law implementation, it was found that a Simplified Vehicle Operation control law could negate the benefits a high-performance over-actuated propulsion and control system could provide, degrading the potential for safe flight in nominal and off-nominal scenarios. Future work will include vehicle-centered force and moment capability envelopes that illustrate the control power potentials and limitations of the bare airframe in comparison to implemented control laws.

8 References

Alwi, H., & Edwards, C. (2008). Fault tolerant control using sliding modes with on-line control allocation. *Automatica , 44*(7), 1859-1866.

Blanken, C. L., Lusardi, J. A., Ivler, C. M., Tishler, M. B., Decker, W. A., Malpica, C. A., . . . Tucker, G. E. (2009). An investigation of rotorcraft stability-phase margin requirements in hover. *American Helicopter Society's 65th Annual Forum.* Grapevine, TX.

Coleman, R. P., & Feingold, A. M. (1958). *Theory of self-excited mechanical oscillations of helicopter rotors with hinged blades.* NACA.

Dhayagude, N., & Gao, Z. (1996). Novel approach to reconfigurable control systems design. *Journal of Guidance, Control, and Dynamics, 19*(4), 963-966.

Durham, W. C. (1994). Attainable moments for the constrained control allocation problem. *Journal of Guidance, Navigation, and Control, 17*(6), 1371-1373.

Falconì, G. P., Angelov, J., & Holzapfel, F. (2018). Adaptive fault-tolerant position control of a hexacopter subject to an unknown motor failure. *International Journal of Applied Mathematics and Computer Science, 28*(2).

Flannigan, J. E. (1972). Fly by wire technology. *AIAA Guidance and Control Conference*. doi:A72-39118

Gandhi, R. N. (2016). A comparison between quadrotor flight configurations. *42nd European Rotorcraft Forum.* Lille, France.

Gao, Z. (1996). Techniques in reconfigurable control system design. Retrieved from https://www.researchgate.net/publication/251454000

Hall, L. T. (2012, August 31). *Acro mode PID options and "Fly by wire"*. Retrieved from DIY Drones: https://diydrones.com/profiles/blogs/acro-mode-pid-options-and-fly-by-wire

Haller, B. (2020, May 14). *How control-allocation for multirotor systems works*. Retrieved 2021, from https://www.cantorsparadise.com/how-control-allocation-for-multirotor-systems-works-f87aff1794a2

Huang, C. Y., & Stengel, R. F. (2012). Restructurable control using proportional-integral implicit model following. *Journal of Guidance, Control and Dynamics, 13*(2).

Huang, C., Celi, R., & Shih, I.-C. (1996). Reconfigurable control designs and flying qualities evaluations for a CH-47. *AIAA, Guidance, Navigation and Control Conference*. doi:96-37445

Jaramillo, J., Yildirim, E., Koru, A. T., Yucelen, T., Pakmehr, M., Dunham, J., & Lu, G. (2022). Experimental results on dynamic attitude control allocation for a hexarotor platform with faulty motors. *AIAA SCITECH 2022 Forum.*

Johansen, T. A., & Fossen, T. I. (2013). Control allocation—A survey. *Automatica, 49*(5), 1087-1103.

Klyde, D. H., Schulze, P. C., Mitchell, D. G., Sizoo, D., Schaller, R., & McGuire, R. (2020). Mission task element development process: An approach to FAA handling qualities certification. *AIAA Aviation Forum.* Atlanta, Ga.

Kumar, M. V. (2008). Design of a stability augmentation system for a helicopter using LQR control and ADS-33 handling qualities specifications. *Aircraft Engineering and Aerospace Technology* .

Leishman, J. G. (2006). *Principles of helicopter aerodynamics.* New York: Cambridge University Press.

Lombaerts, T., Kaneshige, J., Schuet, S., Aponso, B. L., Shish, K. H., & Hardy, G. (2020). Dynamic inversion based full envelope flight control for an eVTOL vehicle using a unified framework. *AIAA Scitech 2020 Forum.*

Lunze, J., & Richter, J. (2008). Reconfigurable fault-tolerant control: A tutorial introduction. *European Journal of Control*, 359-386. doi:10.3166/EJC.14.359–386

Malpica, C., & Withrow-Maser, S. (2020). Handling qualities analysis of blade pitch and rotor speed controlled eVTOL quadrotor concepts for urban. *VFS International Powered Lift Conference.* San Jose, CA.

Oppenheimer, M. W., Doman, D. B., & Bolender, M. A. (2006). Control allocation for over-actuated systems. *14th Mediterranean Conference on Control and Automation.*

Peters, D. A., & HaQuang, N. (1988, October 1). Dynamic inflow for practical applications. *Journal of the American Helicopter Society, 33*(4), 64-68.

PX4 Autopilot. (2022, September 7). *PX4 user guide*. Retrieved from Airframes Reference: https://docs.px4.io/main/en/airframes/airframe_reference.html

Rashad, R., Jelmer Goerres, R., Aarts, J., Engelen, B., & Stramigioli., S. (2020). Fully actuated multirotor UAVs: A literature review. *IEEE Robotics & Automation Magazine, 27*(3), 97-107.

Roiati, R., Anderson, R. P., Collins, K. B., Hruswicki, P., Saini, V. V., Yang, X., & Sharma, N. (2022). *Development of a multi-rotor eVTOL using RPM, collective, and cyclic Control.* Vertical Flight Society.

SAE. (2021). *Bolt, machine -hexagon head, full shank AMS 5731, .250-28 UNJF-3A. (No enabled versions).* Washington DC: United States Department of Defense. Retrieved from Standards Central https://publishers.standardstech.com/content/military-dod-sae-as9490

SAE International. (1996). *Guidelines and methods for conducting the safety assessment process on civil airborne systems and equipment.* ARP 4761.

SAE International. (2010). *Guidelines for development of civil aircraft and systems.* ARP 4754.

SMG Consulting. (2021). *Advanced Air Mobility Reality Index*. Retrieved 2021, from https://aamrealityindex.com/

Stepanyan, V., Krishnakumar, K., & Bencomo, A. (2016). Identification and reconfigurable control of impaired multi-rotor drones. *AIAA Guidance, Navigation, and Control Conference*. doi:2016-1384

Stevens, B. L., Lewis, F. L., & Johnson, E. N. (2016). *Aircraft control and simulation : dynamics, controls design, and autonomous systems (Third edition.).* John Wiley & Sons.

The MathWorks, I. (2021). *Rise time, settling time, and other step-response characteristics*. Retrieved from Stepinfo: https://www.mathworks.com/help/ident/ref/lti.stepinfo.html

Tohidi, S. S., Sedigh, A. K., & Buzorgnia, D. (2016). Fault tolerant control design using adaptive control allocation based on the pseudo inverse along the null space. *International Journal of Robust and Nonlinear Control, 26*(16), 3541-3557.

Tohidi, S. S., Yildiz, Y., & Kolmanovsky, I. (2020). Adaptive control allocation for constrained systems. *Automatica , 121*(109161).

United States Army. (2000). *Aeronatuical design standard performance specification - Handling qualities requirements for military rotorcraft.* Redstone Arsenal, Alabama: United States Army.

Walter, A., McKay, M., Niemiec, R., Gandhi, F., & Ivler, C. (2019). Handling qualities based assessment of scalability for variable-RPM electric multi-rotor aircraft. *Vertical Flight Society's 75th Annual Forum.* Philadelphia, PA.

Walter, A., McKay, M., Niemiec, R., Gandhi, F., & Ivler, C. (2020). Hover handling qualities of fixed-pitch, variable-RPM quadcopters with increasing rotor diameter. *VFS 76th Annual Forum & Technology Display.* Virginia Beach, VA.

Ward, D. G., Monaco, J. F., & Schierman, J. D. (1999). Reconfigurable control for VTOL UAV shipboard landing. *Guidance, Navigation, and Control Conference and Exhibit*. Retrieved from https://doi.org/10.2514/6.1999-4045

Zaccarian, L. (2009). Dynamic allocation for input redundant control systems. *Automatica, 45*(6), 1431-1438.

A Data

Experimental and MATLAB/Simulink simulation data tables

Table A- 1. Collective sweep test at 1200 RPM

	Thrust (lb.)			**Torque (ft.lb.)**		
Collective	**Simulated**	**Experimental**	**% Error**	**Simulated**	**Experimental**	**% Error**
2°	3.607	2.3779	34.075	1.106	0.8841	20.063
4°	7.654	6.5914	13.883	1.478	1.3150	11.028
6°	12.18	11.0963	8.897	2.107	2.0323	3.545
8°	17.08	16.6490	2.523	2.991	3.1796	6.306
10°	22.24	21.8599	1.709	4.125	4.4740	8.461
12°	27.6	25.7658	6.646	5.501	5.8618	6.559
13°	30.34	27.6188	8.969	6.279	6.6821	6.420

Table A- 2. Collective sweep test at 1400 RPM

	Thrust (lb.)			**Torque (ft.lb.)**		
Collective	**Simulated**	**Experimental**	**% Error**	**Simulated**	**Experimental**	**% Error**
2°	4.599	3.5008	23.879	1.502	1.1645	22.470
4°	10	9.3447	6.553	2.004	1.7811	11.123
6°	16.17	15.4629	4.373	2.861	2.7586	3.579
8°	22.86	22.8104	0.217	4.067	4.3109	5.997
10°	29.91	30.1445	0.784	5.614	6.1973	10.390
12°	37.23	35.3489	5.053	7.491	7.9546	6.189
13°	40.97	38.3261	6.453	8.551	9.0866	6.264

Table A- 3. Collective sweep test at 1600 RPM

	Thrust (lb.)			Torque (ft.lb.)		
Collective	**Simulated**	**Experimental**	**% Error**	**Simulated**	**Experimental**	**% Error**
2°	5.686	3.8080	33.028	1.957	1.5145	22.611
4°	12.67	11.4580	9.566	2.609	2.3090	11.499
6°	20.75	19.9798	3.712	3.729	3.6183	2.969
8°	29.52	29.2651	0.863	5.308	5.5752	5.034
10°	38.76	38.3329	1.102	7.331	8.0083	9.239
12°	48.33	45.6381	5.570	9.787	10.4680	6.958
13°	53.23	48.7372	8.440	11.17	11.8695	6.262

Table A- 4. Collective sweep test at 1800 RPM

	Thrust (lb.)			Torque (ft.lb.)		
Collective	**Simulated**	**Experimental**	**% Error**	**Simulated**	**Experimental**	**% Error**
2°	6.87	5.5594	19.077	2.472	1.8427	25.457
4°	15.68	14.9723	4.513	3.294	2.8124	14.621
6°	25.93	25.8491	0.312	4.712	4.5181	4.115
8°	37.06	38.1072	2.826	6.713	7.1543	6.574
10°	48.78	51.4722	5.519	9.276	10.6325	14.624
12°	60.93	58.7986	3.498	12.39	13.3289	7.578
13°	67.13	60.4398	9.966	14.14	14.6198	3.393

Experimental and RCAS graphs

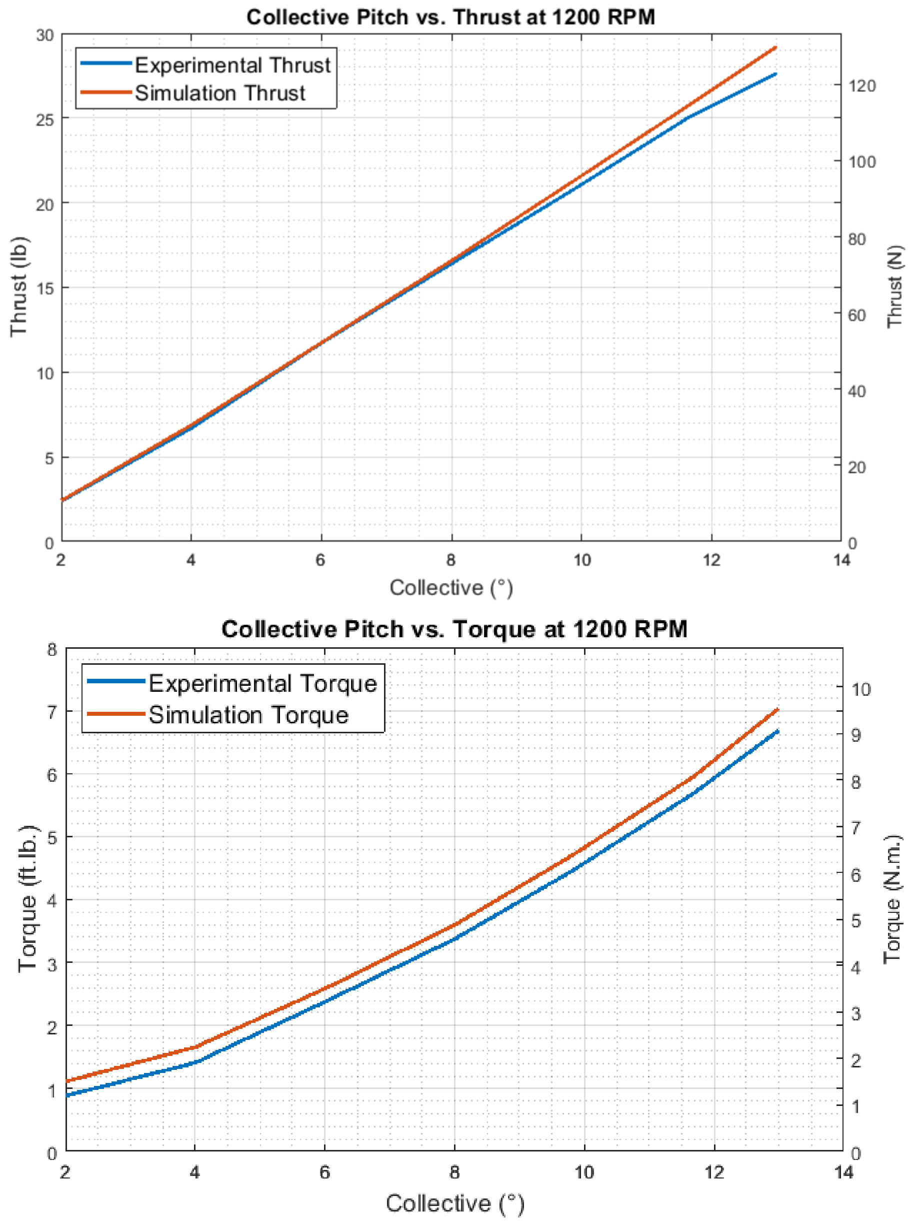

Figure A- 1. Collective pitch vs thrust (top) & collective pitch vs. torque (bottom) at 1200 RPM

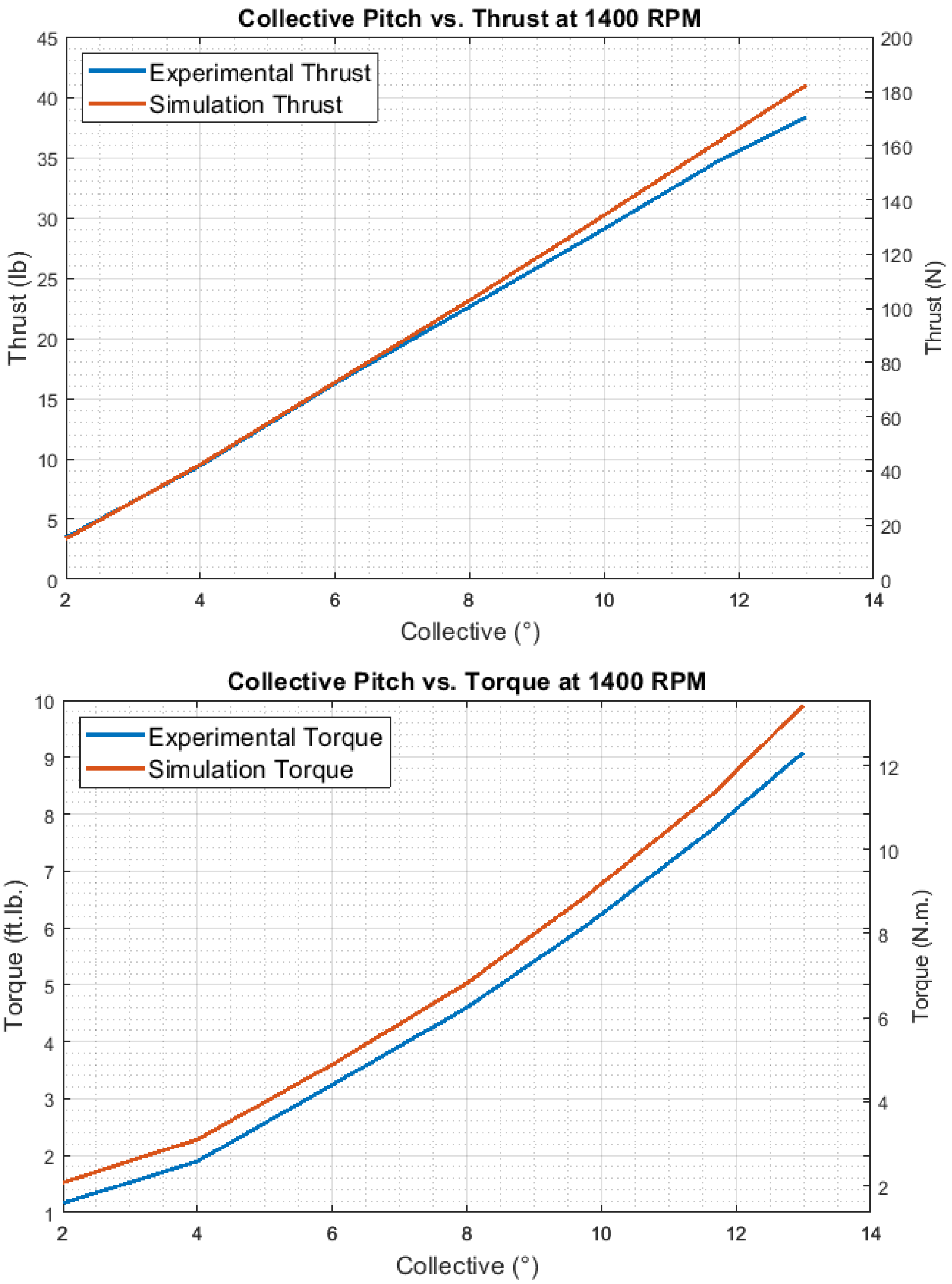

Figure A- 2. Collective pitch vs thrust (top) & collective pitch vs. torque (bottom) at 1400 RPM.

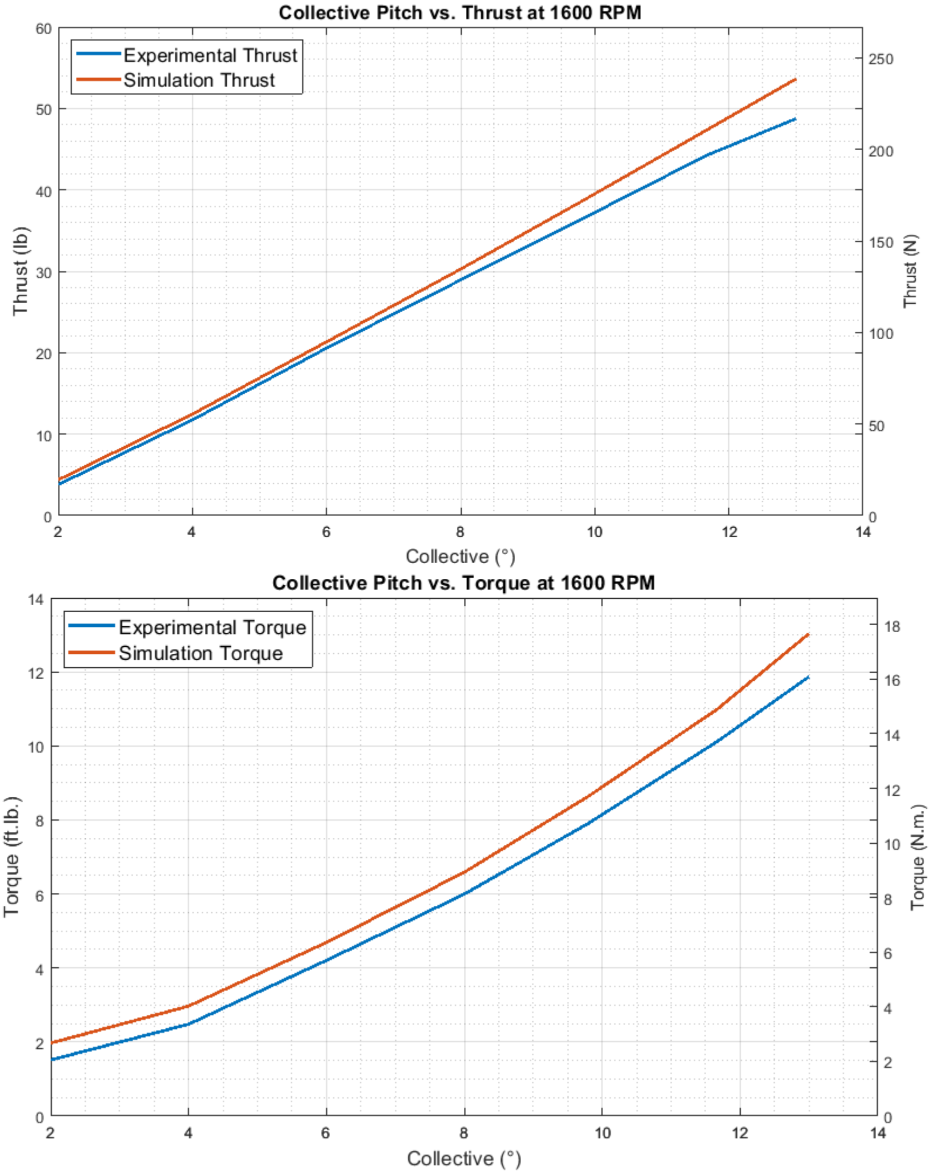

Figure A- 3. Collective pitch vs thrust (top) & collective pitch vs. torque (bottom) at 1600 RPM.

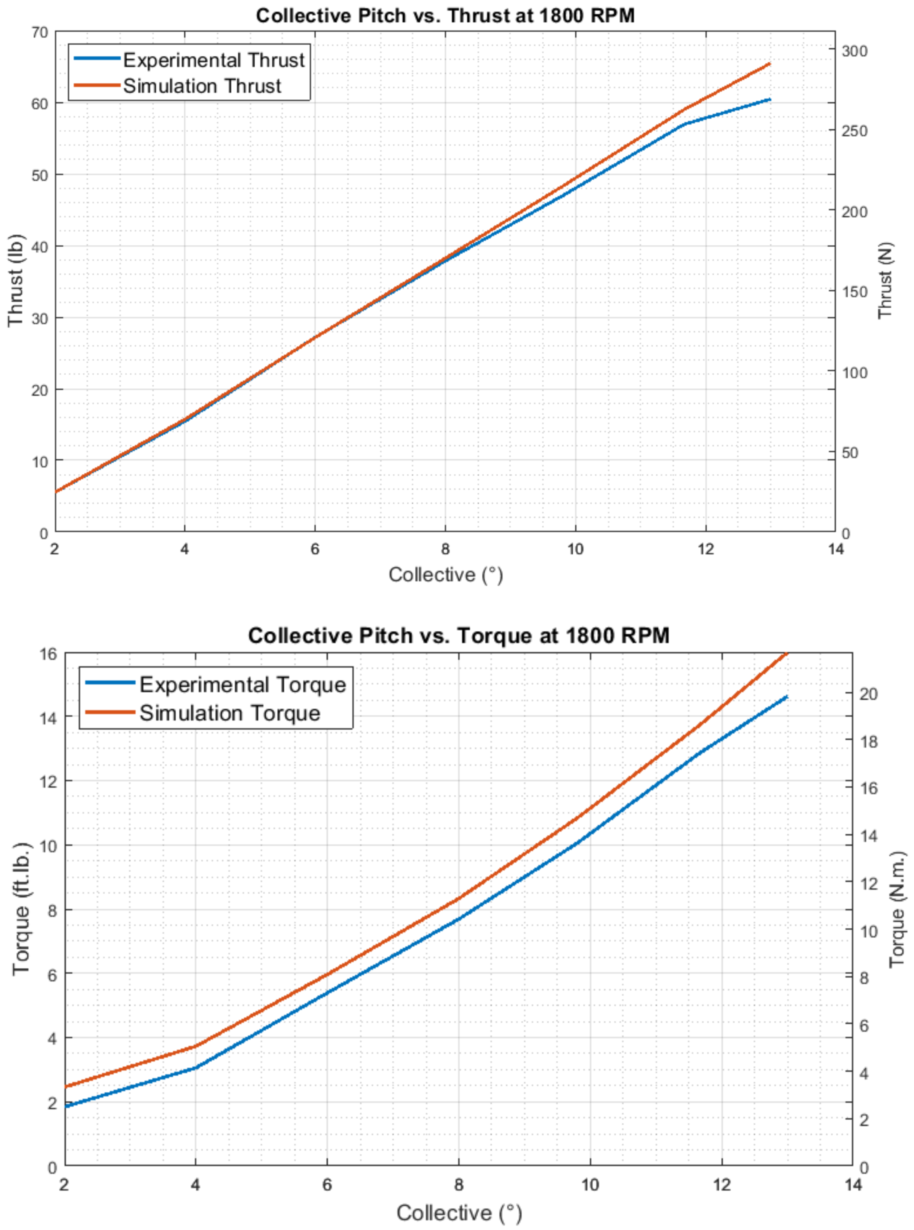

Figure A- 4. Collective pitch vs thrust (top) & collective pitch vs. torque (bottom) at 1800 RPM.

Experimental and RCAS data tables

Table A- 5. Collective sweep test at 1200 RPM

	Thrust (lb.)			Torque (ft.lb.)		
Collective	**Simulated**	**Experimental**	**% Error**	**Simulated**	**Experimental**	**% Error**
2°	2.4166	2.3779	1.601%	1.1108	0.8841	20.409%
4°	6.6879	6.5914	1.443%	1.5530	1.3150	15.325%
6°	11.5290	11.0963	3.753%	2.3086	2.0323	11.968%
8°	16.5290	16.6490	0.799%	3.3382	3.1796	4.751%
10°	21.5360	21.8599	1.504%	4.6206	4.4740	3.173%
12°	26.6170	25.7658	3.198%	6.1577	5.8618	4.805%
13°	29.2180	27.6188	5.473%	7.0330	6.6821	4.989%

Table A- 6. Collective sweep test at 1400 RPM

	Thrust (lb.)			Torque (ft.lb.)		
Collective	**Simulated**	**Experimental**	**% Error**	**Simulated**	**Experimental**	**% Error**
2°	3.3679	3.5008	3.946%	1.5287	1.1645	23.824%
4°	9.2793	9.3447	0.705%	2.1389	1.7811	16.728%
6°	15.9600	15.4629	3.115%	3.1889	2.7586	13.494%
8°	22.8980	22.8104	0.383%	4.6300	4.3109	6.892%
10°	30.2540	30.1445	0.362%	6.5073	6.1973	4.764%
12°	37.3680	35.3489	5.403%	8.6791	7.9546	8.348%
13°	40.9960	38.3261	6.513%	9.9132	9.0866	8.338%

Table A- 7. Collective sweep test at 1600 RPM

	Thrust (lb.)			**Torque (ft.lb.)**		
Collective	**Simulated**	**Experimental**	**% Error**	**Simulated**	**Experimental**	**% Error**
2°	4.3969	3.8080	13.394%	1.9716	1.5145	23.184%
4°	12.1090	11.4580	5.376%	2.7720	2.3090	16.703%
6°	20.8820	19.9798	4.320%	4.1637	3.6183	13.099%
8°	29.9790	29.2651	2.381%	6.0675	5.5752	8.114%
10°	39.2990	38.3329	2.458%	8.4774	8.0083	5.534%
12°	49.0860	45.6381	7.024%	11.4520	10.4680	8.592%
13°	53.6310	48.7372	9.125%	13.0350	11.8695	8.941%

Table A- 8. Collective sweep test at 1800 RPM

	Thrust (lb.)			**Torque (ft.lb.)**		
Collective	**Simulated**	**Experimental**	**% Error**	**Simulated**	**Experimental**	**% Error**
2°	5.5459	5.5594	0.243%	2.4571	1.8427	25.005%
4°	15.3090	14.9723	2.199%	3.4811	2.8124	19.209%
6°	26.3840	25.8491	2.027%	5.2496	4.5181	13.934%
8°	38.0500	38.1072	0.150%	7.7099	7.1543	7.206%
10°	50.4720	51.4722	1.982%	10.9250	10.6325	2.677%
12°	60.9360	58.7986	3.508%	14.2800	13.3289	6.660%
13°	65.4470	60.4398	7.651%	15.9880	14.6198	8.558%